8-2012

ENVIRONMENTAL IMPLICATIONS AND APPLICATIONS OF NANOMATERIALS

Priyanka Bhattacharya
Clemson University, pbhatta@g.clemson.edu

ENVIRONMENTAL IMPLICATIONS AND APPLICATIONS OF NANOMATERIALS

A Dissertation
Presented to
the Graduate School of
Clemson University

In Partial Fulfillment
of the Requirements for the Degree
Doctor of Philosophy
Physics

---

by
Priyanka Bhattacharya
August 2012

Accepted by:
Dr. Pu Chun Ke, Committee Chair
Dr. Apparao M. Rao
Dr. Chad E. Sosolik
Dr. David A. Ladner

ABSTRACT

Recent advances in material science and nanotechnology have given rise to a myriad of developments, while in the meantime call for research into the impacts of nanomaterials on the environment and human health. Although considerable progress has been made in the past decade concerning the behavior of nanomaterials in biological systems, such understanding is critically lacking with respect to the fate of nanomaterials in ecosystems.

Accordingly, this dissertation addresses the interactions between nanomaterials and algae—the major constituent of the aquatic food chain (Part I, Chapter two), and exploits the physicochemistry of nanoscaled synthetic dendritic polymers for environmental applications, especially for water purification that is a focused theme of the entire dossier (Part II, Chapters two-five).

This dissertation is organized as follows.

Chapter one presents a general review of the physical/physicochemical properties, characterizations, implications—especially ecological implication, and applications of a host of most produced and studied nanomaterials. In addition, advances in environmental applications of nanomaterials are discussed.

Chapter two examines algal responses to two major types of engineered nanomaterials – quantum dots and polystyrene. Inhibited photosynthetic activities of green algae are observed as a result of the physical adsorption of the nanomaterials.

Chapter three elucidates the physicochemical properties of poly(amidoamine)-tris(hydroxymethyl)amidomethane- and amine-terminated dendrimers towards their applications in water remediation. Here, the capacities and mechanisms of the dendrimers in

hosting cationic copper, anionic nitrate, polyaromatic phenanthrene, and the more heterogeneous humic acids are discussed.

Based on the results of Chapter three, Chapter four presents a dendrimer-based novel optical scheme for improving the detection sensitivity and selectivity of environmental pollutants. Specifically, the surface plasmon resonance of a gold nanowire and the high hosting capacity of dendrimers are utilized for enhancing the detection limit of copper down to the nanomolar level.

Chapter five exploits a promising use of dendrimers for the removal of potentially harmful discharged nanoparticles. Here fullerenols are used as a model nanomaterial, and their interactions with dendrimers of two different generations are studied using spectrophotometry and thermodynamics methods.

Chapter six summarizes the key findings in this dissertation and presents future work that is stimulated by this PhD research.

DEDICATION

I dedicate this dissertation to Mr. T. Haldar – my first physics teacher, and Drs. Pushan Ayyub and Shankar Ghosh, for their encouragement, patience and guidance; to my mother and brother to whom I remain indebted for being the rocks of my life; to my father, for his boundless blessings from the heavens above. He would have loved a copy of this dissertation and I had always imagined giving him one.

ACKNOWLEDGMENTS

Any accomplishment usually entails the work of many and I'd like to thank them all for making this dissertation possible.

My profound thanks go to my PhD advisor, Dr. Pu Chun Ke, whose unmatched guidance, patience and support throughout this dissertation work was the most instrumental. Dr. Ke motivated me to continuously push the boundary of traditional disciplines and discover that research niche which now I call my own. He was always available to answer my doubts and share exciting ideas, scholarly essays and skills. I thank him for making my PhD experience an incredible learning experience and an enchantment – it was my greatest pleasure working under his guidance.

My gratitude goes to my PhD committee members – Drs. Apparao M. Rao, Chad E. Sosolik and David A. Ladner for their time, expertise, discussions and critiques that enhanced the coherence and rigor of this dissertation.

I am forever indebted to my collaborators – Dr. Nihal Rajapakse for his expertise on photochemistry, Drs. Monica H. Lamm and Seung-Ha Kim at Iowa State University for their elegant molecular insight which enriched and diversified my experimental studies, Dr. Paul Dubin at UMass Amherst for his profound knowledge in polymer physics, Dr. Edgardo Etxeberria at the University of Florida for introducing me to plant physiology, and Dr. Jared Brown at Brody School of Medicine, East Carolina University for allowing me to experiment with dendrimers for drug delivery. I am thankful to Dr. JoAn Hudson and her staff at the Electron Microscope Facility of Clemson University for teaching me the essential skills of scanning and transmission electron microscopy.

I am grateful to both Clemson University and the Department of Physics and Astronomy for making my Clemson stay such a rewarding experience. I greatly acknowledge fundings from NSF (Career Award No. CBET-0744040) and EPA (RD34092) to Dr. Ke and EPA (RD835182) to Dr. David Ladner and Dr. Pu Chun Ke for this research. I am thankful to COMSET and Sigma Xi – the National Scientific Research Society for their generous fellowship and scholarship awarded during my study.

It was a great pleasure working with Dr. Sijie Lin, Dr. Tatsiana Ratnikova, Ran Chen, Pengyu Chen, Nick Geitner, Slaven Radic, Poonam Choudhary, James Turner, Ryan Schurr, Mercy Lard, Dr. Seung-Ha Kim, and Nathan Conroy – my lab mates and colleagues during my time at Clemson.

I'd like to thank my good friends – Deepika, Aesha, Tanzeel, Anirudh, Keyur, Atanu, Harshad, Akash and Poulomi for their encouragement and cheers that I always cherished.

Last but not least, I would like to thank my family for their love through thick and thin.

TABLE OF CONTENTS

Page

TITLE PAGE i

ABSTRACT ii

DEDICATION iv

ACKNOWLEDGMENTS v

LIST OF TABLES ix

LIST OF FIGURES x

CHAPTER

I. LITERATURE REVIEW 1

Introduction 1
Nanomaterials fabrication, properties and characterization 2
Environmental implications of nanomaterials 5
Environmental applications of nanomaterials 22

II. ENVIRONMENTAL IMPLICATIONS OF NANOMATERIALS 47

Introduction 50
Nanomaterials characterization 54
Algal cell characterization 57
Interactions of QDs with algae 58
Interactions of PS with cellulose 69
Interactions of PS with algae 72
Discussions and summary 84

III. ENVIRONMENTAL APPLICATIONS OF NANOMATERIALS. I. UNDERSTANDING THE PHYSICO-CHEMICAL BEHAVIOR OF DENDRIMERS IN HOSTING A VARIETY OF CHEMICAL SPECIES 87

Introduction 88
A tris-dendrimer for hosting diverse chemical species 92
A PAMAM dendrimer for mitigating humic foulant 105
Discussions and summary 117

Table of Contents (Continued) Page

IV. ENVIRONMENTAL APPLICATIONS OF NANOMATERIALS. II. AN ENHANCED DETECTION OF POLLUTANTS USING DENDRIMERS 119

Introduction 119
Materials 120
Characterization of dendrimer-Cu(II) binding 121
Enhancing the limit of Cu(II) detection by dendrimer 123
Evaluating the selectivity of dendrimers towards Cu(II) 129
Discussions and summary 131

V. ENVIRONMENTAL APPLICATIONS OF NANOMATERIALS. III. DENDRITIC NANOTECHNOLOGY FOR REMEDIATING DISCHARGED NANOPARTICLES 132

Introduction 132
Materials 136
An empirically determined ratio of dendrimer-fullerenol assembly 136
Thermodynamics of dendrimer-fullerenol assembly 140
Intermolecular interactions in dendrimer-fullerenol assembly 143
Discussions and summary 148

VI. CONCLUSION AND FUTURE WORK 150
Part I: Environmental implications of nanomaterials 150
Part II: Environmental applications of nanomaterials 153
Future work 158

APPENDIX 161

A: Glossary of terms 161

REFERENCES 164

LIST OF TABLES

Table Page

5-1. Characterizations of fullerenols, PAMAM dendrimers and their assemblies. 138

LIST OF FIGURES

Figure Page

1-1. The logical chain of events accounting for the toxicity of NP starts with the sources of NPs and their entrance routes into the ecosystem. 5

1-2. Results of a comprehensive synthesis of reported engineered nanoparticles toxicity for a wide variety of taxonomic groups. 7

1-3. Significance of invertebrate species in the aquatic food web and the possible routes of environmental exposure to NPs after release to the aquatic environment. 9

1-4. The structure a single-celled alga Protococcus is similar in some ways to a plant cell. 10

1-5. Simplified scheme of some terrestrial and aquatic ecosystem processes. 14

1-6. Summary illustrating historical stages in the development, production and use of plastics together with associated concerns and legislative measures. 16

1-7. The Great Pacific Garbage Patch. 18

1-8. Summary of conventional water purification technologies based on the size of the particles to be removed. 25

1-9. Ion exchange processes. 27

1-10. Schematic of screen and depth filtration. 29

1-11. Schematic of a RO system. 30

1-12. Operational issues with removing multiple contaminants from drinking water. 32

1-13. Illustration of DNAPL distribution as residual saturation (sources) and a plume of dissolved contaminants in an aquifer. 34

1-14. Nanoscale iron particles for in situ remediation. 36

List of Figures (Continued)

Figure Page

1-15. Exemplary structure of a generation 0 and generation 2 poly(amidoamine) (PAMAM) dendrimer with amino and amidoethanol surface groups. 42

1-16. Recovery of metal ions from aqueous solutions by dendrimer enhanced filtration 45

Scheme 2-1. Schematic of the adsorption of QDs on algal cells and their effects on the algal photosynthesis. 49

Scheme 2-2. Schematic of the adsorption of PS beads on a cellulose substrate 50

2-1. Schematic representation of zeta potential 56

2-2. SEM image of *Chlamydomonas reinhardtii* sp. and schematic drawing of a *Chlamydomonas* cell. 58

2-3. Transmission electron microscopy image of CdSe/ZnS QDs, bright field image of algal cells and confocal fluorescence image of QDs adsorbed on algal cell surfaces. 59

2-4. Adsorbed vs. equilibrium QDs concentration and schematic of MUA ligand 62

2-5. Absorbance of bicarbonate indicator for acid, neutral, and basic solutions and comparison of CO_2 depletion rates for QDs of various dosages. 66

2-6. Oxygen evolution rate vs. dosage of QDs. 67

2-7. Fluorescence intensities of algae (purple), QDs (dark blue), and algae-QDs mixture 68

2-8. Cellulose chemical structure and a section of the plant cell wall. 70

2-9. Adsorbed vs. equilibrium PS bead concentration for cellulose thin films exposed to positively and negatively charged PS beads. 72

2-10. SEM images of algae adsorbed with PS beads. 73

List of Figures (Continued)

Figure Page

2-11. Zeta potentials of positively and negatively charged PS beads, *Chlorella* control, *Scenedesmus* control, and *Chlorella* and *Scenedesmus* mixed with positively and negatively charged PS beads.. 75

2-12. Adsorbed vs. equilibrium PS concentrations for positive and negative PS beads exposed to *Chlorella* and *Scenedesmus*..... 77

2-13. Absorbance vs. incubation time for *Chlorella* and *Scenedesmus* exposed to positively and negatively charged PS beads of 1.8-6.5 mg/L of algal solution.... 79

2-14. Mechanism of DCF assay..... 83

2-15. ROS production rates by *Chlorella* and *Scenedesmus* due to positive and negative PS adsorption..... 84

3-1. Structure of a generation 1 tris-dendrimer..... 90

3-2. Absorbance spectra of tris-dendrimer, copper, nitrate, PN, and tris-copper, tris-nitrate and tris-PN complexes at pH 10, 7 and 2, and enlarged branch of tris-dendrimer with possible specie coordinations at different pH. 97

3-3. The binding dynamics of Cu(II), NO_3^- and PN with tris-dendrimer..... 98

3-4. Spectrophotometric titration plots for tris-Cu(II), tris-NO_3^-, and tris-PN. 103

3-5. Hydrodynamic sizes of HA, G5-PAMAM and G5-HA complexes in the respective supernatants at different HA:G5-PAMAM ratios..... 106

3-6. Fluorescence emission spectra of HA and G5-PAMAM at different concentrations. 109

3-7. Fluorescence emission of HA in the presence of decreasing amounts of HA per G5-PAMAM, and Stern-Volmer plot for G5-HA complexes..... 110

3-8. Fraction of HA remaining in solution vs. ratio of HA per G5-PAMAM added..... 112

List of Figures (Continued)

Figure Page

Scheme 3-1. Schematic of complexation, aggregation and re-stabilization processes in dendrimer-HA interactions. 113

3-9. ATR-FTIR spectra of HA, G5-PAMAM and G5-HA complex..... 116

4-1. Experimental scheme showing detection of Cu(II) using G4-Sac dendrimers and Au-NW-induced SPR, and TEM image showing the adsorption of G4-Sac dendrimers onto a single Au-NW. 121

4-2. Absorbance of the Cu(II)-G4-Sac complex. 123

4-3. Fluorescence emission spectrum of Alexa Fluor 633 dye and absorbance of Cu(II), and fluorescence emission spectra of labeled G4-Sac, Au-G4-Sac complex, Cu(II)-G4-Sac complex, and Au-G4-Sac-Cu(II) complex.. 126

4-4. Average fluorescence emission intensity of G4-Sac- Cu(II) complexes with and without Au-NWs.. 128

4-5. Selectivity of G4-Sac toward Cu(II), and time evolution of FRET efficiency between labeled G4-Sac and Cu(II). 130

5-1. DLS measurements of G1/fullerenol and G4/fullerenol assemblies, and image of G4/fullerenol complexes. 139

5-2. ITC raw data and analysis plots of G1/fullerenol and G4/fullerenol complexes..... 142

5-3. Fluorescence emission of $C_{60}(OH)_{20}$ at different concentrations and plot of intensity of fluorescence emission of $C_{60}(OH)_{20}$ vs. concentration..... 144

5-4. Fluorescence emission of G1 and G4 at different concentrations..... 145

5-5. Fluorescence emission of fullerenol in the presence of increasing amounts of number of primary amines of G1 and G4 per fullerenol. 145

5-6. Stern-Volmer plots for G1/fullerenol and G4/fullerenol complexes..... 147

CHAPTER ONE

LITERATURE REVIEW

1.1. Introduction

The recent trend of science and technology has shown a convergence from the macroscopic and microscopic levels to the nano- and quantum scale. Over the past two decades, nanotechnology, a branch of engineering science that deals with creating objects smaller than 100 nm in dimension, has significantly advanced electronics, medicine, and materials, catalysis, and industrial engineering. This revolution has spawned activities affecting the social, economic, and environmental spheres, often in ways that are entirely unforeseen.

Along with innovations and growth of nanotechnology, however, there has been a growing concern over the potentially adverse environmental and health impacts of nanomaterials (1-8). Timely recognition of such concern and development of mitigating strategies will ensure the safe development of nanotechnology by avoiding the pitfalls plagued by past major technological developments of nuclear power, genetically modified foods, and information technologies; these latter technologies have often harmed the environment leading to public skepticism.

It is well accepted that environmental problems are a complicated mosaic of multiple phenomena that require multidimensional analysis and solutions. Consequently, interdisciplinary approaches that combine physical and biological sciences with a focus on the environment are often desirable for environmental protection and remediation. In the past physical sciences have had much to offer for addressing environmental issues:

advancements in laser physics and computing techniques have led to the development of air pollutant monitoring; developments in materials processing and design have created more efficient energy generation methods and recycling techniques; the use of geophysical methods to monitor radioactivity have established new clean-up strategies; environmental physicists have made major contributions to the understanding of global climate change and the ozone hole (9).

The central objective of this dissertation is to investigate the environmental implications and applications of nanotechnology. Strategically, the principles and techniques of physics, materials, and physical chemistry have been applied to examine the interactions between the environmental components of algae, humic substance, and contaminants and the nanomaterial matrix of quantum dots (QDs), plastic, and dendritic polymers. Part I of this dissertation is focused on evaluating the ecological implications of QDs and nanosized plastic adsorption. Part II of this dissertation concerns the applications of dendritic polymers for environmental remediation.

1.2. Nanomaterials Fabrication, Properties and Characterization

Recent development in high-resolution instrumentation such as scanning tunneling microscopy, atomic force microscopy, and electron microscopy, as well as the establishment of new disciplines of supramolecular chemistry and molecular self-assembly has enabled fabrication of nanomaterials of unique morphology, strictly controlled size, shape, and crystalline structures, and has led to discoveries of fullerenes and carbon nanotubes (CNTs) and the synthesis of novel nanomaterials such as QDs and nanowires. Such materials are being extensively applied to a number of fields, including but not limited to catalysis, optics,

electronics, and biotechnology (10). An important aspect of nanomaterials is their increased ratio of surface area to volume, giving rise to quantum mechanical effects. Such reduction in size also results in unique physical properties such as increased mechanical strength, as well as the quantum effects which alter their electronic properties.

Two main approaches are used in the synthesis of nanomaterials (11):

a. *Top-down approach* – This involves division of a massive solid into smaller portions by either mechanical milling or attrition (mechano-synthesis), chemically breaking specific bonds (e.g., hydrogen bonds) that hold together larger repeating elements of the bulk solid, or volatilization of a solid by laser ablation and solar furnace, followed by condensation of the volatilized components.

b. *Bottom-up approach* – This involves condensation of atoms or molecular entities in a gas phase or solution. This *self-assembly* approach is far more popular in the synthesis of nanoparticles (NPs). Moreover, these NPs can be modified in liquid suspension by treatment with various chemical species for a diverse range of applications including integration with biological systems.

A number of novel physical phenomena emerge as the size of the system decreases. For instance:

i. Opaque substances become transparent (copper). Electromagnetic radiations have a penetration depth on the order of 50 nm through most of the optical spectrum. Hence, when the size of a bulk solid is reduced to the order of the penetration depth, most of the electromagnetic radiation is transmitted through the substance making it transparent vs. the opacity/reflectance in its bulk form (12).

ii. Stable materials turn combustible (aluminum). High specific area of nanomaterials renders high reactivity and short reaction times (13).

iii. Chemically inert materials serve as catalysts (gold). Partial electron transfer from the surface to gold nanocluster and oxygen-vacancy F-center defects are shown to play an essential role in the activation of the gold nanoclusters (14).

iv. Hydrophilic metallic substances become hydrophobic (15). A dual-scale roughness at a specific aspect ratio of metallic nanowires imparts them with water-repelling characteristics.

v. Good insulators become conductors (silicon) (16). In layers thinner than 100 nanometers, the properties of the element itself become irrelevant: what matters is the surface. Cleaning promotes conductivity by creating new electronic states on the silicon surface where electrons can reside.

It is clear that much of the unique nanomaterial properties are influenced by the particle size. Besides, surface properties such as surface charge play an important role in determining nanomaterial reactivity. Particle size characterization becomes imperative because nanomaterials generally remain aggregated in aqueous media due to their surface hydrophobicity. Most of the conventional methods for particle size characterization are based on light scattering, such as electron microscopy (EM) and dynamic light scattering. In addition, NP surface charge can be modified, intentionally or unintentionally through chemical functionalization (to increase stability in aqueous media) or absorption of species onto the NP surface. Surface charge is a key parameter controlling NP stability in aqueous media; it varies as a function of pH due to protonation or deprotonation of functional groups, while remains fixed resulting from crystal lattice defects and atomic substitution.

Nanoparticle surface charge is usually characterized by measuring the zeta potential of the particle derived from its electrophoretic mobility in the aqueous media.

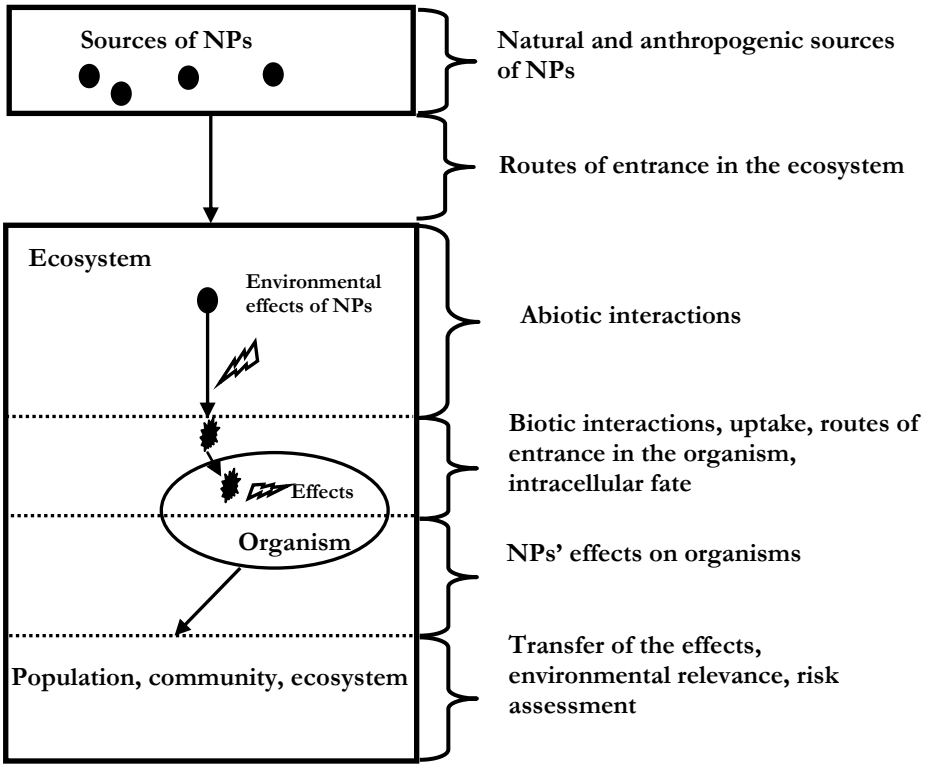

Figure 1-1. The logical chain of events accounting for the toxicity of NP starts with the sources of NPs and their entrance routes into the ecosystem (Adopted from (17)).

1.3. Environmental Implications of Nanomaterials

Throughout the lifecycle of nanomaterials' production, use, disposal and reuse, there are high chances of them being exposed to the aqueous environment (Figure 1-1). Such exposure is governed by the highly reactive surfaces of the nanomaterials, which dictate their aggregation and deposition. The stability and transport of NPs are important in determining

whether these novel materials can be removed by water treatment technologies, or whether NPs have a high potential for mobility in the environment. The properties of particular interest to environmental analysis include surface charge, presence of surface functional groups, Hamaker constant, and interaction energy with water (wettability). The tendency of NPs to aggregate, particularly in natural systems, is an important consideration in determining not only their mobility, fate, and persistence, but also their toxicity. Guldi and Prato (18) suggested that destabilized NPs experience a decreased ability to produce reactive oxygen species (ROS) and this may have implications regarding their toxicity (19). Conversely, agglomeration of CNTs within the lungs of laboratory test animals, where they were intentionally introduced, led to their suffocation (20, 21). Hetero-aggregation, or aggregation with other materials in the environment, could also alter the functional properties of nanomaterials.

Some NPs, such as fullerenes (C_{60}), are inherently insoluble in water due to their attractive interfacial hydrophobic interactions. Their surfaces may be modified chemically by attaching functional groups (-OH, -COOH, -NH) to render them soluble. However, it is interesting to note that such modification of the nanoparticle surface may not in fact result in perfect dispersion (22). For instance, hydroxylation of C_{60} to form fullerenol ($C_{60}(OH)_{20}$) increases its affinity for water molecules in the aqueous phase through hydrogen bonding, but transmission electron microscopy (TEM) images show they readily form molecular clusters composed of many fullerenol molecules (23). Inhomogeneous distribution of the OH groups on the surface of the C_{60} molecule can result in distributed hydrophobic-hydrophilic regions and attractive patch-patch interactions between the hydrophobic regions can initiate their clustering. In addition to aggregation, particle deposition also determines

their ecological activities. Interactions with natural organic matter (NOM), ubiquitous in all aquatic systems, can alter the effective charge, reactivity and hydrodynamic radius of NPs (24). Hence, it is important to consider the behavior of NPs in aquatic systems in order to evaluate their potential impacts on the ecosystem.

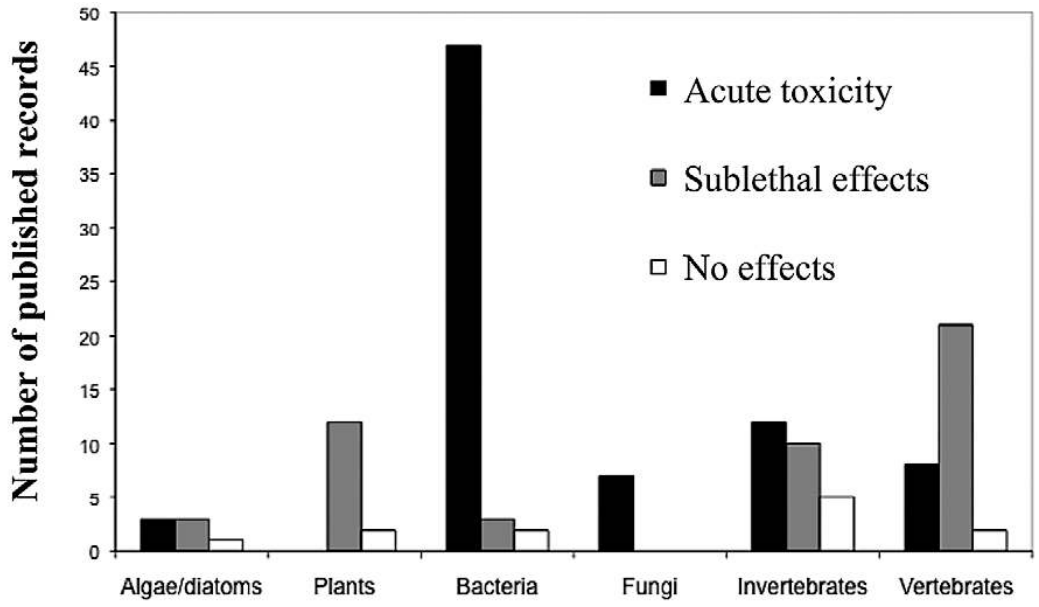

Figure 1-2. Results of a comprehensive synthesis of reported engineered nanoparticles toxicity for a wide variety of taxonomic groups (25).

Ironically, the properties of nanomaterials that make them desirable to the medical field may create concerns in terms of environmental impact, such as nanoparticle uptake by cells. Over the last decade, a number of studies have focused on the possible health effects of carbon based nanomaterials such as fullerenes. Fullerenes are powerful antioxidants, comparable in strength to vitamin E, while other studies report that some types of fullerenes

can be toxic to tumor cells, cleave DNA, and inhibit bacterial growth (26-31). Exposure via inhalation during nanomaterial fabrication such as that of CNTs have been shown to damage lungs, which has also been observed with silica and asbestos (20). Similarly, adverse effects upon dermal exposure should also be considered for assessing the risks of both nanomaterial fabrication and product use.

Thus far, much of the work on nanotoxicity has focused on possible human exposure. However, it has become imperative to conduct ecotoxicological studies of nanomaterials given their inevitable release into the environment. Early work in this latter field has been focused on fullerene-based nanomaterials. For example, Oberdörster (32) showed that fullerenes could impair brain functions in fish. However, very little is known regarding the ecological impacts of metal oxide NPs (e.g., TiO_2, ZnO) and QDs – some of the most produced nanomaterials (Figure 1-2). Specifically, TiO_2 in the anatase phase is used as a pigment in paints, paper, inks, and plastics. Crystalline SiO_2 works as both a semiconductor and an electrical insulator. The ceramic nature of ZnO allows its use both as a pigment and a semiconductor. QDs are semiconductors that display narrow fluorescence and broad absorption bands due to the quantum effects constraining electrons and are widely applied in medical imaging and sensing. Such widespread use of NPs stresses the need to evaluate their environmental fate from cradle (point of manufacture) to grave (point of use and disposal).

Hence, an important component of this dissertation is to assess the impacts of environmentally released NPs on aquatic algae. These studies are essential for filling a critical knowledge gap because algae serve as the basis of the food chain and are primary agents for global biogeochemical cycles. Any impact on such organisms will cascade and biomagnify

through the ecosystem, ultimately affecting humans. For this particular aspect we chose two types of NPs – QDs and polystyrene (PS) NPs – as models for assessing the impacts of hard vs. polymeric NPs on algae.

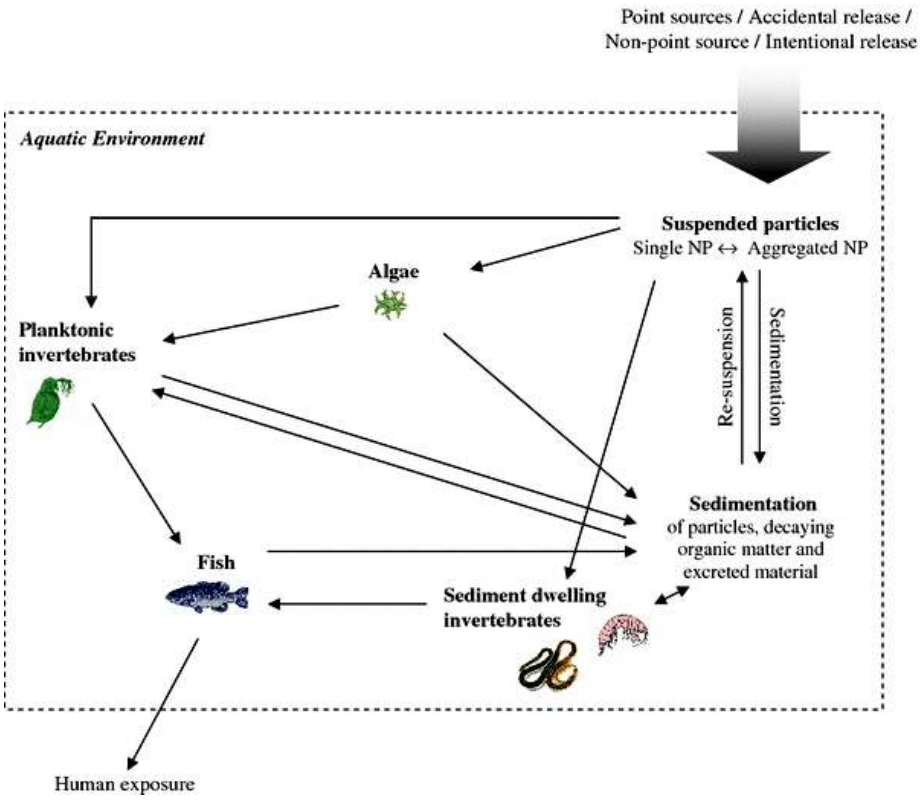

Figure 1-3. Significance of invertebrate species in the aquatic food web and the possible routes of environmental exposure to NPs after release to the aquatic environment. After entry of NPs into the aquatic environment the suspended particles will be taken up by planktonic or sediment dwelling invertebrates through different exposure routes (i.e. direct uptake from the water phase or through food uptake) (33).

1.3.1. Ecotoxicity of non-organic nanoparticles

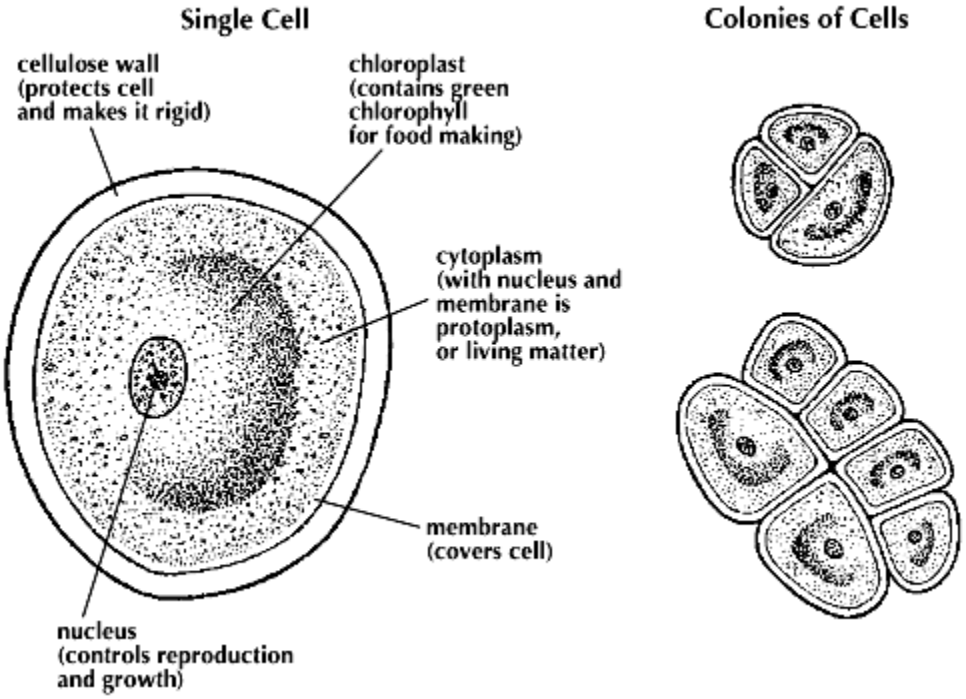

Figure 1-4. The structure of a single-celled alga Protococcus is similar in some ways to a plant cell. Algal cells, like those in plants, have a nucleus and a stiff cell wall made of cellulose. Floating in the cell's cytoplasm is a chloroplast, which contains chlorophyll. The chlorophyll uses energy from sunlight to make food from carbon dioxide and water. Colonies of these algae cells form green scum on ponds and moist rocks (Image courtesy: *Encyclopedia Britannica Kids*).

Unlike mammalian cells, most plants, algae, bacteria and fungi possess cell walls (Figure 1-4) whose major components are carbohydrates, linked to form a rigid complex network, and proteins (34). The cell wall forms a primary site of interaction and a barrier for the entrance of NPs into the cell. The cell walls in plants and algae mainly consist of cellulose. Algae typically also possess glycoproteins and polysaccharides in their cell walls

whose functional groups such as carboxylates, phosphates, hydroxyls, and amines provide for active sites for interacting with NPs (35). Cell walls are semipermeable beneath which is the plasma membrane. The diameter of pores across the cell wall ranges between 5 to 20 nm (36, 37). Thus, only NPs and their aggregates with a size smaller than that of the largest pore are expected to pass through the cell wall and reach the plasma membrane. Moreover, the interactions between NPs and cells might physically damage the cell wall and induce pore formation. This could potentially result in new sites for NP internalization. The plasma membrane is a bilayer lipid membrane with embedded proteins and is selectively permeable. The transport mechanisms that control the movement of substances across the membrane include passive transport through diffusion and osmosis, transport of nutrients through the transmembrane protein channels, active transport through energy dependent endocytosis, and extrusion of unwanted substances through exocytosis. The potential entry routes for NPs to penetrate through this bilayer lipid membrane have been discussed recently (38), including endocytosis and facilitation via carrier proteins and ion channels. Once crossing the membrane, NPs may interfere with metabolic processes of organelles such as endoplasmic reticulum, golgi apparatus, and endo-lysosomal system, possibly through the production of ROS. For example, the swelling of the endoplasmic reticulum, vacuolar changes, and phagosomes were explicitly seen in macrophage cells exposed to high doses of single-wall CNTs (39).

Among the limited studies on the effects of NPs on algae, plants, and fungi, both direct and indirect effects have been found. Direct toxic effects of NPs on organisms are mainly determined by their chemical composition and surface reactivity, which might incite redox reactions upon contact with organic molecules and impact on photosynthetic or

respiratory processes. Silva et al. (40) suggested that the accumulation of NPs in photosynthetic surfaces might provoke foliar heating due to stomata obstruction and alteration of gas exchange in plants. NPs such as fullerenes have a photo-induced electron transfer capacity (41). Therefore these NPs possess the capability of affecting photosynthetic and respiratory processes upon cell entry. TiO_2 NPs have been shown toxic to green algae *Desmodesmus subspicatus*. While larger TiO_2 NPs caused less toxicity, the toxicity induced by small TiO_2 NPs exhibited a clear dose-response relationship with their specific surface area (42). However, the aspect of NP aggregation, which could possibly influence inhibitory effects, was not examined. Similarly, the effects of alumina (Al_2O_3) NPs on plant root growth have been shown to depend upon their size instead of chemical composition (43). Zn and ZnO NPs have also been shown to affect growth in radish, rape, and ryegrass (44). These researchers concluded that the observed phytotoxic effects were related to the NPs themselves rather than the released ionic constituents of the NPs, since neither the supernatant after centrifugation nor the filtrated Zn and ZnO solutions showed any adverse effect on the plants. However, Wong et al. (45) recently showed that the toxicity of ZnO NPs to marine diatoms *Skeletonema costatum* and *Thalassiosia pseudonana* could be mainly attributed to dissolved Zn^{2+}. The algal cell surfaces is predominantly negatively charged (46) and hence attract the positively charged Zn^{2+} and ZnO NPs to further cause damage either mechanically or via ROS generation. This observation was supported by a number of other studies (19, 47, 48).The major difference in the differential toxicities of ZnO NPs and Zn^{2+} in the above studies is the high concentration of ZnO NPs used in the former which could primarily lead to aggregation induced mechanical damage to the ryegrass. Similarly, silver

nanoparticles (AgNPs) were shown to incite membrane alterations, increase its porosity, and disrupt the capacity of bacteria in regulating membrane transport (49, 50).

The indirect effects of NPs are caused mainly by physical restraints, release of toxic ions, or ROS production. As an example of physical restraint, the accumulation of NPs on the surface of photosynthetic organisms may inhibit photosynthetic activity because of shading effects, i.e., reduced light availability, rather than because of toxicity of the NPs. Such adsorption could also block the uptake of essential nutrients either through clogging of the cell wall or nutrient adsorption. It was observed that aggregates of carbon black bound to sperm cells reduced fertilization success of *Fucus serratus*, a marine seaweed (51). NPs might produce ROS upon their interaction with organisms or with agents present in the environment (e.g., ultraviolet (UV) radiation). NPs with photocatalytic properties such as TiO_2, AgNPs and fullerenes have shown antibacterial effect with sunlight or a UV illumination (52, 53). The generation of ROS can also be induced by release of toxicants from NPs. Ionic silver (Ag^+) released from AgNPs inhibits respiratory enzymes and induces oxidative stress upon ROS generation (50, 54). Ag^+ may also bind to sulfur- and phosphorus-containing molecules (S-adenosylmethionine, cysteine, taurine, glutathione, etc.) involved in cell defense against oxidation (54, 55), and may result in depletion of intracellular concentration of those molecules (56).

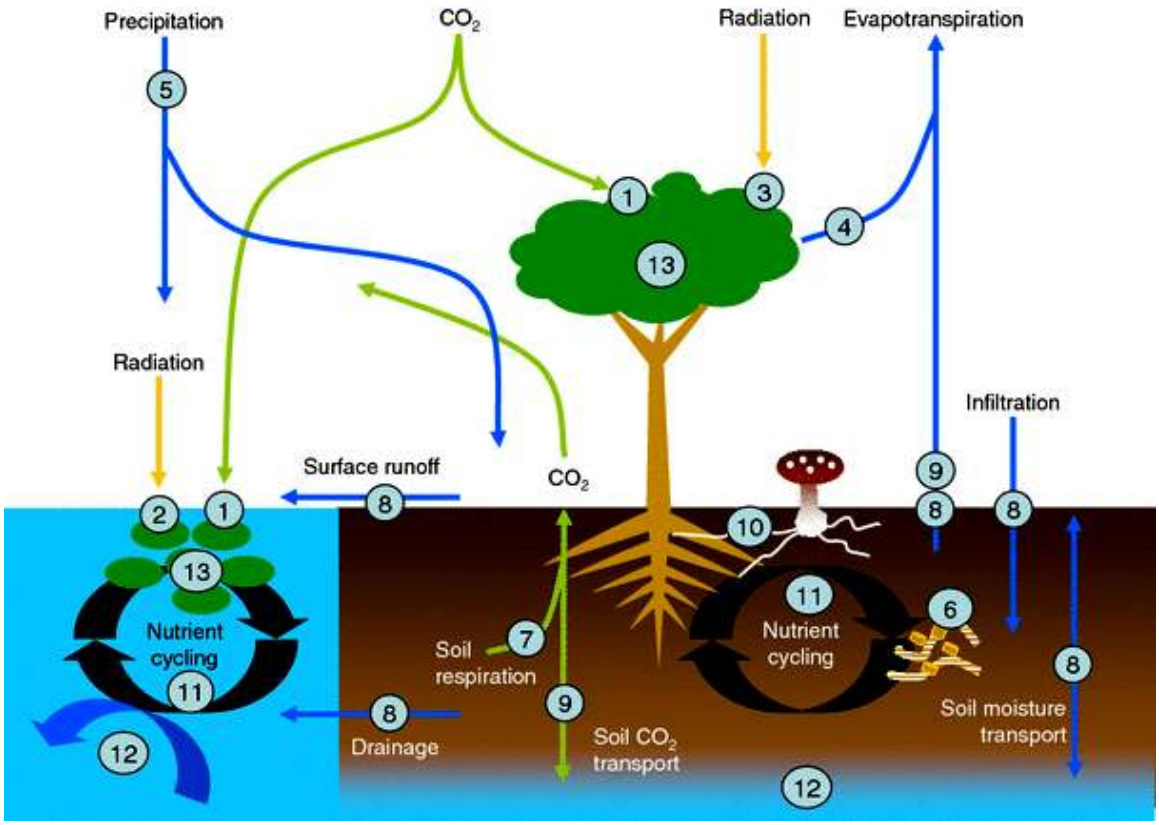

Figure 1-5. Simplified scheme of some terrestrial and aquatic ecosystem processes. Among other impacts, NPs' effects on photosynthetic organisms may reduce the fixation of CO_2 (1); NPs adsorbed (2) or deposited (3) on photosynthetically active surfaces might reduce light availability or gas exchange (4) and thus photosynthesis; NPs present in the atmosphere might increase the nuclei available for raindrop formation (5), thus altering precipitation; NPs' impacts on bacteria, fungi, and other edafic fauna (6) might affect soil respiration (7), and other soil-texture-related processes such as transport of liquids (8) or gases (9), also modifying symbiotic relationships (10). Together, this might lead to impairments in three key services provided by ecosystems, i.e., nutrient cycling (11), water depuration (12), and biomass production (13) (17).

Navarro et al. (57) and Miao et al. (58) concluded that the toxicities observed for freshwater alga *Chlamydomonas reinhardtii* and marine phytoplankton *Thalassiosira weissflogii* were due to the release of Ag^+ from AgNPs, which reduced cell-specific growth rate, photosystem II quantum yield, and chlorophyll *a* content. Likewise, the cytotoxicity attributed to CdSe QDs was also mediated by their intracellular oxidation and release of Cd^{2+}

and Se^{2-} ions (59). However, there are limited studies available on the adverse effects of QDs on plants, bacteria and algae (60, 61). It has recently been shown (62) that amphipod *Leptocheirus plumulosus* exposed to CdSe/ZnS core-shell QDs via algae resulted in high amphipod mortality. Acutely toxic Cd and Se in amphipods exposed to QDs in water were highly correlated and spatially localized within the amphipod. In contrast, when exposed to QDs via algae the metal constituents were more disperse within the algae suggesting QDs dissolution and resulting in metal ion toxicity. This study suggests QDs were accumulated to a greater extent than dissolved ion and could lead to trophic transfer since QDs ingested by algae were bioavailable to induce toxicity; such phenomenon was not observed in the absence of algae. Hence understanding the physical and ecotoxicological effects of QDs is critical for developing adequate regulatory structures to protect aquatic ecosystems from their detrimental effects.

In addition to physical adsorption/trapping and ion release, organisms may excrete compounds as a feedback response to impact nanotoxicity. Algal exudates can produce substances to induce NP flocculation or metal ion chelation and thus reduce the bioavailability of both NPs and their released metal ions (63). Exopolymeric substances production has been shown to increase in algae upon exposure to NPs, and may thus contribute to detoxification mechanisms (58).

Due to their enhanced reactivity and adsorption capacity, NPs may either increase or decrease the bioavailability of pollutants as well as themselves. Hydrophobic pollutants such as phenanthrene may sorb onto the surfaces of hydrophobic fullerenes and CNTs and increase their bioavailability to green alga *P. subcapitata* and zooplankton *D. magna* (64). On the other hand, the toxicity of diuron to green algae was reduced in the presence of carbon-

black NPs (65). Similar to inorganic NPs, micro- and nanosized plastic have been recently shown as potential carriers of harmful pollutants in the aquatic ecosystem. The following section extensively reviews the hazards posed by plastic in the aquatic environment.

1.3.2. Ecotoxicity of polystyrene nanoparticles

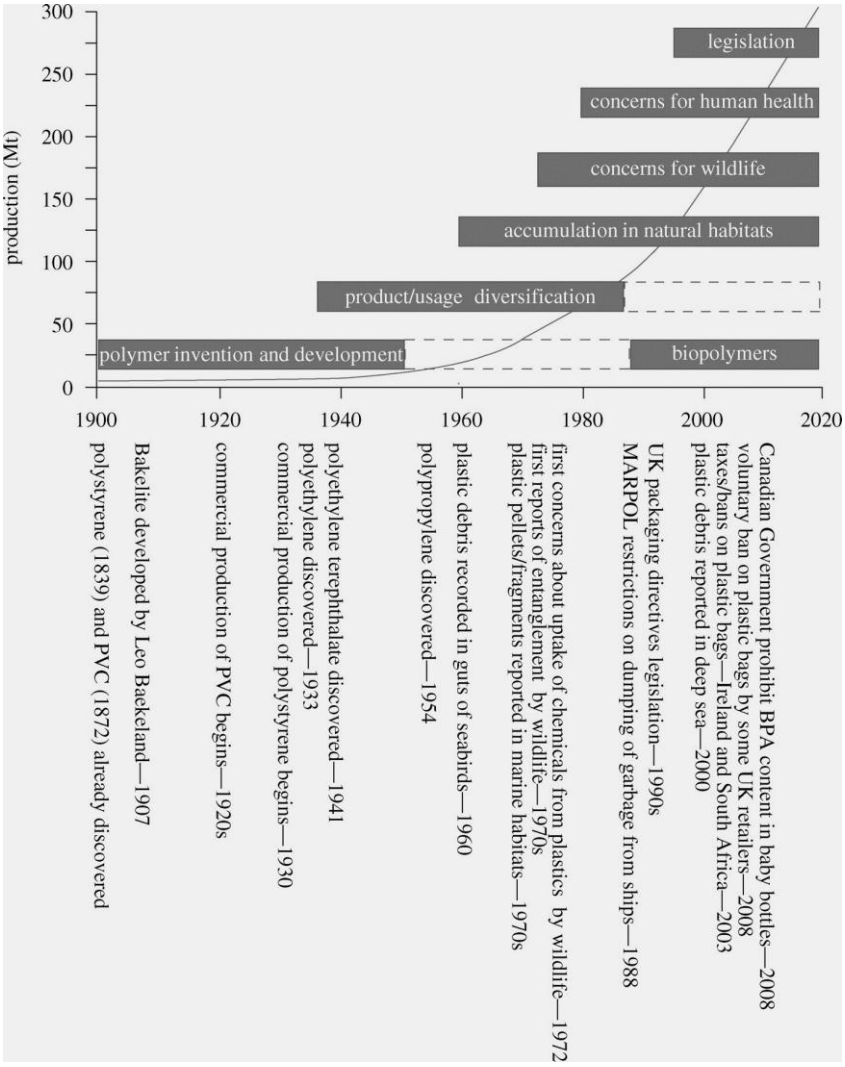

Figure 1-6. Summary illustrating historical stages in the development, production and use of plastics together with associated concerns and legislative measures. Solid grey line shows plastic production in millions of tonnes (Mt) (66).

The worldwide production and use of plastics has resulted in their increased disposal into the marine environment (67, 68). Plastics are synthetic organic polymers whose versatility has led to a great increase in their use over the past three decades, and they have rapidly moved into all aspects of everyday life (69, 70). The lightweight, strong, durable, and economic characteristics make plastics suitable for the manufacturing of a wide range of products. These same properties, however, also happen to be the causes of concern over the adverse effects of plastics in the environment (70, 71) (Figure 1-6). Since they are buoyant and slow to degrade, an increasing load of plastic debris is being dispersed over long distances, and when they finally settle in sediments they may persist for centuries (72-74).

With recent reports on the unexpectedly high incidence of plastic debris in the North Pacific Gyre (Figure 1-7) (Algalita Marine Research Foundation annual reports), research on the ecological fate of plastics has become a high priority area in Marine Biology (75, 76). Plastic debris in the marine environment is found in a wide range of sizes, from micrometers to meters (77). Due to the high resistance to degradation (77, 78), microplastics potentially persist in the marine environment (79, 80). Microplastics accumulated in the ocean can be ingested by marine biota (67, 81), and can absorb bioaccumulative and toxic compounds from seawater (82), which include organic pollutants (POPs) (83-85) and metals (86). Once ingested, the absorbed pollutants may be transferred to the respective organisms (87-92).

Figure 1-7. The Great Pacific Garbage Patch (Image courtesy of Algalita Marine Research Foundation).

Plastics such as polyvinylchloride, PS, polycarbonate, polyethylene (PE), polyester, and polyurethane have been shown to contain and release toxic monomers that are linked to cancer and reproductive abnormalities in humans, rodents, and invertebrates (93). In addition, microplastic particles have been found to adsorb, concentrate, and transport hydrophobic contaminants from seawater into marine organism tissue. Low levels of polychlorinated biphenyls, dichlorodiphenyl, trichloroethane, and nonylphenol in seawater have been shown concentrated several orders of magnitude at the surfaces of plastic particles. In a recent study, phenanthrene-contaminated PE particles evolved into marine

sediments, significantly enhancing accumulation of this potentially toxic agent into the tissues of marine benthic organisms (94).

Most studies have been focused on quantifying the abundance of plastic in the marine environment. There is a lack of understanding in how and to what extent microplastics can pose a toxicological hazard. Plastic particles in the marine environment undergo slow but steady degradation through physical processes like collision induced abrasion, exposure to sunlight, and chemical processes. Dense plastic particles are more susceptible to collision than lighter ones (95), and photo-oxidation can functionalize the surface of plastics (96). Smaller plastic particles pose more danger to the ecosystem since they can easily mix with food items (97) and be ingested by marine organisms. Also, owing to their smaller size and higher surface area, plastic can adsorb pollutants such as polyaromatic hydrocarbons (PAH) to a greater extent (92, 98). Studies (99, 100) have drawn attention to an inconspicuous and previously overlooked form of plastics pollution: small fragments of plastic (usually up to 0.5 mm across) derived from hand cleaners, cosmetic preparations and airblast cleaning media. The environmental impact of these particles, as well as similar sized flakes from degradation of larger plastic litter has not been properly established yet. The most common plastics found in the ocean are PE, polypropylene (PP) and PS, the last of which is most commonly used for packaging (95). In 2006, the U.S. disposed of 870,000 tons of PS plastic plates and cups (plus 590,000 tons on other PS products), according to the United States Environmental Protection Agency (US-EPA)'s report on Municipal Solid Waste (101). PS microplastics amongst other types of plastic formed from the fragmentation of larger items and spillage of plastic products and pellets

have been found to contaminate the shorelines of 18 sites worldwide representing six continents (102).

PS takes decades to hundreds of years to dissolve. Instead, it photo-degrades extremely slowly into progressively smaller pieces. Among the above mentioned most commonly found plastics in the ocean, PS is also the densest (103). Erosion may lead to decreases in the specific density of PS, thereby enhancing its buoyancy (104). In New Zealand and Canada, PE and PS scrubber grains respectively were identified in the cleansing preparations available in those markets, sometimes in substantial quantities (100). Several studies indicated the hazards to marine biota imposed by PS particles. In the Bristol Channel in the summer of 1973, 21% of the flounders (*Platichthyes flesus*) were found to contain PS spherules (105). The same study found that in some areas 25% of sea snails (*Liparis liparis*) were heavily contaminated by such debris. In the New England coast the same type of spherules were found in 8 out of 14 fish species examined, and in some species 33% of individuals were contaminated (106). In addition, according to Zitko (107), low molecular weight compounds from PS particles were leached by seawater, and the fate and effects of such compounds on aquatic biota remained unknown. Despite of the environmentally adverse potential of PS, no published studies existed prior to this dissertation on their impacts on algae – a primary food source for marine biota.

Plastic debris floating at sea may acquire a fauna of various organisms such as bacteria, diatoms, algae, barnacles, hydroids and tunicates (90, 106, 108, 109). Such debris loaded with marine organisms can drift and be transported across the ocean thus increasing the range of certain marine organisms or introducing species into an environment where

they are previously absent (110). Such arrival and invasion of unwanted and aggressive alien taxa can be detrimental to marine ecosystems (111).

Micro- and nanoparticles of plastic used in consumer products (112) are introduced directly into the oceans via runoff. These include the micron-sized plastic particles typically used as exfoliants in cosmetic formulations (100, 113), those generated in ship-breaking industry (114), and industrial abrasives in synthetic 'sandblasting' media (beads of acrylic plastics and polyester). Engineered plastic NPs derived from post-consumer waste as well as from meso-/microplastics via degradation pose a specific challenge to the ecosystem. Small eukaryotic protists, diatoms and flagellates that measure in the range of 200 nm to a couple of microns are abundant in the oceans. Recent studies based on quantifying their photosynthetic pigments indicate that nano- and picoplankton are not only the predominant groups of plankton biomass but also the major contributors to primary production (115). As plastic NPs are of a comparable size, understanding their mechanisms of interaction with the nano- or picofauna is particularly important.

While limited data on the interaction of NPs with biota is available, these studies have been for the most part focused on non-organic, engineered NPs (ENPs) such as oxides, metals, CNTs, and QDs per discussed. Though these NPs have shown different levels of toxicity to algae, such data cannot be reliably extrapolated to polymer NPs. Inorganic NPs may carry some POPs via surface absorption but plastic NPs are expected to have much higher levels of matrix-solubilized POPs. Data on the effects of plastic NPs on marine flora and fauna (15, 116) are limited and hence an attempt to elucidate the mechanisms of the effects of plastic nanoparticles on algal growth and biological functioning has been made in this dissertation.

In addition to a myriad of assessments of the environmental implications of nanomaterials, there has been a considerable effort underway exploring use of nanomaterials in applications such as membrane separation, catalysis, adsorption, and strategic analysis of environmental protection. Accordingly, Part II of this dissertation is focused on the environmental applications of nanomaterials. Specifically, the following section provides an extensive literature review on the use of nanomaterials in water treatment applications.

1.4. Environmental Applications of Nanomaterials

Water shortage is a paramount challenge facing populations of both developed and developing nations. Worldwide, 1.1 billion people lack access to sufficient amounts of safe water (117). Also, industry relies on large quantities of clean water during manufacturing, which is then returned to the environment. Hence, adequate supplies of decontaminated water with high throughput at a low cost are a growing challenge around the world. Since the 19th century, urgent solutions to water quality problems have been conjointly addressed through an interdisciplinary approach - a convergence of physical sciences, biology, environmental engineering and information science. Current water purification methods in wide use employ chemically intensive treatment that is relatively expensive, harmful to the environment, and is not adaptable to the non-industrialized world. In general, they include physical processes such as filtration and sedimentation, biological processes such as slow sand filters or activated sludge, and chemical processes such as flocculation and chlorination, and the use of electromagnetic radiation such as UV light for reducing the concentration of particulate matter including suspended particles, parasites, bacteria, algae, viruses, fungi, and

a range of dissolved and particulate material derived from the surfaces that water may have made contact with after falling as rain.

Sources of drinking water include groundwater, lakes and reservoirs, rivers and canals, and desalinated sea water. While deep groundwater is of very high bacteriological quality, it may still have a high concentration of dissolved solids such as salts of calcium and magnesium. Lakes and reservoirs generally have a high humic content besides dissolved solids, whereas rivers and canals have high levels of bacterial activity, algae, and other suspended solids and dissolved constituents. Treatments of water from the above sources usually include the following steps:

1. *Pre-treatment* – Surface water is screened to remove large debris such as sticks, leaves, trash, and other particles which may interfere with subsequent treatment processes. Deep groundwater usually does not need to be screened. Water rich in hardness salts is also treated with sodium bicarbonate to precipitate out calcium carbonate using the common-ion effect (reduction in solubility of an ionic precipitate by adding one of the ions of the precipitate in equilibrium with the precipitate). A pH adjustment is done following the above processes to make water neutral for potable purposes.
2. *Flocculation* – This process removes turbidity and clarifies water by forming removable precipitates. Flocculation is a process by which small precipitates coagulate to form bigger precipitates which can then be removed by filtration. Commonly used flocculants include iron hydroxides - being insoluble at and above a pH of 7, aluminium hydroxides – a severe poisoning incident in 1988 at Camelford in south-west UK raised concerns about this method of flocculation, and polyDADMAC – a high molecular weight synthetic polymer that forms readily removable flocs but is an expensive alternative to

inorganic materials. Following flocculation, sedimentation of the flocs is carried out in a large tank.

3. *Filtration* – After the floc is separated, water is filtered to remove remaining suspended particles and unsettled floc. The most common filter is a sand filter in which water moves vertically through a layer of sand topped with anthracite coal. The activated carbon removes organic content. Such filters can be usually regenerated by backwashing, i.e. passing water quickly upward through the filter to remove embedded particles. Membrane filters are used to filter out any particles usually larger than 0.2 μm. However, such filters cannot filter out dissolved phosphates, nitrates and heavy metal ions.
4. *Disinfection* – As a final step, water is disinfected from any harmful microbes and pathogens by adding disinfectants like chlorine (in the form of gaseous chlorine ad sodium hypochlorite) due to its strong oxidizing potential. One drawback of chlorination is that on combination with natural organic matter (NOM), it forms potentially harmful chemical by-products such as trihalomethanes (THM) and haloacetic acids (HAA) - both of which are carcinogens and are regulated by government agencies such as the US-EPA. To get around this problem, ozone disinfection is widely used. Ozone, or O_3, is an unstable free radical species of oxygen which readily gives up one atom of oxygen. Being a strong oxidant, this free radical is toxic to most microbes and pathogens, and leaves behind relatively less harmful by-products. Another form of disinfection used is UV radiation. Absorption of UV light by DNA and proteins in microbial cells results in the inactivation of the microorganisms. Using a combination of two wavelengths – 185 nm and 254 nm - photooxidation of organic compounds is achieved thus reducing the

amount of total organic carbon to < 5 ppb. However, the main disadvantage of both ozone and UV treatments is that they have to be created on-site for disinfection and leave behind no residual disinfectant. Hence, a combination of the above three methods is often used.

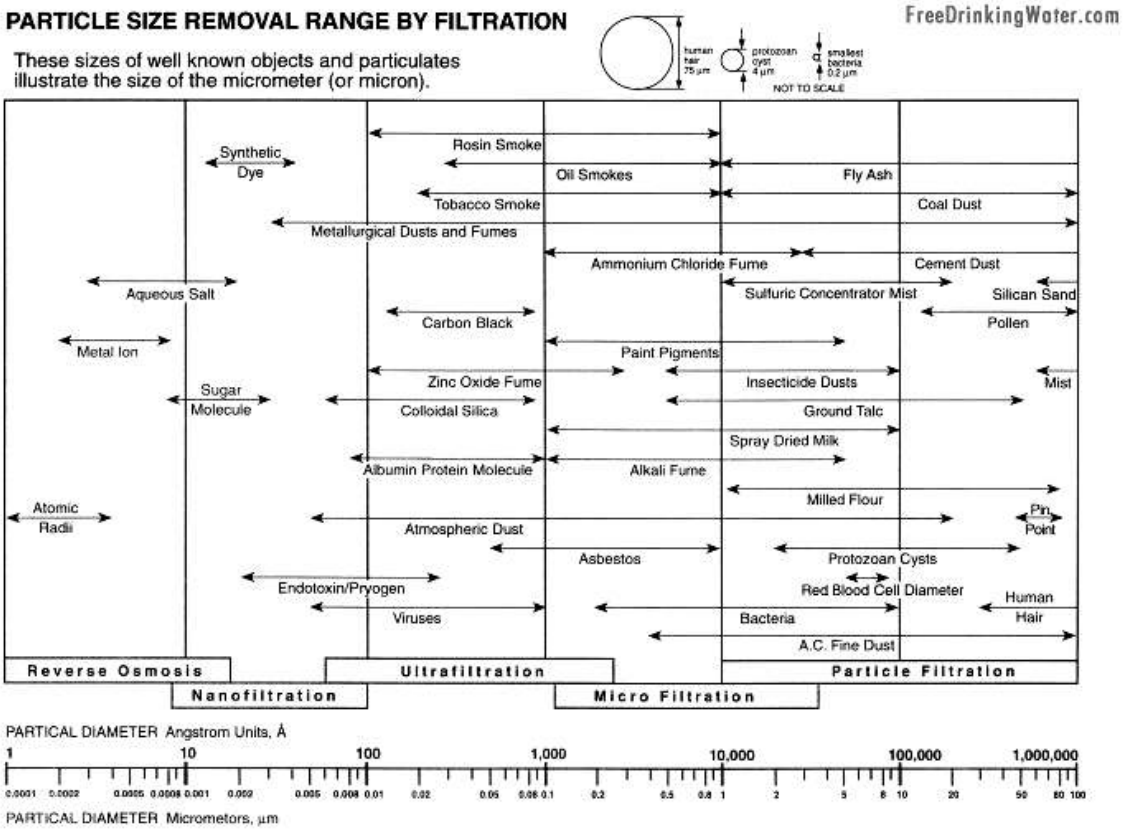

Figure 1-8. Summary of conventional water filtration technologies based on the size of the particles to be removed (Image courtesy of freedrinkingwater.com).

The most common water purification and filtration (Figure 1-8) technologies are discussed below, with their advantages and disadvantages listed.

1. *Distillation* – This is the oldest method of water purification wherein water is boiled and the resultant water vapor is condensed, collected, and stored. However, organics such as herbicides and pesticides, with boiling points lower than 100°C cannot be removed by distillation. It is also a costly method, requires large amounts of energy and water, and hence is usually used on industrial scales. Distilled water can also be very acidic and lacks oxygen and essential minerals and is deemed unsuitable for drinking.
2. *Ion Exchange* – Water percolates through bead-like spherical resin materials called ion-exchange resins. Ions in water are exchanged with other ions in the resins. The two most common ion-exchange methods are *softening* and *deionization*. Softening is a step prior to reverse osmosis. The softeners contain beads that exchange two benign sodium or potassium ions for every calcium or magnesium ion removed. Deionization (DI) involves exchange of hydrogen ions for cations or hydroxyl ions for anions. The hydrogen and hydroxyl ions then combine to form water (Figure 1-9). The cation resins are usually made of styrene and divinylbenzene containing sulfonic acid groups, and the anion resins of styrene containing quaternary ammonium groups. The resins need to be regenerated once all the ions in them have been exchanged. Hence, although the initial capital investment is inexpensive, ion exchange involves high operating costs over longer terms. Also, DI does not remove organics and microorganisms.

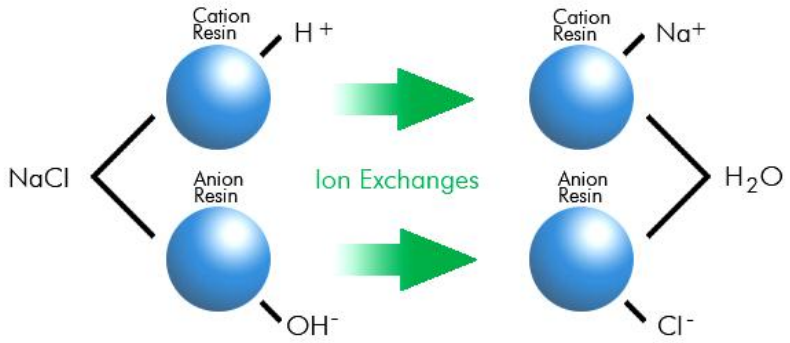

Figure 1-9. Ion exchange processes (Image courtesy of <http://www.freedrinkingwater.com/water-education/quality-water-filtration>).

3. *Activated Carbon* – This method effectively removes most chemicals and gases and in some cases, can be effective against microorganisms. However, it does not treat total dissolved solids, heavy metals, or hardness. Two types of carbon filters are usually used – granular activated carbon and solid block carbon. The advantage of activated carbon stems from its large effective surface area (60-150 acres per lb). They are created from a high-temperature process in which a matrix of millions of microscopic pores and crevices are formed. The pores trap microscopic particles whereas the activated surface adsorbs smaller organic molecules. Thus the adsorption process is controlled by the size of the pores and diffusion rates of the organic molecules through the pores. Certain granular carbons can effectively remove chloroamines and free chlorine. However, carbon filtration is associated with a big disadvantage of creating toxic carbon fines.
4. *Microfiltration (MF) and Ultrafiltration (UF)* – There are three types of microporous filtration: depth, screen, and surface (Figure 1-10). Depth filters have large pores on the

top surface so that particles pass into the interior of the membrane. These particles are then either trapped at constrictions in the membrane pores made of matted fibers or materials compressed to form a matrix, or by adsorption onto the pore walls (118). Screen filters are uniform structures which have small pores in the top surface, and collect particles larger than the pore diameter on the membrane surface. Surface filters are made from multiple layers of media. When fluid passes through the filters, particles larger than the spaces within the filter matrices are retained, accumulating primarily on the filter surfaces. Depth filters are usually used as prefilters because they are an economical way for removing 98% of suspended solids due to their much larger surface area and protect elements downstream from fouling or clogging whereas screen filters rapidly become clogged due to retention of particles at the top surface. Microfiltration usually operates between 200-700 kPa pressure, but are not effective in removing dissolved organic and inorganic solutes with molar mass <3 kDa since small and linear polymers can snake through the pores. UF uses finely porous polymer membranes that can be used to filter out dissolved substances avoiding the use of coagulants. The average pore diameter ranges between 10 – 1000 Å. This technique probably produces the highest quality water for the least amount of energy and is regenerable. However, in all cases, the membranes will retain most, but not necessarily all, molecules above their rated size, like dissolved inorganics. The principal issue with UF is membrane fouling sometimes requiring cleaning every 2-3 weeks (118). Increasing the hydrophilicity of the membrane surface or changing surface charge decreases fouling and increases the flux.

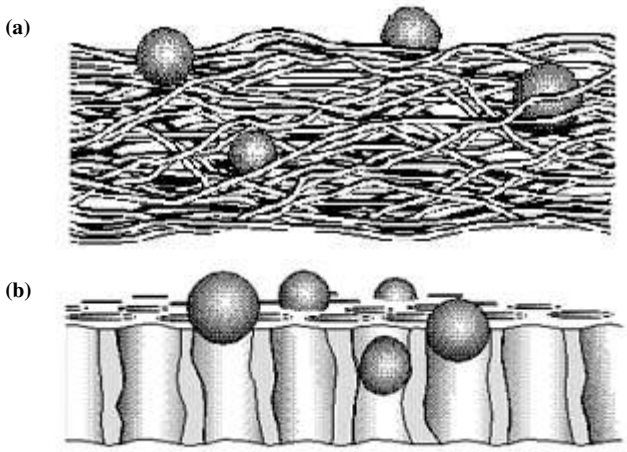

Figure 1-10. Schematic of (a) screen and (b) depth filtration (Image courtesy of <http://www.h2ro.com/_Solutio2.htm>).

5. *Reverse Osmosis (RO)* – Till date, it is one of the most economical ways of producing the highest quality of drinking water by removing nearly 90-99% of all contaminants. The pore structure being much tighter than MF membranes, RO memebranes are capable of removing most particles, bacteria and organics >300 Da, including pathogens. Natural osmosis occurs when solutions with two different concentrations are separated by a semi-permeable membrane. Osmotic pressure drives water through the membrane and equilibrium is reached when the concentration of the solutes on both sides of the membranes is same. In RO, a membrane which is permeable to water but impermeable to the solutes is used. Applied hydraulic pressure at the feed side of the membrane to the concentrated solution counteracts the natural osmotic pressure. Pure water is driven from the concentrated solution and collected on the other side of the membrane (Figure 1-11). The semi-permeable membrane rejects salts (ions) by a charge phenomenon action: the greater the charge, the greater the rejection. Therefore, the membrane rejects

nearly all (>99%) strongly ionized polyvalent ions but only 95% of the weakly ionized monovalent ions like sodium. It is highly effective in removing several impurities such as total dissolved solids, asbestos, lead and other toxic heavy metals, radionuclides, chlorinated pesticides, most heavier weight volatile organic carbons, and many dissolved organics. A combined use of RO and activated carbon could be the most effective treatment in the broadest range of water impurities and contaminants. But, because RO membranes are very restrictive, they yield slow flow rates, typically certain gallons/day. Storage tanks are required to produce an adequate volume in a reasonable amount of time. Perfect semi-permeable membranes are also difficult to create and if not well-maintained, bacterial forms can colonize the membranes. In addition, to obtain high quality water, typically 400-1000 lb/in^2 pressures have to be applied (119), making the process energy inefficient.

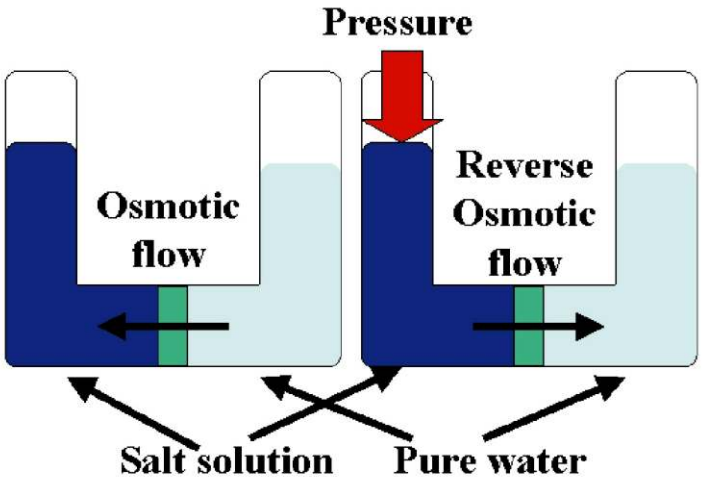

Figure 1-11. Schematic of a RO system (Image courtesy of Reverse Osmosis, Oracle ThinkQuest).

Somewhere between UF and RO lies *Nanofiltration (NF)*. The pore size of a NF membrane is ~1 nm with a molecular weight cutoff (MWCO) of less than 1000 Da. Hence, they can effectively remove low total dissolved solids containing cations, NOM, biological contaminants, organic pollutants, nitrates, and arsenic from groundwater and surface water (120). NF typically operates at lower pressures (3 MPa) than RO and hence is more cost effective for desalination (121). A combination of RO and NF could prove more effective in producing potable water from brackish water. However, NF membranes are still subject to fouling, like RO.

It can be noted from above that each purification technology removes a specific type of contaminant and none can be relied upon to remove all contaminants to the levels required for drinking and critical applications. A well-designed water purification system uses a combination of purification technologies to achieve best water quality, making the process costly and bulky. Furthermore, each of the purification technologies must be used in an appropriate sequence to optimize their particular removal capabilities. In December 2007, the US-EPA released a detailed poster identifying treatment technologies that remove multiple contaminants, including information on contaminants removed, operational and waste disposal issues, and helpful tips (EPA 816-H-07-004, December 2007) (Figure 1-12).

EPA United States Environmental Protection Agency

Removing Multiple Contaminants from Drinking Water: Issues to Consider

Public water systems that need to add treatment for one contaminant may find that they also have other water quality concerns. Choosing a treatment technology that can remove several co-occurring contaminants may be more efficient and cost effective. This table describes treatment technologies that can remove multiple contaminants, identifies the contaminants that can be removed, and summarizes related operational and waste disposal issues.

Removal Technology	Arsenic	Fluoride	Microbes	Nitrate	Radium	Uranium	Other	Operational Issues	Waste Disposal Issues
Activated Alumina (AA) Uses a porous aluminum-based material to adsorb certain contaminants.	✓	✓				✓	selenium	• Other ions may competitively adsorb and displace contaminant. AA is optimized at a pH of 5.0 to 5.5; pH 5.0–6.0 is optimal for arsenic removal. Other ions, or removal of multiple ions will cause more frequent regeneration and require careful monitoring to prevent breakthrough. • What arsenic is present in the form As(III), pre-oxidation is necessary to convert it to the form As(V). • Must be backwashed periodically to prevent clogging. • Must be periodically regenerated. • System is low cost, easy to operate, and requires minimal operator attention.	• Wastes include backwash water, brine, rinse water, and acid neutralization water as well as spent filter media. • Levels of arsenic and radionuclides will likely dictate options for spent media disposal. • Pretreatment may be needed for disposal to a sanitary sewer.
Anion Exchange A physical-chemical process in which ions are swapped between a solution phase and a solid resin phase. The solid resin adsorbs anions and releases chloride into the water.	✓	○		✓		✓		• pH of 6–8 in the treated water will maximize uranium removal and optimize resin regeneration. pH 6.3 to 9.0 is optimal for resins. • What arsenic is present in the form As(III), pre-oxidation is necessary to convert it to the form As(V). • Uranium is the strongest binding contaminant, followed by arsenic and then nitrate. Uranium is so strongly adsorbed that it may be difficult to regenerate the resin. Less strongly binding contaminants may breakthrough if not carefully monitored. • Sulfates, nitrates, and other ions compete for adsorption sites. • High dissolved solids (levels >500 mg/L can adversely affect treatment performance. • Precipitated iron, manganese, and silica will foul resin and require cleaning. • Contaminant breakthrough can be avoided by careful monitoring and by running several columns in series, keeping the most recently regenerated column last. • Required operator skill level is intermediate.	• Wastes include backwash water, regenerant brine, rinse water, and spent media. • Resins have a high capacity for adsorbing arsenic, radium, and uranium which will likely dictate options for spent media disposal. • Pretreatment for spent brine may be needed for disposal to the sanitary sewer.
Ion-Based Adsorptive Media Ion-based adsorptive media to adsorb contaminants.	○				○	○	antimony	• When arsenic is present in the form As(III), pre-oxidation is necessary to convert it to the form As(V). • Metal ions compete with arsenic for adsorption sites, which can affect treatment performance. • If pH adjustment or pre-oxidation step is lost, treated water may have an arsenic spike. • Phosphate and silica compete with As(V) for adsorption sites. • Backwash is required to remove particulates and to redistribute media. Frequent or improper backwash can result in media loss. • Bacteria can accumulate in the media during low flow and hot weather. • When removing multiple contaminants the weaker adsorbing contaminant can breakthrough if not carefully monitored. • System is low cost, easy to operate, and requires minimal operator attention.	• Backwash water can be easily recycled through the treatment plant to maximize water conservation, or it can be discharged to a sewer, septic system, or surface water. • Testing is needed to ensure spent media is not hazardous or radioactive.
Mixed Bed Ion Exchange Anion and cation exchange resins can be combined in a single ion exchange unit to remove cationic (e.g. cadium) and anionic (e.g. arsenic, uranium) contaminants.	✓				✓	✓	sulfate, magnesium, calcium	• Cadmium competes at pH as >10.5 for cadium removal and 6.10 for uranium. • Sulfate and uranium can displace arsenic from the resin, causing a spike of arsenic in the treated water. • Contaminant breakthrough can be avoided by careful monitoring and by running several columns in series, keeping the most recently regenerated column last. • May be necessary to increase treated water alkalinity after ion exchange to reduce corrosion in the distribution system. • Intermediate operator skill level required.	• Wastes include spent regenerants and spent media that may have elevated concentrations of radium and arsenic which will dictate disposal methods. • Pretreatment may be needed for disposal to the sanitary sewer.
Greensand Filtration Uses manganese-coated filter media to oxidize and adsorb contaminants.	✓				✓		iron, manganese up to 10 ppm	• High iron to manganese ratio may lower radium adsorption on greensand filters, but the presence of iron is beneficial to arsenic adsorption. • Arsenic removal by greensand requires a pH >6.8. Radium removal improves as pH increases over the range from 5 to 9. • Minimal operator attention and maintenance requirements; requires operator skill level is basic. • Cost-effective for radium removal at small systems.	• Wastes generated include sludge and augmentant from the filter backwash as well as spent filter media. Radium and arsenic levels will dictate disposal options.
Oxidation/Coagulation/Filtration Involves adsorption of contaminants to an aluminum or ferric hydroxide precipitate and removal of these particles by filtration.	✓	○				✓	iron, manganese	• When arsenic is present in the form As(III), pre-oxidation is necessary to convert it to the form As(V). • 20:1 iron to arsenic ratio will improve iron removal. • Ferric chloride is typically used as the source of iron. • Arsenic removal is less effective at higher pH. • Coagulating costs are relatively low. • Advanced operator skill level required. • Optimum pH for uranium removal is 6.0.	• Wastes generated include iron and alum sludges from the contact and settling basins, the supernatant from the sludge, filter backwash, and spent filter media. Additional liquid waste may be generated when the sludge is de-watered prior to landfill disposal. • Backwash water is typically discharged to a sewage or septic system. • High concentrations of uranium may dictate disposal options.
Lime Softening Removes hardness by precipitating out calcium and magnesium carbonates.	✓				✓	✓	hardness	• pH >10 is needed for radium removal. Uranium removal requires pH >10.5 and is improved by adding magnesium carbonate. • Advanced operator skill level required. • Treatment costs are high and may not be a cost-effective alternative for small systems. • It may be necessary to increase alkalinity for corrosion control.	• Wastes include a high volume of lime sludge which precipitates with radium and/or uranium, supernatant from the sludge, and filter backwash. • Testing is needed to ensure spent media is not hazardous or radioactive.
Reverse Osmosis (RO) A pressure-driven membrane separation process that removes contaminants larger than the membrane pores.	✓	✓	✓	✓	✓	✓	TDC, most metals, sulfate, calcium, magnesium, potassium, phosphorous	• RO membranes fail easily, so pretreatment to remove particulates and organics may be necessary. • Calcium and magnesium can cause membrane fouling. • Cellulose acetate membranes are susceptible to biological fouling; free chlorine can be beneficial up to 1 mg/L. • Polyamide membranes can be damaged by chlorine, high iron, and chloramines. • Depending on operating parameters, 20 to 40% of raw water can be lost in the reject stream. • Advanced operator skill level required. • Treatment costs are higher than other treatment options.	• Wastes consist of concentrated waste stream and spent membranes which may contain elevated levels of radionuclides. • Testing is needed to ensure spent media is not hazardous or radioactive.

Notes: Best Available Technologies (BATs) specified in regulations are indicated by ✓. Technologies that are effective but not currently listed as a BAT are indicated by ○.

TIPS

- ✓ **More frequent monitoring and shorter run times may be necessary to prevent breakthrough of weaker absorbing contaminants for certain technologies.**
- ✓ **While a technology may be able to remove multiple contaminants, operating parameters such as optimal pH may very for each contaminant. Adjustments may be necessary to maximize treatment for the combined contaminants.**
- ✓ **In addition to cost, ease of operations and operator qualifications should be considered.**
- ✓ **Pre-oxidation may be necessary for maximum removal of certain contaminants.**
- ✓ **When considering treatment efficacy, evaluate whether a series or parallel configuration will work best to prevent breakthrough of contaminants.**
- ✓ **Testing may be needed to determine if spent media is hazardous or radioactive. If waste residuals contain certain radionuclides such as uranium or therium, they may be subject to the Nuclear Regulatory Commission's licensing requirements.**

For more information:

EPA Office of Water Safewater site – http://www.epa.gov/safewater

EPA Office of Research and Development Drinking Water Research site - http://www.epa.gov/ord/dw/

Safe Drinking Water Hotline – 1-800-426-4791

Figure 1-12. Operational issues with removing multiple contaminants from drinking water (Image courtesy of US-EPA).

It can be seen that all the conventional water treatment technologies have associated disadvantages. Nanomaterial-based membrane technologies, adsorbents and catalysts could create new generations of technologies and novel environmentally benign solutions for potable water treatment and groundwater remediation. They could serve three main purposes – sensing and detection of pollutants, treatment and remediation of contaminants, and finally, prevention of pollution. For example, in groundwater remediation, environmental engineers employ a pump-and-treat technique which pumps out the groundwater and re-injects it after treating for contaminants. This entire process is cost-inefficient and mostly incapable of meeting cleanup goals (122). As a result, *in situ* treatments such as biodegradation have been explored extensively. For this, zero valent iron (ZVI) and catalysts have been used to promote redox reactions that degrade contaminants (123). Nanomaterials have been developed to promote such reactions at high rates; however, successful applications of this technology require high degree of control of nanoparticle mobility, reactivity, and ideally, specificity for the contaminant of interest.

Nanomaterials are also being used to enhance membrane separation processes, leading to greater selectivity and lower costs. Stimulated by the huge potentials of nanomaterials for environmental remediation, there is a body of literature growing on the use of various nanomaterials for potable water treatment. Below is an extensive review of such literature involving nanomaterials.

1.4.1. Nanomaterials for water treatment

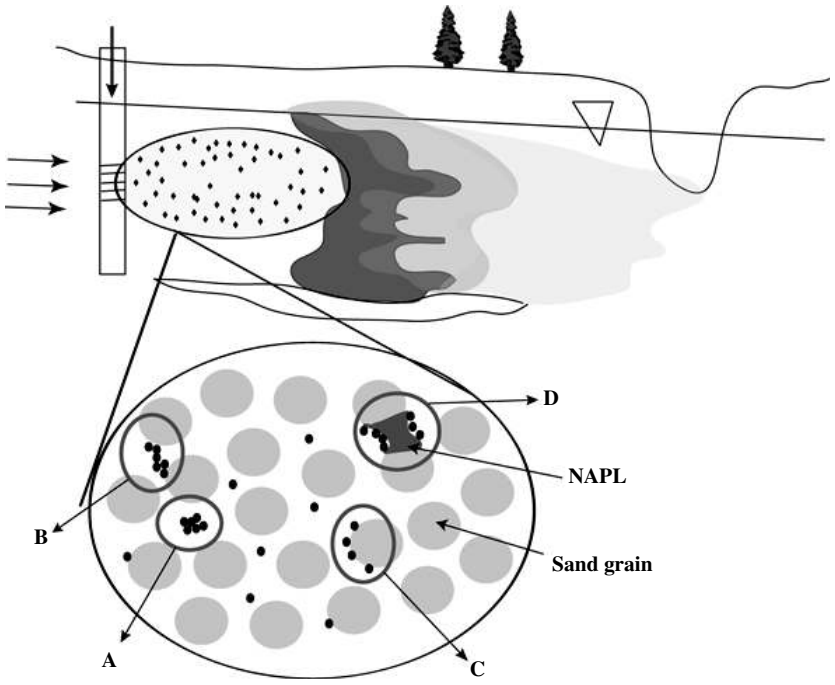

Figure 1-13. Illustration of denser than water non-aqueous phase liquid (DNAPL) distribution as residual saturation (sources) and a plume of dissolved contaminants in an aquifer. Nanotechnology offers the potential to effectively target the chemical treatment to the residual saturation zone in situ. Reactive nanoparticles are injected into the aquifer using a well. The particles are transported to the contaminant source where they can degrade the contaminant. Nanoparticles can aggregate (A) and be filtered from solution via straining (B) or attachment to aquifer grains (C). Methods to target the nanoparticles to the contaminant (D) could improve the efficiency of the technology (124).

Nanotechnology has the potential to create novel and effective *in situ* treatment technologies for groundwater contaminant source zones (Figure 1-13). For example, highly reactive NPs such as nanoscale zerovalent iron ("nanoiron" or NZVI) (125) (Figure 1-14), nanocatalysts (e.g., Au/Pd bimetallic nanoparticles (126)), or nanosized sorbents (127) have been developed specifically to remediate contamination by organic and inorganic contaminants. Their small size, typically of 10–500 nm, makes their delivery to subsurface contaminants *in situ* possible and provides access to contamination trapped in the smallest

pores in an aquifer matrix. In addition, the high reactivity of nanomaterials can accelerate degradation rate of contaminants in the source zone, making the contaminants innocuous, or adsorb and/or complex with the nanomaterials to become immobile, thus decreasing the time and cost of remediation relative to traditional treatment technologies.

Most commonly used nanomaterials for water treatment are categorized into the following:

A. *Inorganic reactive nanomaterials* - Several documented applications of NZVI ranging from pilot to full-scale show that they can be cost-effective in remediating groundwater (123). For example, NZVI remediates groundwater from trichloroethylene (TCE) without creating chlorinated intermediates unlike other *in situ* treatments, polychlorinated biphenyls (PCBs), chlorinated aliphatic and aromatic hydrocarbons, hexavalent chromium, chlorinated pesticides, and perchlorate. Since iron is a strong reductant, when injected into a contaminated site it oxidizes with the contaminants and makes them less or non-toxic through redox reactions where ZVI gets oxidized and the generated electrons reduces the contaminants (Equations 1-1 and 1-2). Here, Me is a metal ion.

$$Fe^{0} \rightarrow Fe^{2+} + 2e^{-} \quad (1\text{-}1)$$

$$Me^{a+} + be^{-} \rightarrow Me^{a-b} \quad (1\text{-}2)$$

The particles are no longer active once all the ZVI have been oxidized. One concern to keep in mind is the transport and aggregation kinetics of nanomaterials in groundwater remediation. High deposition and aggregation rates of nanomaterials in the subsurface could limit their transport before reaching the contaminant site (Figure 1-14).

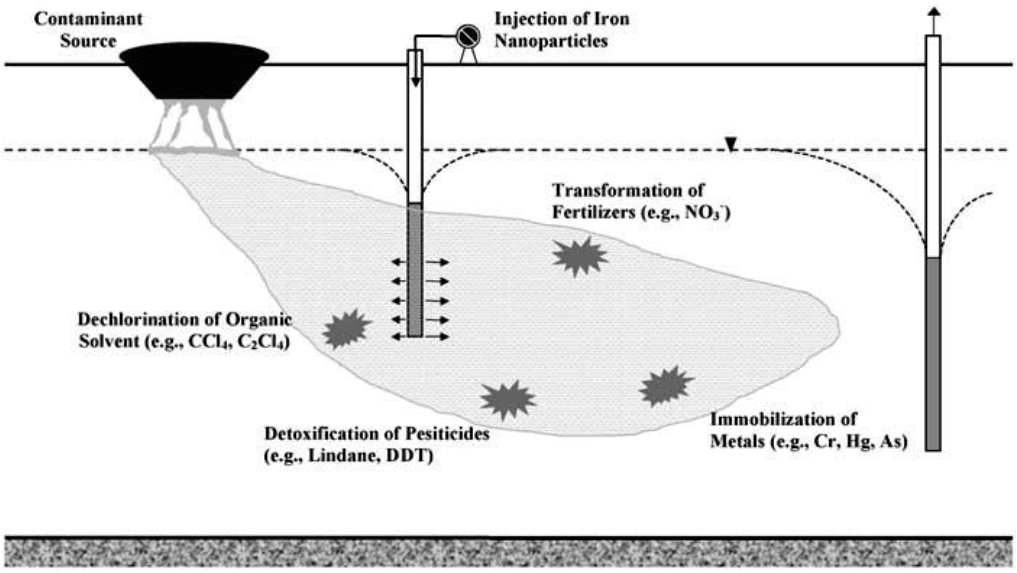

Figure 1-14. Nanoscale iron particles for in situ remediation (128).

Research has shown that NZVI worked five times better than conventional iron filings or powder for the same weight since the surface area of NZVI is 10 – 50 m^2/g, as compared to 0.01 – 1 m^2/g surface area of iron filings (129, 130). The US-EPA conducted several pilot studies, one of which injected 100 kg of iron NPs suspended in approximately 10,000 L of water. The study showed promising results in terms of removing contamination and now the US-EPA is planning a full-scale system (131). However, the reactivity and lifetime of reactive nanomaterials depend upon any processes that affect the nanomaterial surface properties (e.g. formation of iron oxide on the surface). In addition, any oxidant such as O_2 and NO_3^- that out-competes the contaminants will consume the electrons released by the reactive

nanomaterial. Also, harmful reaction products such as vinyl chloride and dichloroethane, both classified as carcinogens, may be produced during the process.

As new nanomaterials like NZVI are being used widely in environmental remediation, their ecological effects should be examined. It remains unclear how these particles will affect the microbial ecosystem, and the property of iron that makes it useful for removing contaminants could also be lethal to cells and micro-organisms. A recent study found that iron NPs are toxic to neural cells (132). Micro-organisms are essential for healthy soil as they recycle nutrients by decomposing dead matter, remediate the soil from contaminants as well as immobilize heavy metals (133). Thus during remediation efforts, excess use of iron could harm the ecology unintentionally by limiting the micro-organisms (134).

Besides NZVI, TiO_2 NPs also show promise for water treatment due to their photocatalytic activity (135, 136). The versatility of TiO_2 in treating water contaminated by both organic and inorganic contaminants stems from redox potentials under UV light (137, 140). TiO_2 NPs can be used in combination with activated carbon or biodegradation (hybrid processes) owing to their antibacterial properties. As predescribed in section 1.4., although UV effectively inactivates waterborne bacteria and protozoa cysts and oocysts, it is not very effective for viral pathogens. However, UV light is capable of activating photocatalytic materials such as TiO_2, which are then capable of inactivating viruses. Moreover, new photocatalysts such as TiO_2 doped with nitrogen (TiON), or co-doped with nitrogen and a metal such as palladium, can be activated with visible light (138) or even with sunlight, making the process both energy and cost effective. Similarly, AgNPs also

possess anti-bacterial material properties and can decompose toxic halo-organic compounds such as pesticides into non-toxic organic products (139).

B. *Carbon-based nanomaterials* – CNTs might be powerful adsorbents for the removal of organic and inorganic trace pollutants (140, 141) due to their high surface area and capability of surface functionalization. For example, Li et al. (142) found that multi-walled CNTs (MWCNTs) had a sorption capacity 3-4 times larger than activated carbon and granular activated carbon toward heavy metals Pb(II), Cu(II) and Cd(II). Further, cerium oxide-supported CNTs (CeO_2-CNTs) could effectively adsorb As(V) (143). Li et al. (144) showed that surface oxidation of CNT led to an increasing adsorption capacity for Cu^{2+}. However, large-scale application of carbon nanomaterials so far is limited by the high production costs of CNTs and concerns over their regeneration and environmental deposition (145, 146). Also, competitive sorption of other aromatic compounds such as NOM might reduce their performance efficiency (147). Moreover, if water is held in the carbon block for a long period, microorganisms can grow inside to result in fouling and contamination. Recent research has shown that double-walled CNTs can transport water three orders of magnitude faster than that predicted by continuum hydrodynamic models (148, 149). Such high flux can be attributed to the atomically smooth hydrophobic walls of the CNTs resulting in a slip of water through the pores. The nanotube membranes fabricated by Holt et al. were 3 mm long and had a diameter of 1.6 nm. Further measurements with these membranes revealed (150) salt rejection coefficients that matched or exceeded those of commercially available NF membranes as well as surpassed their flux by up to four times. Nevertheless, such

membranes are difficult and costly to manufacture and are prone to fouling given their hydrophobic nature. Besides CNTs, fullerenes can also serve as sorbents for PAHs such as napthlalene (151).

C. *Zeolites and other sorbents* – These are microporous aluminosilicate minerals commonly used as adsorbents due to the presence of a porous structure which loosely holds several cations. Although they can be naturally found, due to associated impurities synthetic zeolites such as NaP1 ($Na_6Al_6Si_{10}O_{32}.12H_2O$) are widely used for the exchange of cations such as Na^+ for heavy metals such as Ni(II), Cr(III), Zn(II), Cu(II), and Cd(II) (152). The principle mechanism of sieving is based on size exclusion. Once they capture the ions of interest, they can be hot pressed into extremely compact ceramic forms and safely discarded. A relatively novel adsorbent called self-assembled monolayers on mesoporous supports (SAMMS) shows promise in effectively adsorbing toxic metal ions, anions, as well as radionuclides (153, 154). The large surface areas (~1000 m^2/g) and high density of sorption sites on SAMMS surfaces with the capability of being functionalized to render them selective toward target pollutants makes SAMMS particularly attractive for water treatment.

1.4.2. Nanomaterials for water filtration

Membrane processes such as RO, UF and NF are considered key components of advanced water purification and desalination technologies and nanomaterials such as those predescribed are contributing to the development of more efficient and cost-effective water filtration processes. Two types of nanotechnology enhanced membranes exist – nanostructured membranes like those made of CNTs or nanocapillary arrays, effective in

removing bacteria (155); and nanoreactive membranes, where functionalized NPs aid the filtration process, such as the bimetallic Fe^0/Pt^0 NPs incorporated into cellulose acetate films fabricated by Meyer et al. (156) which showed an effective reduction of TCE with only ethane as a by-product. By surface modifying membranes with AgNPs, biofouling effects could be minimized (157). However, little is known on the stability of these functional layers and their environmental impact when they leave the membrane surface.

It can be seen from the above discussions that intensive chemical treatments such as those involving chlorine compounds, ozone, alum and ferric salts, coagulation and filtration aids, anti-scalants, and ion exchange resins often leave behind harmful byproducts, thus adding to the problems of contamination. Moreover, such treatment methods in many regions of the world cannot be used because of high cost and lack of appropriate infrastructure. The 1993 outbreak of cryptosporidiosis in Milwaukee, Wisconsin, U.S., in which approximately 400,000 people were infected and more than 100 died reminded the U.S. drinking-water industry that relying exclusively on physicochemical removal, which can suffer from malfunctions arising from defects in manufacturing or operation, can have a devastating effect on public health. A major hindrance to the efficient application of membrane bioreactors (MBRs) commonly used for treating biological contaminants is membrane fouling. Fouling in MBRs is primarily caused by microbe-generated extracellular polymeric substances, most notably polysaccharides, proteins and NOM. Hence, there is an urgent need to develop novel non-fouling membranes which are economical and of high flux. Fouling of polymer membranes is influenced by membrane physicochemistry and morphology. Polymers used in porous membranes are generally hydrophobic in nature, and as a consequence are highly vulnerable to adsorption of organic foulants. One of the

methods used to reduce fouling largely involve graft polymerization of hydrophilic monomers on the membrane surface (158). Such modified membranes, however, are only capable of preventing surface fouling, while internal pores may remain prone to fouling (159). The process of membrane modification also adds to membrane cost.

Another important issue to address is the detection limits of most of the above mentioned methods for water treatment. Contaminants occur in trace quantities and present a considerable challenge to remove them especially in presence of large concentrations of other constituents. It is not economically feasible to treat the entire volume of water either. Moreover, speciation remains a challenging detection problem. For example, As(III) is estimated to be ~50 times more toxic than As(V), so both As(III) and total As must be measured. The most common methods used today to detect As(III) are anodic stripping voltammetry (160) (LOD=1.2 μg/L) and ion exchange separations combined with inductively coupled plasma mass spectroscopy (161). But both methods are not feasible for domestic purposes, especially in developing countries. Determination of anions in aqueous systems remains one of the most challenging analytical problems. Typically, anions are determined by ion chromatography but lack the desired sensitivity.

Advances in macromolecular chemistry such as the synthesis of dendritic polymers have provided great opportunities for improving and developing effective filtration processes for water purification to eliminate different organic solutes and inorganic anions. Dendritic polymers which include hyperbranched and dendrigraft polymers, dendrons and dendrimers are highly synthetic, nanoscale branched structures with a high degree of surface functionalities, monodispersity, controlled composition, and architecture which display interesting physicochemical behavior due to their shape, size and multiple functionalities

(162). A dendritic polymer consists of three main components – core, interior branch cells, and a terminal branch cell. The size of a dendritic polymer is characterized by its 'generation', or number of branches emanating from the central core (Figure 1-15.). Moreover, the pH-dependant amphiphilic property of dendritic polymers allows them to capture various chemical species in diverse environments such as aqueous and organic solutions, and oil-water interfaces, and then release these chemical species in a controlled manner by changing the pH *in situ* without having to resort to intensive and expensive regeneration.

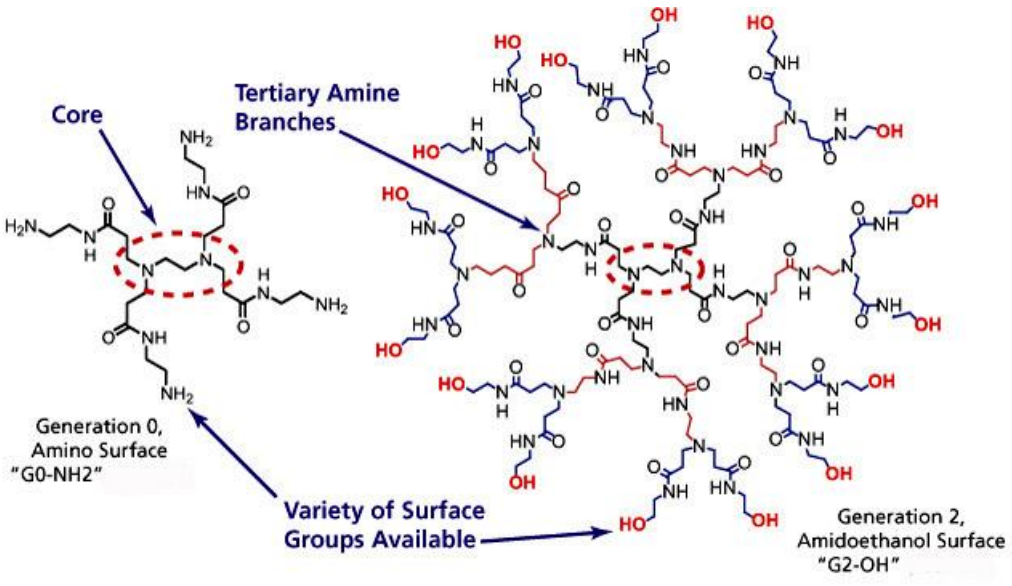

Figure 1-15. Exemplary structure of generation 0 (G0) and generation 2 (G2) polyamidoamine (PAMAM) dendrimers with amino and amidoethanol surface groups.

The unique physicochemical properties of dendrimers as noted below make them particularly attractive as functional materials for water treatment.

1. *Hosting capacity and Recyclability*: A high degree of flexibility in the synthesis of nearly monodisperse nanoscale (size ranges between 1-20 nm) dendrimers with well-defined molecular composition, size and shape, variable functionalization with cation/anion binding functional groups, and hydrophobic cavities in dendrimers afford them with flexible but rigid scaffolding. These properties provide new and unprecedented opportunities for developing a new generation of efficient and bio-benign functional materials for environmental remediation. Compared to the price of carbon-based nanomaterials (high purity MWNTs - $500/g, SWNTs - $2,000/g, and C_{60} - $120/g), dendrimers with a high degree of functionality (High purity Priostar™ Dendrimers - $50/g) serve as a more cost effective material for water purification (Dendritic Nanotechnologies, INC, Buckyball pricing from BuckyUSA, SW & MWCNT pricing from BuckyUSA, CNI, and Carbon Solutions, Dendrimers pricing from Dendritech & DNT). As reviewed above the pressure-driven RO membranes have a pore size of 0.1-1.0 nm and are very effective in retaining dissolved inorganic and organic solutes with molar mass below 1000 Da, but they suffer from membrane fouling, chemical damage, significant dead volume (20-40%), and high cost, and requires advanced operational skills. NF membranes are very effective at removing hardness and organic solutes with molar mass between 1000 – 3000 Da. In contrast, dendrimers with a molecular weight over 10,000 Da can effectively remove higher molecular weight inorganic and organic compounds. Unlike RO and NF membranes whose operations require high pressure, dendrimer-enhanced UF membranes require lower pressure (200–700 kPa) and can capture both low and high molecular weight contaminants, as opposed to UF membranes which can only remove dissolved

organic and inorganic compounds of >3 kDa. Dendrimers have much smaller intrinsic viscosities than linear polymers with the same molar mass because of their globular shape (162). Thus, comparatively smaller operating pressure and energy consumption could be achieved with dendritic polymers in tangential/cross-flow UF systems typically used for water purification. Per mass basis, dendritic polymers have a much large surface area than bulk particles. Moreover, it has been demonstrated that dendritic polymers can be integrated into existing, commercial UF membrane separation processes (163, 164). Dendritic polymers may be regarded as 'soft' NPs, have high hosting capacity, can serve as recyclable and water-soluble ligands for toxic metal ions, radionuclides, inorganic anions, organic solutes and PAHs (165, 166).

Specifically, within the pH range of 2-10, PAMAM dendrimers bind to transition metals and anions through multiple mechanisms, including Lewis acid-base complexation with their primary and tertiary amines serving as donors, and ion-pairing with charged terminal groups, and to PAHs through non-specific hydrophobic interactions that result from their physical encapsulation in interior cavities. Furthermore, dendritic polymers can be used as templates for the formation of catalytically active and redox NPs (167), and as bioactive NPs by scaffolding Ag(I) (168). In a proof-of-concept study, Diallo et al. (169, 170)showed that PAMAM dendrimers with an ethylenediamine core and terminal NH_2 could recover Cu(II) from aqueous solution with a much larger binding capacity than linear polymers with amine groups, and furthermore, the dendrimers could be regenerated and Cu(II) recovered by lowering the solution pH from 7 to 4. PAMAM dendrimers also show

a very low fouling tendency for commercially available regenerated cellulose membranes (170) and can be readily integrated into commercially available water purification systems (Figure 1-16).

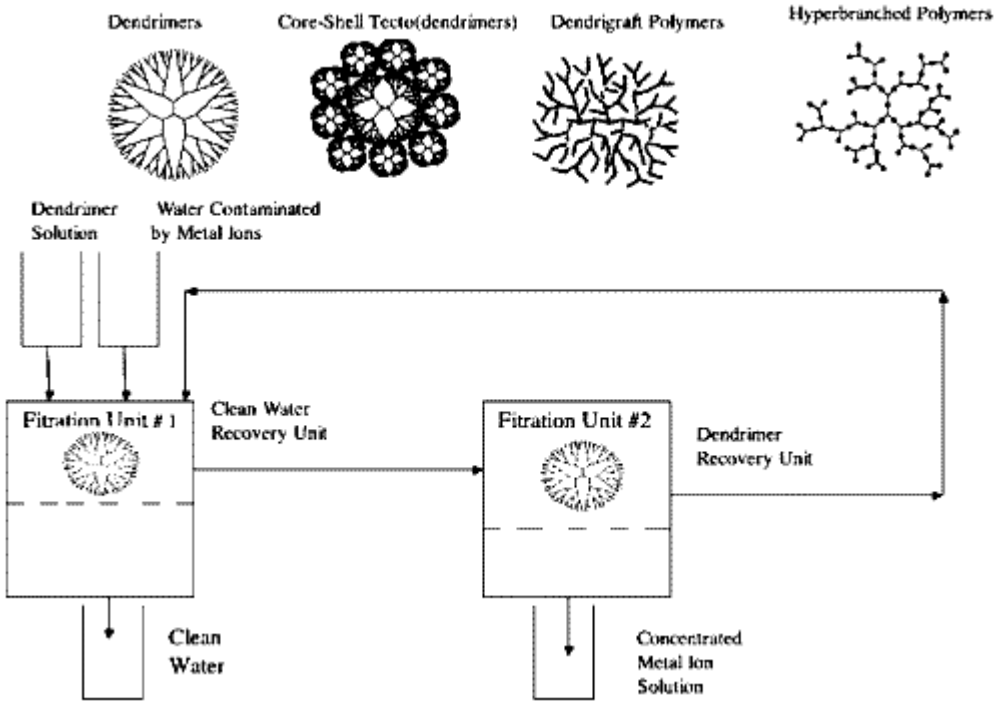

Figure 1-16. Recovery of metal ions from aqueous solutions by dendrimer enhanced filtration (170).

2. *Biocompatibility*: With the advancement of dendritic nanotechnology for environmental remediation, it is important to evaluate the environmental fate and toxicity of dendritic polymers. To that effect, dendrimer-related toxicity has been observed only for generation-seven and larger, and even then, only minimally (171).

Several studies on the use of dendrimers for DNA transfection, metal ion contrast agent carriers for MRI, targeted drug and therapeutic agent delivery vehicles, and viral inhibitors suggested that hyperbranched polymers and PAMAM dendrimers of generations-5 and below are non-toxic and biodegradable (172, 173). Moreover, dendrimers do not leave behind any potentially harmful by-products.

3. *Degradability*: PAMAM dendrimers show measurable degradation only in the third year of storage at 5°C, and a shelf life of ~6-9 months at ambient temperature based on retro-Michael reaction. Such long lifetime of dendritic polymers ensures their stability and effectiveness for the practice of water treatment. Dendrimers with aromatic structures within the polymer interior can be degraded by photon-induced cleavage. Furthermore, addition of enzyme-degradable bonds (e.g., amides in PAMAM) can be used such that intracellular or extracellular hydrolytic enzymes can break the polymer chains within one; such property could become relevant upon accidental uptake of dendritic polymers during water consumption. A third mechanism for dendrimer degradation is by water hydrolysis acting on ester bonds incorporated into the polymers. Such mechanisms may be utilized to selectively break down dendritic polymers post their usage in water treatment.

Thus, the high and versatile hosting capacities, energy efficiency, regenerability, selectivity, biocompatibility, and environmentally benign nature make dendritic polymers a desirable nanomaterial for environmental applications. It is therefore an effort through the second half of this dissertation to exploit the physico-chemical behavior of dendritic polymers for environmental remediation.

PART I

ENVIRONMENTAL IMPLICATIONS OF NANOMATERIALS

CHAPTER TWO

ENVIRONMENTAL IMPLICATIONS OF NANOMATERIALS

Chapter two focuses on understanding the interactions of quantum dots (QDs) and plastic nanoparticles with algal cells. QDs, specifically, owing to their unique electrical and optical properties, have found their applications in a number of areas ranging from medical imaging to tagging and sensing. Cadmium-based chalcogenides (CdE, where E = sulfide, selenide, telluride) were the first synthesized QDs and are widely used due to their ability to demonstrate an increase in their band gap energy with a decrease in their size (174, 175). Further, QDs can be synthesized as composite core/shell structures with a material of a larger band gap as the shell to enhance the photoluminescence quantum yields and shield the toxic core. Such core/shell QDs have been widely used in biological applications (176) and therefore have been selected for the presented study. A logarithmic QDs adsorption onto algal cells (*Chlamydomonas sp.*) was observed with increased QDs concentration. In addition, both our CO_2 depletion and O_2 production assays showed a significantly inhibited photosynthetic activity of the algae exposed to the QDs, suggesting the potential impact of nanoparticle adsorption on the photochemistry of aquatic plant species (177).

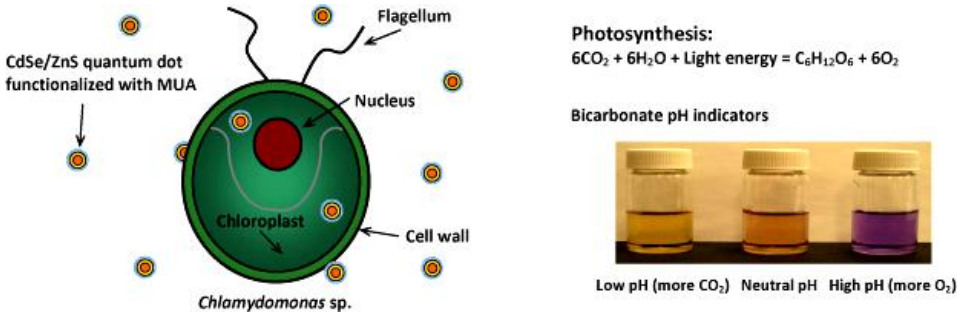

Scheme 2-1: Schematic of the adsorption of QDs on algal cells and their effects on the algal photosynthesis (177).

In our study the impact of inorganic NP adsorption onto algal cells was extended to that of organic NPs. The physical adsorption of nanosized PS beads onto a model cellulose film and two living algal species, *Chlorella* and *Scenedesmus*, was studied. This adsorption was found to ubiquitously favor positively charged over negatively charged plastic beads due to the electrostatic attraction between the beads and the cellulose constituent of the model and living systems. Such a charge preference is especially pronounced for *Chlorella* and *Scenedesmus*, whose binding with the plastic beads also depended upon algal morphology and motility, as characterized by the Freundlich coefficients. Furthermore, a CO_2 depletion assay showed that adsorption of PS beads hindered algal photosynthesis, possibly through the physical blockage of light and air flow by the NPs. Our ROS assay further indicated that PS adsorption promoted algal ROS production (177). Such algal responses to PS exposure may have implications on the sustainability of the aquatic food chain.

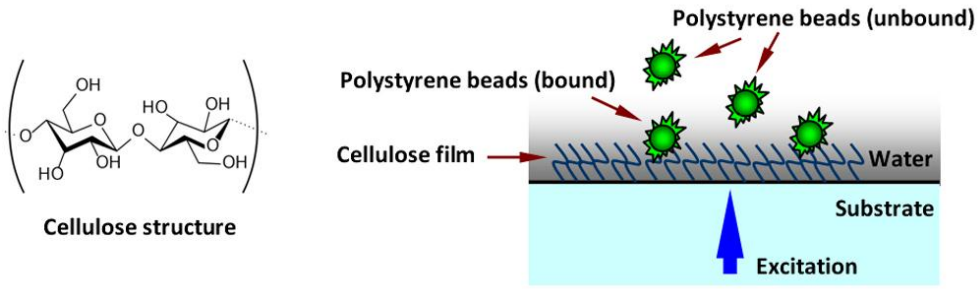

Scheme 2-2: Schematic of the adsorption of PS beads on a cellulose substrate (178).

2.1. Introduction

Along with the rapid development of nanotechnology, a major technological advancement of the present time, there is a growing interest and a need to understand the biological and environmental consequences of engineered nanomaterials (179, 180). Obtaining such an understanding will benefit the biological, medicinal, and environmental applications of nanotechnology. Additionally, research in this area will guide the design and production of nanomaterials to minimize their potential adverse effects on human health and the environment (181). QDs are a major class of semiconducting nanocrystals which possess unique optical, electrical, and chemical properties (182-184). Since their early development in the 1980s, QDs have been used extensively in such biological applications as cell labeling, fluorescence in situ hybridization, pathogen detection, ligand binding, genomic and proteomic detection, and high-throughput screening of biomolecules (182-188). The toxicity of QDs has also been examined, and strategies though far from optimal have been developed to improve the biocompatibility of QDs through ligand exchange, hydrophobic interaction, and encapsulation (184). Like other classes of ENPs, QDs may eventually be

discharged through industrial and research outlets and impact living organisms in the environment. Despite their broad use in many applications, fundamental research on the biological and environmental fates of ENPs is critically lacking (17, 189). Specifically, little is known about the interaction between ENPs and plant species (17, 189-192), the major component of ecosystems and the food chain. Among the literature available, mixtures of nano-SiO_2 and nano-TiO_2 were reported to increase nitrate reductase activity, enhance water and nutrient uptake, stimulate the antioxidant system, and hasten germination and growth of soybean (*Glycine max*) (193). Nano-TiO_2 at 0.25% increased seed germination, plant dry weight, chlorophyll production, and the RuBP activity and the rate of photosynthesis of spinach (*Spinacia oleracea*), while concentrations greater than 0.4% nano-TiO_2 were found to be detrimental to plant growth (194). Chlorophyll-bound gold and silver nanoparticles were found to enhance the production of excited electrons in the photosynthetic complex (195). Uncoated alumina nanoparticles at 2000 mg/L were reported to reduce the root growth of corn, carrot, cucumber, soybean, and cabbage seedlings, while alumina nanoparticles coated with phenanthrene had no effect on the root growth of vegetation (196). One recent study (197) demonstrated the uptake of fullerene C_{70} by rice plants. These fullerene particles were found to share the vascular systems with water and nutrients and were transmitted to the second generation of the rice plants through plant progeny harvested from the first generation.

Here, single-celled green algae *Chlamydomonas* sp. were used as a model system for examining the interaction of QDs with plant species. Like most high plants and bacteria, algae possess a cell wall outside their cell membrane. However, unlike mammalian cells, algae do not show robust endocytosis when exposed to foreign materials and particles. Previous

spectroscopic and electron microscopic results suggest that small QDs of less than 5 nm in diameter, when aided by light, can enter bacteria possibly by means of oxidative damage to the cell wall and the cell membrane (198). There are three possible mechanisms through which QDs could pass through the algal cell walls and membranes: (1) nonspecific diffusion - is unlikely with QDs since the largest globular proteins that can pass through intact cell walls of *Bacillus subtilis*, a bacteria, have radii of ~2 nm (199), while the smallest high-quality QDs measure ~3 to 4 nm (200); (2) non-specific membrane damage – highly reactive halogenated NPs were able to enter bacterial cells via nonspecific membrane damage (201). QDs can enter the cells through this mechanism as these NPs are able to transfer electrons to redox-active molecules (including oxygen) upon light exposure (202) and the smaller the QD, the greater its redox potential (203, 204); and (3) specific uptake – takes place through pore sizes slightly larger than those for nonspecific diffusion; the largest pores known are of permeases for excreting proteins from bacteria and have been shown to have pore openings of up to 6 nm. Since functionalized QDs are typically larger than 5 nm, our focus was on the effect of QDs *adsorption* on algal photosynthesis, and uptake of QDs into algal cells was disregarded.

For over a century, plastic has served our domestic and industrial needs, ranging from household utensils to cosmetics, sportswear, automobile parts, and oil and water pipelines. Plastic production, estimated at 260 million tons globally in 2007 (205), comes in various forms of natural materials (e.g., chewing gum, shellac), chemically modified natural materials (e.g., natural rubber, nitrocellulose), and completely synthetic materials (e.g., epoxy, polystyrene). Due to its mass production, plastic rapidly accumulates in terrestrial and aquatic habitats and has become the most common type of marine litter worldwide (75, 89).

Surveys of New Zealand beaches have revealed 100,000 plastic granules per meter of coastal zone (206). Experimentally cleared beaches in Panama were seen to regain 50% of the original plastic burden after only 3 months (207). Beaches in remote South Pacific Islands were collecting plastic debris and microplastic particles at levels comparable to industrialized areas (208). The sources of plastic contamination of the marine environment include preproduction plastic pellets, powders, production scrap, consumer plastic debris, and microplastic particles used in industrial and domestic cleansers and in medical applications for drug delivery (94, 100, 209, 210). Plastic debris transported by wastewater and stormwater systems subsequently enters aquatic habitats where photo, chemical, and physical degradation processes fragment them into a wide array of particles sizes, ranging from macroscopic (>5 mm) to microscopic (<1 μm) (94). In contrast to the global scale of plastic disposal, it remains poorly understood as to what extent discharged plastic may compromise environmental sustainability (89, 211, 212). In this chapter, the physical adsorption of PS NPs on cellulose - a major structural component of the cell wall of green plants, many forms of algae, and the oomycetes - was examined. PS is a thermoplastic material made from petroleum-derived styrene. It is widely used to make both rigid and foam products. Foam PS or Extended PS (EPS) is used extensively in cups, plates, trays and packaging and degrades faster than most other forms of plastics (213).

Both single-celled *Chlorella* and multicelled *Scenedesmus* were used to delineate the effect of algal morphology on plastic adsorption. To further assess algal photosynthetic activities, the rate of CO_2 depletion resulting from the plastic adsorption was measured. In order to evaluate algal responses to environmental stresses caused by the plastics, ROS production by the algal species was also monitored. The use of plastic NPs is a first in the

field and is a logical extrapolation of microplastics continuously weathered by sunlight, rain, wind, and ocean waves, as well as decomposed by bacteria, microorganisms, and NOM (89). Furthermore, photo-oxidation functionalizes the surface of plastics to render them with different charge polarities, a basis for employing both positively and negatively charged plastics here.

2.2. Nanomaterials Characterization

Yellow fluorescent CdSe/ZnS core/shell QDs (Ex: <550 nm; Em: 570-585 nm) were purchased from NN-Laboratories, LLC. The QDs were rendered water soluble by mercaptoundecanoic acid (MUA) ligands coating on the QD surfaces. Positively (amidine latex) and negatively (carboxyl latex) charged PS beads were purchased from Molecular Probes. The primary size and surface area of both types of beads were 20 nm and 2.5×10^6 cm^2/g, respectively. The amidine NPs were stable at low pH and hence were dispersed in MES buffer with a pH of 6 at room temperature. The carboxyl NPs were stable at neutral to high pH and were dispersed with Milli-Q water with a pH of 7.4 at room temperature. The PS NPs existed as small agglomerates in both dispersions, and a complete breakdown by sonication was not performed, since this would not replicate a realistic representation of the natural conditions.

2.2.1. Nanomaterial size and surface charge

Nanomaterial size is characterized either by light scattering techniques or by scanning electron microscopy (SEM) and TEM. Dynamic light scattering (DLS), also known as photon correlation spectroscopy, is a technique most commonly used to measure the

hydrodynamic size of nanoparticles. When a monochromatic light beam, such as a laser, shines onto a solution with spherical particles in Brownian motion, a Doppler Shift occurs when the light hits the moving particle, changing the wavelength of the incoming light. This change is related to the size of the particle. It is possible to compute the sphere size distribution and give a description of the particle's motion in the medium by measuring the diffusion coefficient of the particle and using the autocorrelation function. The nondestructive *in situ* nature of scattering experiments has significant advantages over the electron scattering techniques. Dynamic scattering measures the instantaneous values of the scattered intensity $I(t)$ over time at a fixed angle, φ. For concentrated and/or interacting NPs, the diffusion coefficient is modified due to the hydrodynamic and thermodynamic (attraction and repulsion) interactions between the neighboring NPs. The motion of the nanoparticles is then strongly coupled. Therefore, DLS is not suited for concentrated samples or complex mixtures where the particles are likely to be interacting with one another. Viscometry can be employed for measuring the hydrodynamic size of soft polymeric nanoparticles and will be discussed in Chapter Three.

The average hydrodynamic diameter of the QDs determined by DLS (Zetasizer S90) was 11.69 nm. A small volume of QDs suspension (10 μL) was air-dried directly on a 200 mesh formvar/carbon-coated copper TEM grid prior to imaging. The concentration of the QDs was 0.1 mg/mL. Imaging was conducted with a Hitachi H-9500 high resolution transmission electron microscope, under a 100 kV accelerating voltage. The dried QDs were determined by TEM as 5-9 nm.

NP surface charge can be modified, intentionally or unintentionally through chemical functionalization (to increase stability in aqueous media) or adsorption of species onto

particle surface. Surface charge is a key parameter controlling NP stability in aqueous media. It can vary as a function of pH due to protonation or deprotonation of functional groups, while fixed charges result from crystal lattice defects and atomic substitution. In an aqueous medium, a diffuse electrical double layer will form at the solid-liquid interface as ionic species are attracted to the charged surface. The zeta (ζ) potential is the electrical potential that exists at the "shear plane" at some distance from the particle surface (Figure 2-1). It is derived from measuring the electrophoretic mobility distribution of a dispersion of charged particles as they are subjected to an electric field.

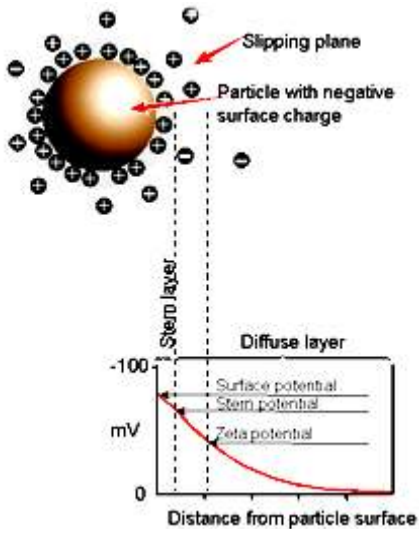

Figure 2-1. Schematic representation of zeta potential (Image courtesy of Zeta Potential – An Introduction in 30 min, Malvern Instruments Technical Note).

The surface charge of the as-supplied PS beads was characterized using a Zetasizer. The amidine PS beads showed an average zeta potential of 106 mV, and the carboxyl PS beads had an average zeta potential of -40.4 mV. Both zeta potential measurements were performed for the PS beads of 4 mg/mL and their values indicate good stability in aqueous solutions.

2.3. Algal Cell Characterization

Fresh *Chlamydomonas* sp., oval shaped single-celled green algae (Figure 2-2), were harvested from the greenhouse at a Clemson University Facility. These algae are commonly found in soil and freshwater. The cell wall of *Chlamydomonas* sp. is a seven-layered structure with three conspicuous layers composed mainly of non-cellulosic polysaccharides and glycoproteins (214). The algae have a prominent cup or bowl-shaped chloroplast which contains the pyrenoid – the center for CO_2 fixation. The whole cell wall is approximately 320 nm wide (215). The algae use flagella for their motility.

Freshwater algae *Chlorella* and freshwater/saltwater *Scenedesmus* were purchased from Carolina Biological Supply Company. They were cultured in Alga-Gro freshwater medium. In contrast to *Chlamydomonas* sp., *Chlorella*, single-celled green algae, are spherical in shape and about 2-10 μm in diameter (Figure 2-2(a)) and do not possess flagella. *Chlorella* contain green photosynthetic pigments, chlorophyll-*a* and chlorophyll-*b* in their chloroplasts. Due to their high photosynthetic efficiency of ~8% (216) and richness in proteins, *Chlorella* are a good source of food and energy. Among all plants in the world, green algae are the highest sources of chlorophyll, and *Chlorella* accounts for the highest among them ranging from 3-5% chlorophyll (217). Unlike *Chlamydomonas* sp., the *Chlorella* cell walls do contain cellulose.

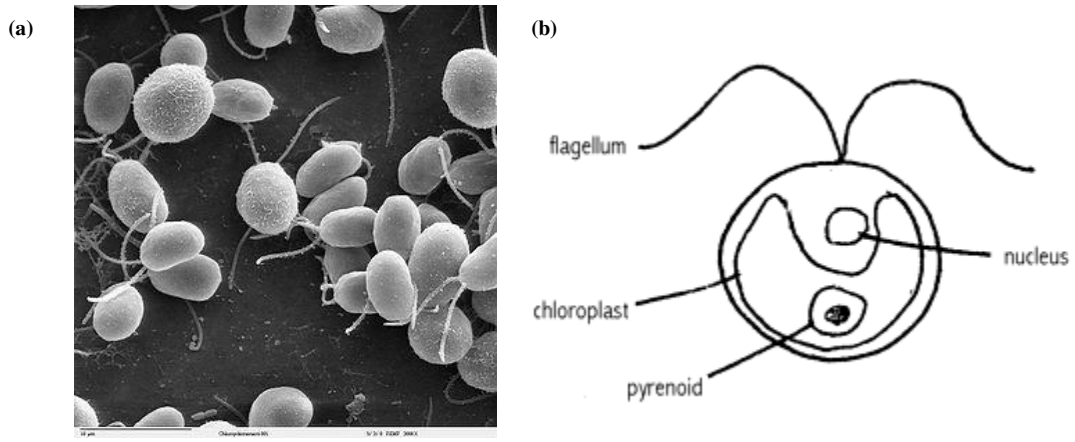

Figure 2-2. (a) SEM image of *Chlamydomonas reinhardtii* sp. (218) (b) Schematic drawing of a *Chlamydomonas* cell (Image courtesy of www.wikipedia.org).

Scenedesmus belong to a genus of freshwater single-celled or colonial algae forming 2-32 celled, usually 4-celled colonies. They are elongated and ellipsoidal in shape with an average area of 7×16 μm^2 and possess two pairs of flagella (Figure 2-2(b)). The cell wall of *Scenedesmus* consists of sporopollenin in the outer layer and hemicellulose in the inner layer and is usually smooth. Sporopollenin is an isoprene derivative. It is a component of pollen cell walls. In contrast to cellulose, hemicellulose is derived from several sugars in addition to glucose including xylose, mannose, galactose, rhamnose, and arabinose. Hemicellulose also consists of shorter chains of approximately 200 sugar units and is branched as opposed to unbranched cellulose. Each *Scenedesmus* contains a chloroplast with a single pyrenoid.

2.4. Interactions of QDs with Algae

Algal cells were concentrated by low-speed centrifugation (11,700 RCF) for 3 min. The concentrated algae were then incubated with QDs of 0.05-5 ppm at room temperature

for 2 h. Four samples of each concentration were prepared to ensure experimental repeatability and to establish error bars.

2.4.1. Qualitative visualization of interactions

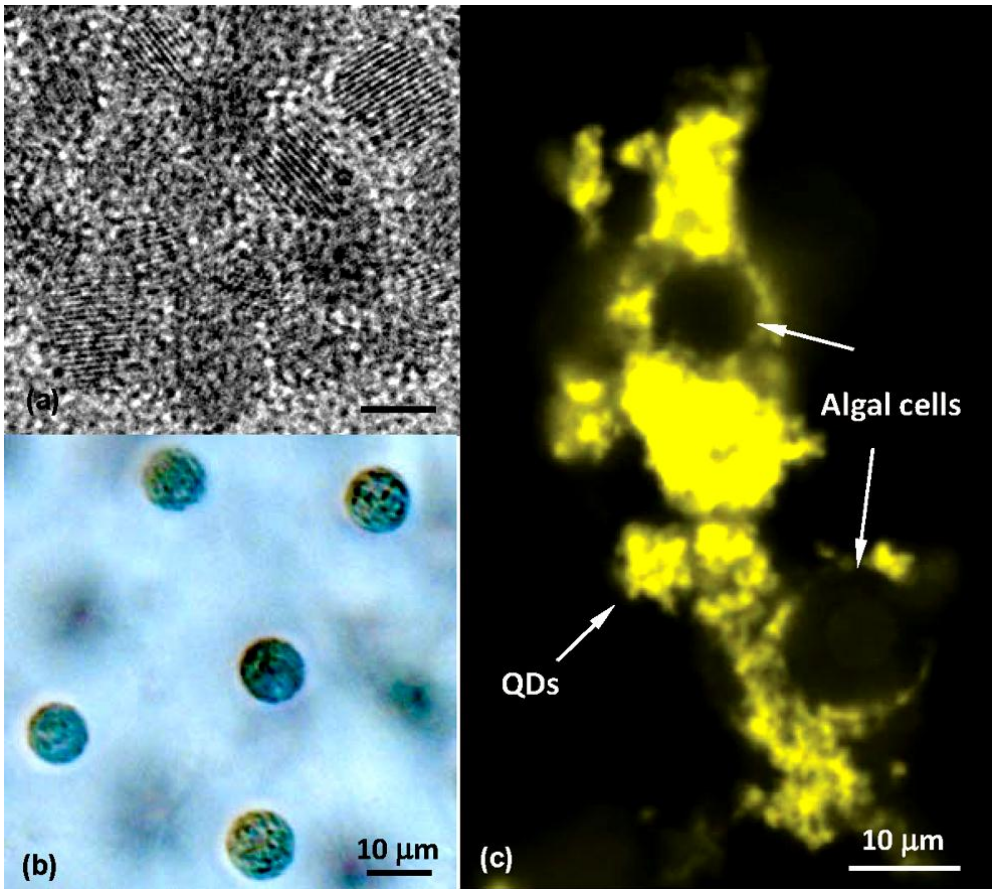

Figure 2-3. (a) Transmission electron microscopy image of CdSe/ZnS QDs, whose sizes are in the range of 5-9 nm. The QDs lattices are visible. Scale bar: 5 nm. (b) Bright field image of algal cells. (c) Confocal fluorescence image of QDs (yellow) adsorbed on algal cell (round) surfaces (177).

The algal cells were imaged under bright field microscopy with a fluorescence microscope (Imager A1, Zeiss). Approximately 10 μL of algae solution was flown into a sample channel sandwiched between a glass substrate and a cover glass prior to imaging. Figure 2-3(b) shows the image of the algal cells. The non-fluorescent thin flagella are not visible in the image. To observe the effects of QD adsorption onto the algal cells, the algal cells were incubated with QDs in an 8-well chamber glass overnight and visualized using confocal fluorescence imaging (LSM 510, Zeiss). Samples were excited with an argon ion laser at 488 nm and fluorescence images were captured with use of a BP 570-590 filter set and a 40× oil immersion objective. Figure 2-3(c) shows the confocal image of the adsorbed QDs onto the algal cells. The algal cells had negligible fluorescence at 488 nm. The image clearly shows significant QD adsorption onto the algal cells. A small volume of QDs suspension was also imaged using TEM. A drop (10 μL) of the QD aqueous solution was air-dried directly onto a 200 mesh formvar/carbon-coated copper TEM grid prior to imaging. The concentration of the QDs was 0.1 mg/mL. Imaging was conducted with a Hitachi H-9500 high resolution transmission electron microscope, under a 100 kV accelerating voltage. The QD crystalline structure was clearly visible (Figure 2-3(a)).

2.4.2. Quantitative assessment of QD-algae interactions

A UV-vis spectrophotometer (Biomate 3) was used to quantify the amount of QDs adsorbed on the algae. Absorbance was recorded at 545 nm before and after adding various concentrations of QDs into the algal growth medium, with the differences denoting total concentrations of the QDs in the solution. At this wavelength QDs showed a strong

absorbance. After 2 h of incubation, 10 μL of NaOH was added in the algae/QDs solution before filtering through membranes with a pore size of 0.45 μm (Nalgene). The introduction of NaOH was to prevent the aggregation of negatively charged QDs (due to the deprotonation of the carboxylic acid of MUA, Figure 2-4(b)) in the weakly acidic environment of the algal growth medium (pH 6.45). After filtration, all algal cells were blocked by the membranes because of their large size (~10 μm, Figure 2-4(b)), while the absorbance of the filtrate indicated the amount of free (or unadsorbed) QDs. The amount of adsorbed QDs can be calculated by Equation 2-1:

$$Abs_{adsorbed} = (Abs_{QDs+algae} - Abs_{algae}) - Abs_{filtered} \quad (2\text{-}1)$$

where $Abs_{filtered}$ and $Abs_{QDs+algae}$ denote the absorbance of the algae/QDs solution before and after filtration, and Abs_{algae} is the absorbance of the algae alone. An adsorption curve was established by varying the QDs concentration from 0.1 to 5 ppm (Figure 2-4(a)).

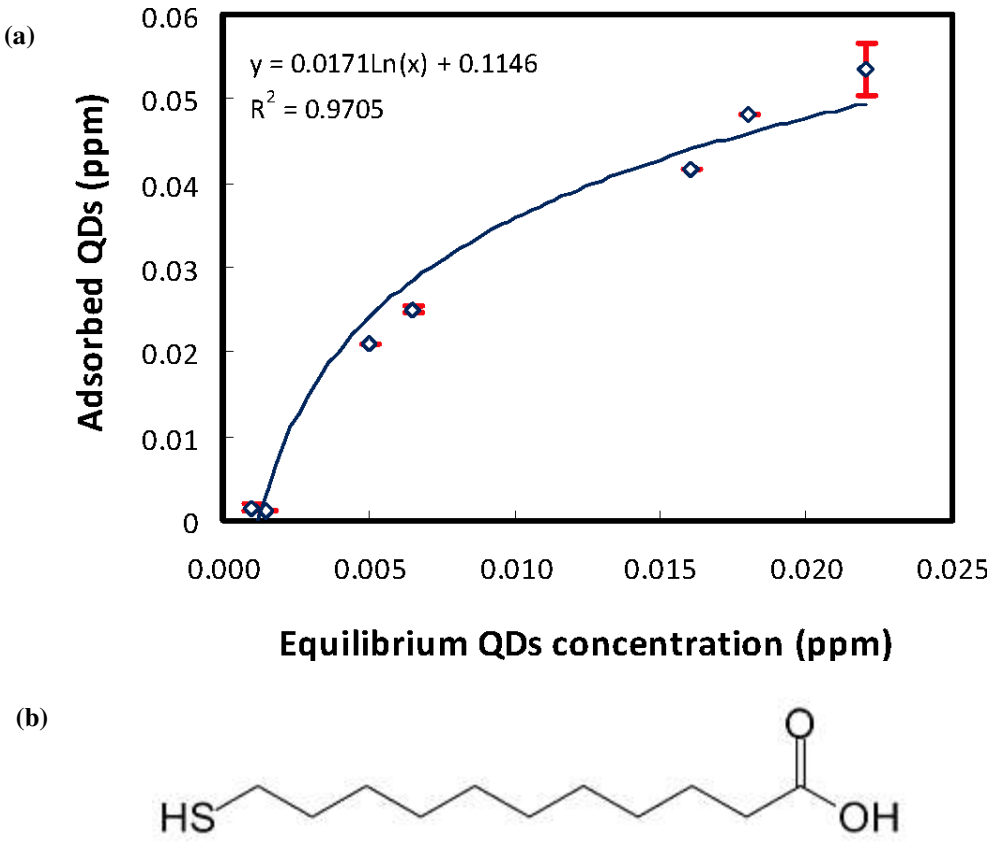

Figure 2-4. (a) Adsorbed vs. equilibrium QDs concentration. The equilibrium QDs concentration is the adsorbed QDs subtracted from the initial QDs sample concentration. Also shown is a fitted logarithmic trendline (177) (b) Schematic of MUA ligand.

This curve was derived from Equation 2-1 as described above. Adsorption of QDs to algal cells increased with the dosage of the QDs. A logarithmic increase in the QD amount adsorbed was observed with increased equilibrium concentration of the QDs. The surface area of a typical algal cell (~10 μm in diameter) is at least 250,000 times larger than that of a QD (<20 nm in diameter), which allowed for a significant amount of the QDs to be adsorbed. The QDs used in this study were surface-coated with MUA, a ligand to elicit water solubility. When examined under bright field imaging, the algae exposed to the QDs

appeared less mobile than the control algae. As stated above, the pore size of the *Chlamydomonas* cell wall is approximately 320 nm wide. The chemical composition of the porous algae cell wall consists of polysaccharides and glycoproteins, which afforded numerous QDs binding sites through nonspecific (electrostatic, hydrophobic, and hydrogen bonding) interactions. The binding affinity of QDs for algae can also be due to the H-bonding interaction between the carboxylic groups (-COOH) of the MUA and the amine groups ($-NH_2$) of the algal cell wall. The overall interaction between algae and QDs can physically and/or chemically damage the algal cell wall and membrane to facilitate uptake of the QDs. However, no such uptake was observed in our electron microscopy imaging, possibly due to the size of the QDs, the aggregation of the QDs in the weakly acidic algal growth medium, as well as the thickness of the algal cell wall (~20 nm) (219). To better understand the physical adsorption of QDs to algae, the Freundlich model (220) was used to fit the adsorption isotherms. The Freundlich model is a modification of the Langmuir adsorption scheme, and is appropriate for describing rough inhomogeneous adsorbent (i.e., algae) surfaces with multiple adsorption sites. Considering the adsorbate-adsorbate (i.e., QDs-QDs) interactions, the empirical Freundlich equation is expressed in Equation 2-2 (221)

$$q_{eq} = kC_{eq}^{\ n} \qquad (2\text{-}2)$$

where k is a coefficient indicating the affinity of QDs for algae, n is a constant characteristic of the adsorption system and is related to the binding efficiency. An n value of less than 1 indicates a favorable adsorption, while an n value higher than 1 reflects a weak adsorption (221). The parameters C_{eq} and q_{eq} represent the concentrations of nonadsorbed QDs and the

QDs adsorbed on the algae at equilibrium, respectively. According to the Beer-Lambert law, absorbance is proportional to the concentration of the QDs. For a solution of an absorbing substance, the absorptivity ratio at a monochromatic wavelength is defined as{(incident light, Io)/(transmitted light, I)} and this is logarithmically related to concentration and optical path-length by the Beer Lambert law: Absorbance (A) = $\log_{10}$(Io/I) = ε.c.l., where c is the concentration of solute, l is the path length through the sample, and ε is a constant known as the molar absorptivity or extinction coefficient for each species in the solution for a particular wavelength. Thus, for a fixed path length, UV-vis spectroscopy can be used to determine the concentration of the absorber in a solution.

As such, the parameters of the Freundlich equilibrium model were fitted from a log-log plot of C_{eq} vs. q_{eq}. The plot slope represents the exponent $1/n$, and the value of k can be read from the intercept. For our absorbance data, the value of k was determined as 0.588 ppm^{1-n}, with its exponent n fitted at 0.629. This n value suggests a favorable binding of the QDs to the algae (177).

2.4.3. Effects of QD adsorption on algal photosynthesis

Photosynthesis is a source for driving the metabolic processes of nearly all living species. It is the primary means of fixing CO_2 into organic matter and fuels food production on land and in sea. Algae are positioned at the bottom of the food chain, and algal photosynthesis is a major source of much of earth's oxygen. Since algae consume CO_2 that is dissolved in the aquatic environment, the rate of CO_2 depletion serves as a key indicator for evaluating the photosynthetic activity of the organism. The standard photosynthetic reaction is described by Equation 2-3:

$$6CO_2 + 12H_2O + \text{photons} \rightarrow C_6H_{12}O_6 + 6O_2 + 6H_2O \qquad (2\text{-}3)$$

To evaluate the effects of QDs absorption on algal bioactivities, both oxygen production and carbon dioxide depletion of the algae were examined. A bicarbonate indicator solution (0.2 g of thymol blue, 0.1 g of cresol red, in 0.01 M $NaHCO_3$) was prepared to monitor the depletion of CO_2, the activities of which are depicted by Equation 2-4:

$$HCO_3^- + H^+ \Leftrightarrow H_2O + CO_2 \qquad (2\text{-}4)$$

The algae/QDs solution was mixed with the indicator solution and the samples were tightly sealed to prevent gas exchange. During photosynthesis, the algae consumed CO_2 over time, causing the pH value of the indicator solution to increase accordingly. A transition from acidic to basic condition was indicated by a color change from yellow to purple, accompanied by an increase of absorbance at 574 nm (Scheme 2-1, right panel). The depletion rates of CO_2 were then calculated based on the increase of absorbance values for different sample concentrations. To measure oxygen production of the algae in the presence of the QDs, an Oxyg32 system (Hansatech Instruments) was used for a fixed amount of algal cells treated with various dosages of QDs. All measurements were made at room temperature, under identical lighting conditions. Algae consume CO_2 that is dissolved in aqueous solution for photosynthesis; they also produce O_2 as an end product. Thus, the rate of CO_2 depletion is an important parameter for indicating the photosynthetic activity of the algae. According to Equation 2-4, an increase in the pH corresponds to a decrease in the concentration of CO_2 in the bicarbonate indicator solution. As shown in Figure 2-5(a), the absorbance of the bicarbonate indicator at 574 nm increases with its pH. Therefore, the rate of the increasing absorbance can be treated as an indicator of the CO_2 depletion rate. As

shown in Figure 2-5(b), an increased dosage of QDs resulted in a significant decrease of CO_2 depletion rate at and above 100 ppm of QD dosage.

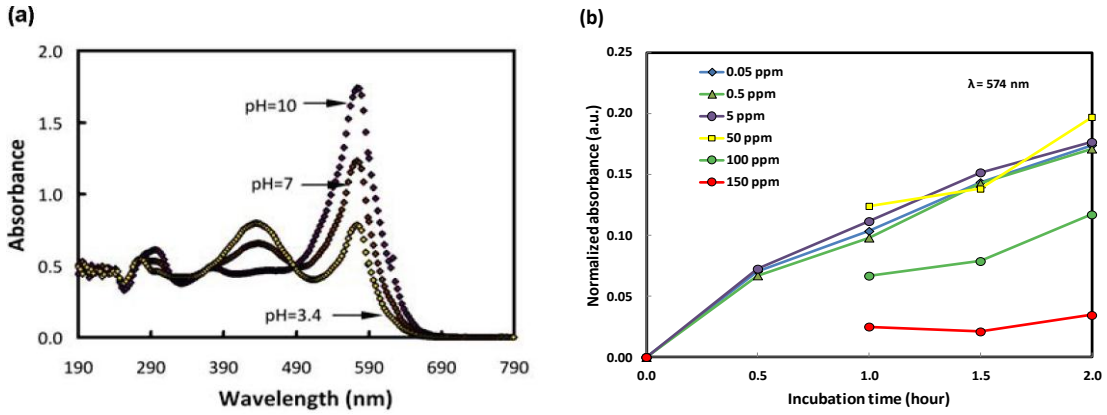

Figure 2-5. Absorbance of bicarbonate indicator for acid, neutral, and basic solutions. The absorbance peaks occur at 574 nm, increasing with the pH values of the solutions. (b) Comparison of CO_2 depletion rates for QDs of various dosages, measured at 574 nm. Significantly reduced CO_2 depletions were found at and above 100 ppm of QDs (177).

The O_2 production rate was also monitored as a result of QD adsorption on algal cells. As shown in Figure 2-6, the oxygen production rate was significantly affected by the addition of different QD concentrations to a fixed concentration of algal solution. Above 5 ppm of QD dosage, the O_2 production rate decreased to nearly zero, indicating a significantly reduced photosynthetic activity. Both experiments proved that the introduction of QDs to algal growth media affected their photosynthetic activity. CO_2 depletion was significantly reduced above 100 ppm of QDs dosage, while retarded O_2 production rate occurred in the low ppm range of QDs dosage. Previous studies with ENPs (ZnO, TiO_2, and CuO) (222-224) mainly focused on the growth inhibition of algae, perhaps due to the

light shading effect, but neglected the photosynthetic function of the algae. As a primary producer in the food chain, the photosynthetic activity of algae is equally important as its reproduction behavior. Introducing QDs to algal growth media triggered the interactions between the algae and the QDs, elicited by adsorption of the QDs onto the algal cells. Adsorption of QDs is expected to hinder the gas flow through algal cells needed for photosynthesis, block the pathways of nutrients uptake, and impede algal mobility via obstruction of their flagella movement. Furthermore, adsorption of QDs can damage algal cell walls to induce pore formation, which could facilitate translocation of the QDs. Although not evident in our study, QDs post uptake may also bind to pyrenoids serving as centers for CO_2 fixation in algal chloroplasts (Figure 2-2(b)), or generate ROS inside algal cells, both of which reduce algal bioactivity.

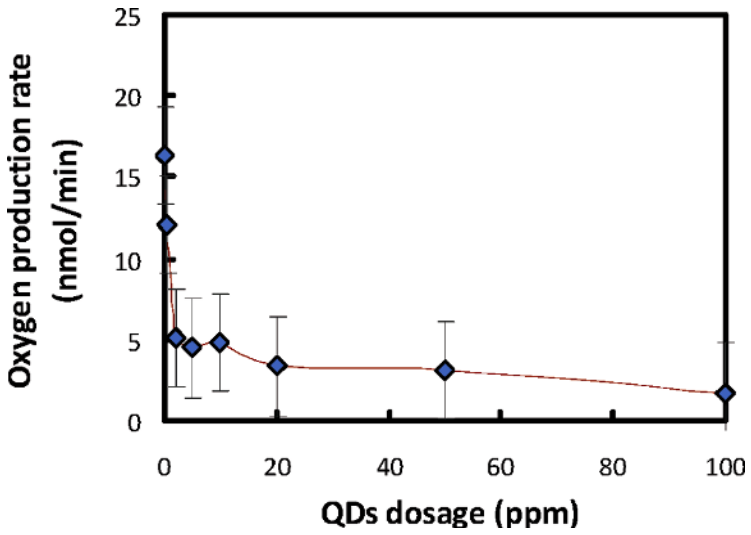

Figure 2-6. Oxygen evolution rate vs. dose of QDs. Significant reduction of oxygen production was observed due to the introduction of QDs to algae solution (177).

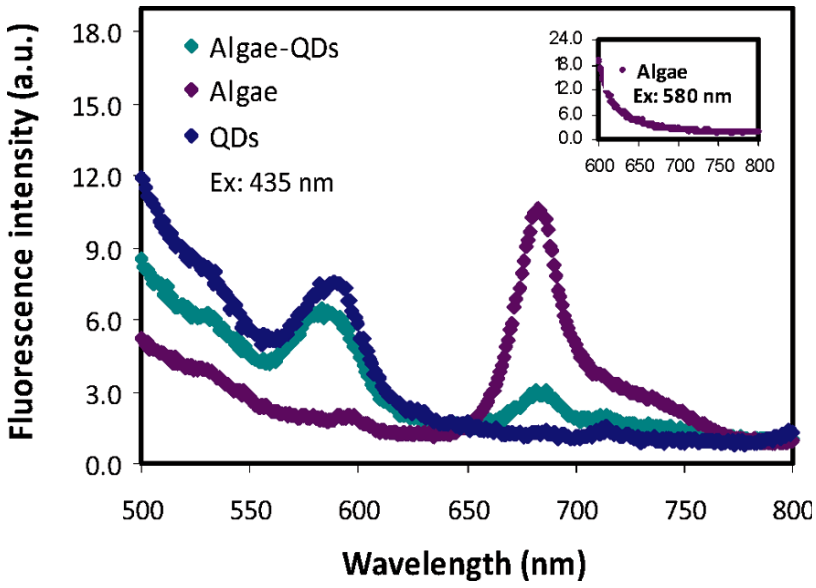

Figure 2-7. Fluorescence intensities of algae (purple), QDs (dark blue), and algae-QDs mixture (cyan), excited at 435 nm where the chlorophyll in algae absorbs light efficiently. The algae and the QDs show strong fluorescence peaks at 683 and 580 nm, respectively. In contrast, the mixture of algae-QDs displays a less prominent fluorescence peak than QDs at 580 nm, and a much less prominent peak than algae at 683 nm (cyan). The fluorescence emission of algae is negligible when excited at 580 nm (inset) (177).

The QD fluorescent properties could also affect algal photosynthesis by either enhancing or quenching the photocatalysis. Hence, a fluorescence spectrophotometer (Varian Cary Eclipse) was used to examine the effects of QDs fluorescence on the photo properties of algal cells. The excitation was set at 435 nm, a wavelength known to induce strong light absorption by the chlorophyll in algae (225, 226). Fluorescence spectra were recorded for algae, QDs (50 ppm), and algae/QDs solution (QDs: 50 ppm; incubation time: 2 h) within the wavelength range of 500-800 nm, at 1 nm/step. As shown in Figure 2-7, when excited by light at 435 nm, QDs emitted a strong fluorescence peak at 580 nm (blue) while algae emitted a prominent fluorescence peak at 683 nm (purple). The algae/QDs solution, in contrast, displayed two fluorescence peaks both at 580 and 683 nm (cyan).

Specifically, the fluorescence peak at 580 nm for the algae/QDs solution was reduced by 20% as compared to that for free QDs, while the peak at 683 nm for the algae/QDs solution was reduced remarkably by 73% as compared to that for the algae. The reduction of QDs fluorescence at 580 nm could be due to the inefficient light absorption by the QDs when adsorbed into multilayers on the algal cell surfaces, or the fluorescence resonance energy transfer (FRET) (227-229) from the QDs (donor) to the algae (acceptor). However, FRET could be excluded as a major cause for the reduced fluorescence intensities based on these following observations: (a) lack of anticorrelation between the QDs fluorescence peak at 580 nm and the algal fluorescence at 683 nm, as indicated by the cyan curve, and (b) lack of fluorescence emission (resonance) when algae were directly excited by light at 580 nm (Figure 2-7 inset). Since intracellular chloroplasts were separated from the extracellular QDs by far more than a Forster distance (227), FRET between the adsorbed QDs and the algae was deemed unfeasible. The subdued fluorescence peak at 683 nm for the algae/QDs solution (Figure 2-7) is attributed to light emission from free or less coated algae, which could be directly excited by light at 435 nm.

2.5. Interactions of PS with Cellulose

Cellulose is a linear polymer, a polysaccharide, consisting of several hundred to over ten thousand D-glucose units linked by β(1→4)-glycosidic bonds (Figure 2-8(a)). It is the most common organic compound on earth and forms a major component of the cells walls of plants, many forms of algae and bacteria. It is hydrophilic, yet insoluble in water. The hydroxyl groups on the glucose residues of one chain form hydrogen bonds with the oxygens on another chain thus firmly holding the chains together side-by-side. This structure

forms microfibrils with high tensile strength which confer rigidity to the plant cell wall (Figure 2-8 (b)). Considering the prevalence of cellulose in plants and bacteria, we expect the binding of cellulose with plastic NPs could shed light on our understanding of the uptake of the particles by plants and bacteria.

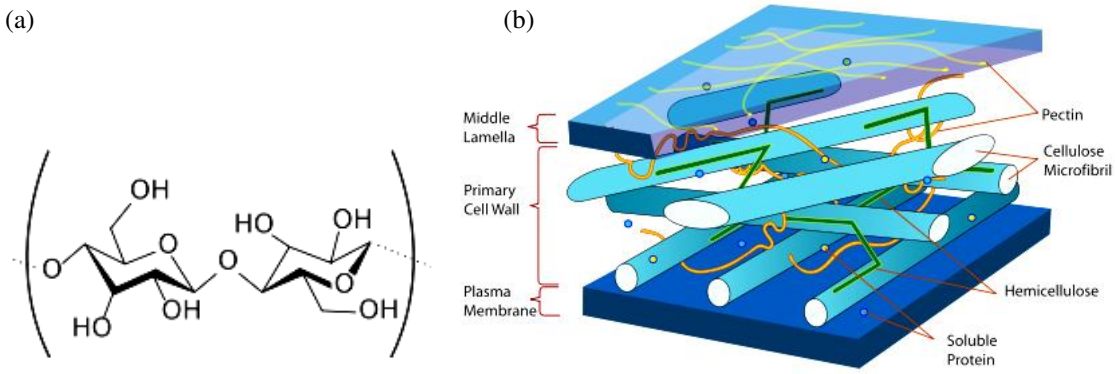

Figure 2-8. (a) Cellulose chemical structure. (b) A section of the plant cell wall (Image courtesy of www.wikipedia.org).

Microcrystalline cellulose powder was purchased from Sigma-Aldrich and dissolved in 9% w/w solution of LiCl/DMAc solvent according to the protocol given in ref (230). It has been postulated (231) that in the presence of an electrolyte like NaCl or LiCl, the cellulose chains would be more extended than in water due to the screening effect of the salt which overcomes the hydrogen bonding between the chains. Briefly, ~1-3% cellulose was suspended in the above solvent and the mixture was heated to 150°C and allowed to slowly cool to room temperature. Cellulose surfaces are slightly anionic, due to the presence of hydroxyl groups. Also, the surfaces of the cellulose microcrystallites possess sulfate groups, typically yielding an anionic charge on the order of 0.15e/nm^2 (232). Approximately 20 μL of

the cellulose solution was added to each well of a standard plastic 96-well flat-bottomed plate and allowed to dry in a desiccator overnight. The solidified cellulose films were incubated with both positively and negatively charged PS beads of 1.6-40 mg/mL in their respective buffer solutions, for 24 h at room temperature. The plates were read at 340 nm using a microplate reader (Biotek Gen 5) to quantify the total concentrations of the NPs. The measurements were repeated after washing away the non-adsorbed beads with their respective buffer solutions. On the basis of our measurements, an adsorption curve was plotted in Figure 2-9 for the amount of adsorbed PS beads (Q_{eq}) per milliliter of cellulose vs. the equilibrium or unadsorbed amount of PS beads (C_{eq}). The amount of adsorbed PS beads was calculated by subtracting the absorbance read after wash from that before wash. The absorbance of the control cellulose was subtracted from both. Under the set conditions, a significant increase of adsorption with PS bead concentration was observed for both types of beads. Saturation of adsorption was not reached for either of the charged beads, suggesting the possibility of a further increase of adsorption with increased PS bead concentration. The binding of both positively and negatively charged PS beads for the cellulose can be attributed to the hydrogen bond formation between the hydroxyl groups of the cellulose and the amidine and carboxylate groups on the PS beads. The roughness of the microcrystallite cellulose surfaces also provided numerous binding sites for the PS beads. Understandably, the negatively charged PS beads adsorbed slightly less than the positively charged beads, due to the electrostatic repulsion exerted by the hydroxyl and sulfate groups in the cellulose.

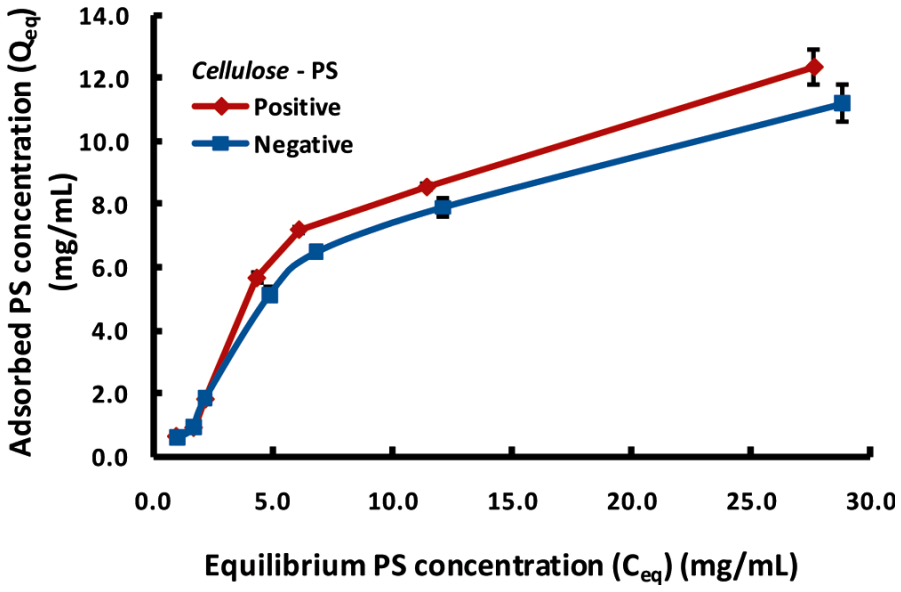

Figure 2-9. Adsorbed vs. equilibrium PS bead concentration for cellulose thin films exposed to positively (maroon) and negatively (blue) charged PS beads (178).

2.6. Interactions of PS with Algae

The algal cells were incubated on a shaker separately with both positively and negatively charged PS beads of 0.08-0.8 mg/mL, for 2 h at room temperature. All dilutions were made in the algal growth media. Three samples of each concentration were prepared to ensure experimental repeatability and establish error bars.

2.6.1. Qualitative visualization of interactions

The algal species were incubated with 4 mg/mL of differently charged PS beads for 24 h on a shaker. The mixtures were centrifuged at 30,000 rpm (27,090*g* RCF) for 3 min, and the supernatants were then removed. The pellets were resuspended in a 1:1 mixture of 2% osmium tetroxide and 4% sodium cacodylate buffer and kept overnight for fixation. The

fixed algae-PS samples were then dehydrated in gradient concentrations of ethanol. SEM imaging was conducted using a Hitachi S4800 scanning electron microscope, operated at a 10 kV accelerating voltage (Figure 2-10).

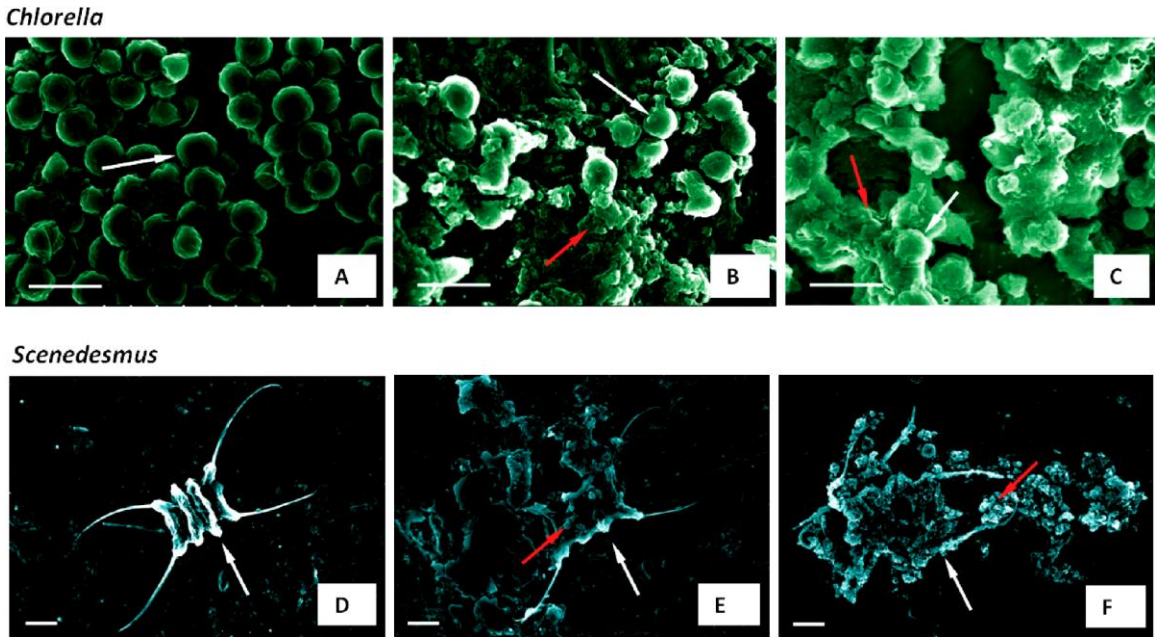

Figure 2-10. SEM images of algae adsorbed with PS beads. Incubation time: 24 h. (A) *Chlorella* control; (B) *Chlorella* with negatively charged PS beads; (C) *Chlorella* with positively charged PS beads; (D) *Scenedesmus* control; (E) *Scenedesmus* with negatively charged PS beads; (F) *Scenedesmus* with positively charged PS beads. Red arrows: nanoplastic aggregates. White arrows: algal cells. Scale bars for all: 5 μm (178).

Clearly, adsorption of the PS beads promoted algal aggregation. However, the aggregation was less pronounced with the negatively charged beads. This is understandable given the unfavorable, electrostatic repulsions between the negatively charged beads and the weakly negatively charged algal cell wall. In addition to surface adsorption, the positively

charged beads adsorbed onto the flagella of the *Scenedesmus* thus reducing their motility (Figure 2-10(F)).

2.6.2. Quantitative assessment of PS-algae interactions

As discussed in section 2.2.1, zeta potential is an excellent tool to study the stability of particles in solution. A ZetaSizer (Nano ZS, Malvern Instruments) was used to measure the change in zeta potential of algae induced by the adsorption of the PS beads. The algal species were incubated with 4 mg/mL of positively and negatively charged PS beads on a shaker, for 24 h at room temperature. As shown in Figure 2-11, *Chlorella* and *Scenedesmus* carried a zeta potential of -26.1 and -11.3 mV, respectively. Upon interaction with the positively charged PS beads, both algal species displayed an increase in zeta potential. Specifically, the zeta potential of *Chlorella*-PS beads increased by 85.8 mV, whereas the zeta potential of *Scenedesmus*-PS beads increased by 56.3 mV. In contrast, upon binding with the negatively charged PS beads, the zeta potential of *Chlorella*-PS beads slightly decreased by 9.0 mV, whereas the zeta potential of *Scenedesmus*-PS beads decreased by 14.6 mV. These measurements suggested that positively charged PS beads possessed a higher binding affinity than the negatively charged ones for the algae, consistent with our binding assay conducted with the PS beads and the cellulose film shown in Figure 2-9. Such consistency implied that cellulose played an essential role in initiating the binding between the algae and the plastics.

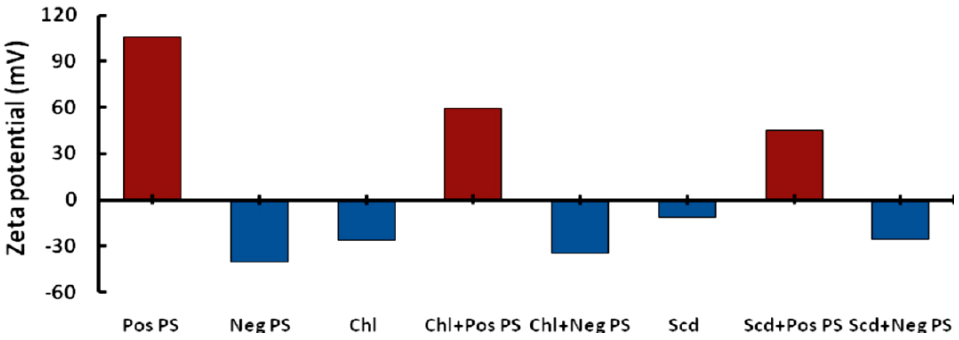

Figure 2-11. Zeta potentials of positively charged PS beads, negatively charged PS beads, *Chlorella* control, *Scenedesmus* control, and *Chlorella* and *Scenedesmus* mixed with positively and negatively charged PS beads. Abbreviations: "Pos" stands for positive, "Neg" for negative, "Chl" for *Chlorella*, and "Scd" for *Scenedesmus* (178).

To quantify the adsorption process, the Freundlich model (Equation 2-2) was used to derive the association constants for the PS-algae systems. A UV-vis spectrophotometer (Biomate 3) was used to quantify the amount of the PS beads adsorbed on the algae. Absorbance was recorded at 260 nm before and after adding various concentrations of the PS beads to the algal growth medium. At this wavelength, the PS beads showed a strong absorbance. After 2 h of incubation, the algae-PS bead solution was filtered through membranes with a pore size of 0.2 μm (Whatman Anotop). Similar to the QD-algae mixtures, a 2 μL portion of NaOH was added to the algae-PS solutions with anionic beads to facilitate their filtration through the weakly acidic membranes. At the low concentrations used, PS controls showed similar absorbances before and after filtration, indicating negligible mutual aggregation. Hence, all algal cells were blocked by the membranes due to their large size, while the absorbance of the filtrate indicated the amount of free or unadsorbed PS beads. The amount of adsorbed PS beads can be calculated by Equation 2-5:

$$Abs_{adsorbed} = (Abs_{PS+algae} - Abs_{algae}) - Abs_{filtered} \qquad (2\text{-}5)$$

where $Abs_{filtered}$ and $Abs_{PS+algae}$ denote the absorbance of the algae-PS bead solution after and before filtration, respectively, and Abs_{algae} is the absorbance of the algae alone. An adsorption curve was established by varying the PS bead concentration from 0.08 to 0.8 mg/mL (Figure 2-12). The curve shows a rapid increase in adsorption with the dosage of positively charged PS beads, for both algal species. As expected, there was negligible adsorption observed for negatively charged PS beads (Figure 2-12). To further characterize the adsorption processes, we fit our adsorption data to the Freundlich equilibrium model for the PS beads. The values of n obtained were 1.70 and 2.22 for *Chlorella* and *Scenedesmus* incubated with positively charged beads and 0.55 and 0.66 for negatively charged PS beads, respectively. As illustrated in Figure 2-12, both the adsorption isotherms for *Chlorella* and *Scenedesmus* within the selected PS concentration range suggest a further increase in adsorption is possible with increased positively charged PS beads. Also, the affinity of negatively charged beads was higher for *Chlorella* than *Scenedesmus* (Figure 2-12(b)). This difference in the adsorption characteristics by the two algal species could be attributed to the more rugged morphology and higher total surface area of *Scenedesmus* than *Chlorella* (Figure 2-10). Specifically, *Chlorella* is spherical and single-celled, while *Scenedesmus* is an ellipsoidal, 4-celled assembly. In addition to morphology, *Scenedesmus* unlike *Chlorella* also possesses two pairs of flagella responsible for its agile motility in the aquatic environment. Its cell wall also consists of hemicellulose as mentioned in section 2.2.2., which is a branched structure in contrast to cellulose, and hence affords a 3D scaffold for adsorption of the PS beads. The k values obtained from the model fitting were 39.18 $(mg/mL)^{1-n}$ for *Chlorella* and 43.09 $(mg/mL)^{1-n}$ for *Scenedesmus* for the positively charged PS beads, further substantiating the observation that the algal species, especially *Scenedesmus*, possessed a high binding affinity for the positively charged PS beads. Although each

Scenedesmus complex had more than twice the surface area than *Chlorella*, the total number of *Chlorella* cells outnumbered *Scenedesmus* by approximately 20 times per unit volume of the culture media. This led to a more pronounced adsorption and more robust nonspecific interaction between the *Chlorella* and the negatively charged PS beads, as indicated by Figure 2-12(b). This was quantitatively substantiated by the Freundlich coefficient k, which was determined to be 0.58 and 0.54 $(mg/mL)^{1-n}$ for *Chlorella* and *Scenedesmus*, respectively. (178)

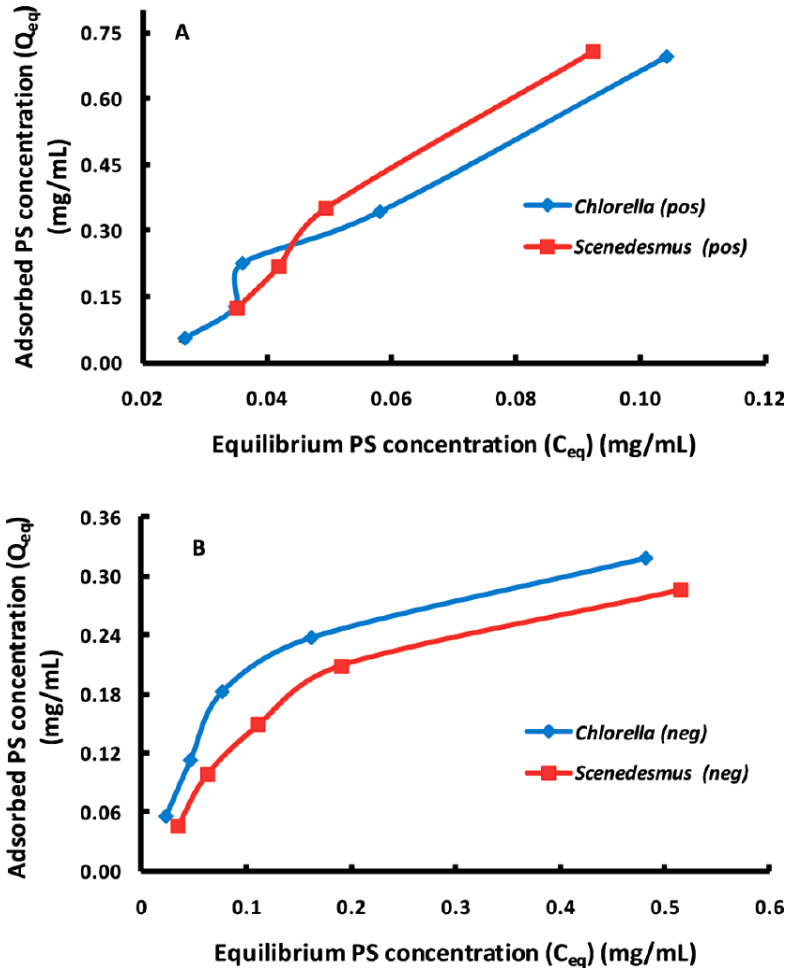

Figure 2-12. Adsorbed vs. equilibrium PS concentrations for (A) positive and (B) negative PS beads exposed to *Chlorella* (blue) and *Scenedesmus* (red) (178).

2.6.3. Effects of PS adsorption on algal photosynthesis

The photosynthetic reaction is described by Equation 2-3. To evaluate the effects of PS bead adsorption on algal bioactivities, the carbon dioxide depletion of the algae was examined in the presence of PS beads of 1.8-6.5 mg/L of algal solution. A bicarbonate indicator solution (0.2 g of thymol blue, 0.1 g of cresol red, in 0.01 M $NaHCO_3$) was prepared to monitor the depletion of CO_2, the activity of which is given by Equation 2-7. The algae-PS bead solution was mixed with the indicator solution, and the samples were tightly sealed to prevent gas exchange. During photosynthesis and respiration, the algae consumed or released CO_2 over time, causing the pH value of the indicator solution to increase or decrease, within a range of pH 4-8, accordingly. A transition from acidic to basic conditions was indicated by a color change from orange-red to deep purple, whereas a decrease in pH was indicated by a color change from orange-red to yellow, accompanied by an increase or decrease of absorbance at 574 nm, respectively. The changes in CO_2 depletion were then calculated on the basis of the increase or decrease of absorbance values for different sample concentrations (Figure 2-13). Absorbance of the control algal species and the control PS beads was also read over time.

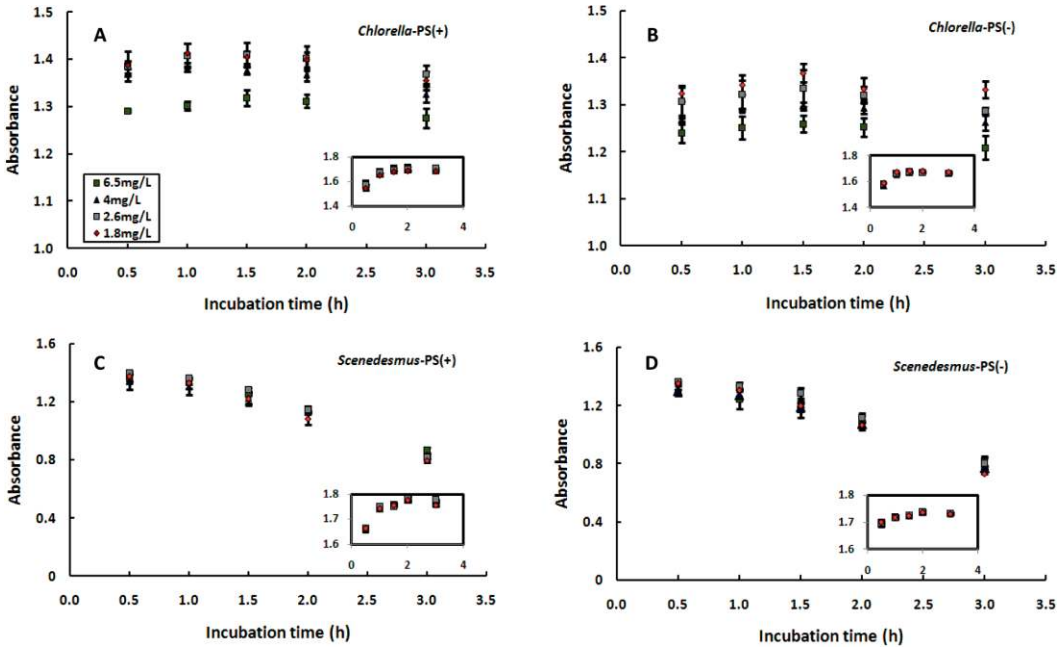

Figure 2-13. Absorbance vs. incubation time for (A, B) *Chlorella* and (C, D) *Scenedesmus* exposed to positively and negatively charged PS beads of 1.8-6.5 mg/L of algal solution. The insets represent the sums of absorbance for the control algae and the four PS concentrations prior to their incubation. All absorbances read at 574 nm. The legend in the first plot applies to the symbols in all four plots and their insets (178).

According to Equation 2-4, an increase in pH corresponds to a decrease in the concentration of CO_2 in the bicarbonate indicator solution, which can be monitored by measuring the absorbance of the indicator at 574 nm. Figure 2-13 shows an addition of the absorbance of control algae and PS bead solutions prior to incubation. The absorbance of the indicator solution with control PS beads was stable over time at 574 nm for all concentrations, and that of the solution with control algae initially increased with time, gradually reaching stability, indicating an initial increasing rate of photosynthesis which became constant after 1.5 h. In contrast, as shown in Figure 2-13(a) and (b), an increased dosage of PS beads added to *Chlorella* resulted in a significant decrease in CO_2 depletion at

and above a PS concentration of 1.8 mg/L of algal solution. The trend is similar for both positively and negatively charged PS beads. This hindered CO_2 depletion could be caused by the light shading effect of the adsorbed PS beads, and/or by obstructed CO_2 gas flow and nutrient uptake pathways. In the case of *Scenedesmus*, adsorption of both positively and negatively charged PS beads also resulted in reduced absorbance with increased PS concentration, similar to that observed for *Chlorella*. Furthermore, the absorbance for *Scenedesmus* decreased approximately 40% over 4 h of incubation for all PS concentrations, indicating onset of algal respiration (Figure 2-13(c) and (d)). A decrease in absorbance of the indicator solution reflects a decrease in pH, corresponding to an increase in the CO_2 concentration in the algal solution. Such increased CO_2 concentration implies that the algae consumed the oxygen dissolved in the solution and released CO_2, a process known as cellular respiration. Cellular respiration in algae is a process by which food molecules are metabolized to convert to chemical energy for the cell. It occurs in the opposite direction as photosynthesis and is usually triggered in the absence of light. The energy produced by respiration is a source for algal motility. As shown in our SEM micrographs (Figure 2-10(f)), aggregation of the PS beads obstructed the flagella of the *Scenedesmus*. The algal species thus were forced to carry out respiration faster than photosynthesis in order to regain its motility. In addition, adsorption of the PS beads on algae could block light from reaching the photosynthesis centers and, although not observed in the present study, could damage the algal cell wall to induce pore formation, which could lead to uptake of the PS beads by the algae.

2.6.4. Oxidative stress on algal cells due to PS adsorption

A number of different ROS, including the superoxide anion ($O_2^{\cdot-}$), hydrogen peroxide (H_2O_2), singlet oxygen (O_2 ($^1\Delta_g$)), and the hydroxyl radical (OH^-) are normal byproducts of oxidative metabolism but can be extremely harmful to organisms at high concentrations. ROS can oxidize proteins, lipids and nucleic acids, often leading to alterations in cell structure and mutagenesis (233). Photosynthesis constitutes an electron transport chain. Since a common biological source of $O_2^{\cdot-}$ is the single-electron reduction of molecular oxygen by electron transport chains, photosynthetic organisms are under severe threat of elevated ROS production (234). When photosynthetic efficiency decreases, ROS are formed as a result of the diversion of electrons to O_2 but not CO_2 (235). Any reduction in electron transfer will enhance ROS production. Due to the presence of a high electron flux in their microenvironment, which also is rich in oxygen and metal ion concentrations, the mitochondria and chloroplasts of photosynthetic organisms are susceptible to high oxidative damage. Also, the effect of ROS in photosynthetic organisms is exacerbated by excessive illumination. For instance, excessive light energy input may increase the levels of singlet state O_2 ($^1\Delta_g$) which is highly electrophilic and capable of oxidizing many other molecules (234). Thus, although many ROS-generating processes are slow under normal conditions, pollutants, xenobiotics, and environmental factors such as high light or UV exposure can accelerate them.

An ROS assay, OxiSelect ROS Assay Kit (Cell Biolabs, Inc.), based on the fluorescent probe dichlorofluorescein (DCF) was used to scrutinize the generation of ROS in algal cells. DCF has been used previously in plant cell cultures to distinguish between

sources of elicited ROS in tobacco epidermal cells (236) and visualize oxidative processes in response to mechanical stress (237). The assay employs the cell-permeable fluorogenic probe 2', 7'-Dichlorodihydrofluorescin diacetate (DCFH-DA). In brief, DCFH-DA is diffused into cells and is deacetylated by cellular esterases to non-fluorescent 2', 7'-Dichlorodihydrofluorescin (DCFH), which is rapidly oxidized to highly fluorescent 2', 7'-Dichlorodihydrofluorescein (DCF) by ROS (Figure 2-14). DCFH exhibits selectivity for H_2O_2 over other free radicals (238). However, *in vivo* conversion of other radicals to H_2O_2 could react with the probe indirectly. The fluorescence intensity is proportional to the ROS levels within the cell cytosol.

In our experiment, specifically, 98 μL of algal cells were preincubated with 100 μL of a 20× diluted solution of DCFH-DA in algal growth media for 10 min in a black 96-well plate. Approximately 2 μL of the PS solutions was added to the plate to give a total bead concentration of 6.5 mg/L. The fluorescence of the mixtures was examined using a Cary Eclipse fluorescence spectrofluorometer (Varian Inc.) over time. The samples were excited at 480 nm and the emission read at 530 nm, with 20 nm excitation and emission slit widths and 10 s exposure time set for each well. To establish error bars, fluorometry experiments were performed in triplicates, and fluorescence intensities as a function of time were plotted (Figure 2-15).

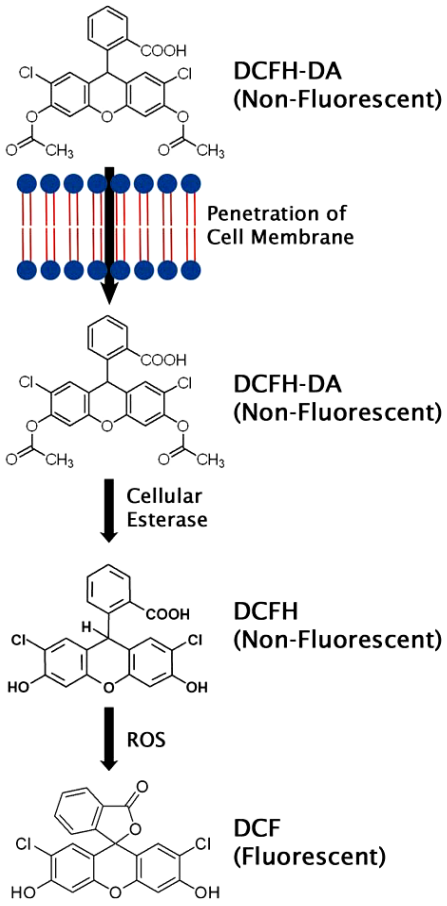

Figure 2-14. Mechanism of DCF assay (Image courtesy: OxiSelect™ ROS Assay Kit product manual, Cell Biolabs, Inc.).

As can be seen in Figure 2-15(a) and (b), for both algal species, adsorption of the positively charged PS beads resulted in a ROS burst and a higher rate of ROS production than the negatively charged beads. Also, *Scenedesmus* samples showed slightly higher levels of ROS production. These observations are consistent with our earlier results that plastic nanoparticles reduced photosynthesis for both algal species, and increased respiration in *Scenedesmus* led to increased O_2 activity (Figure 2-13).

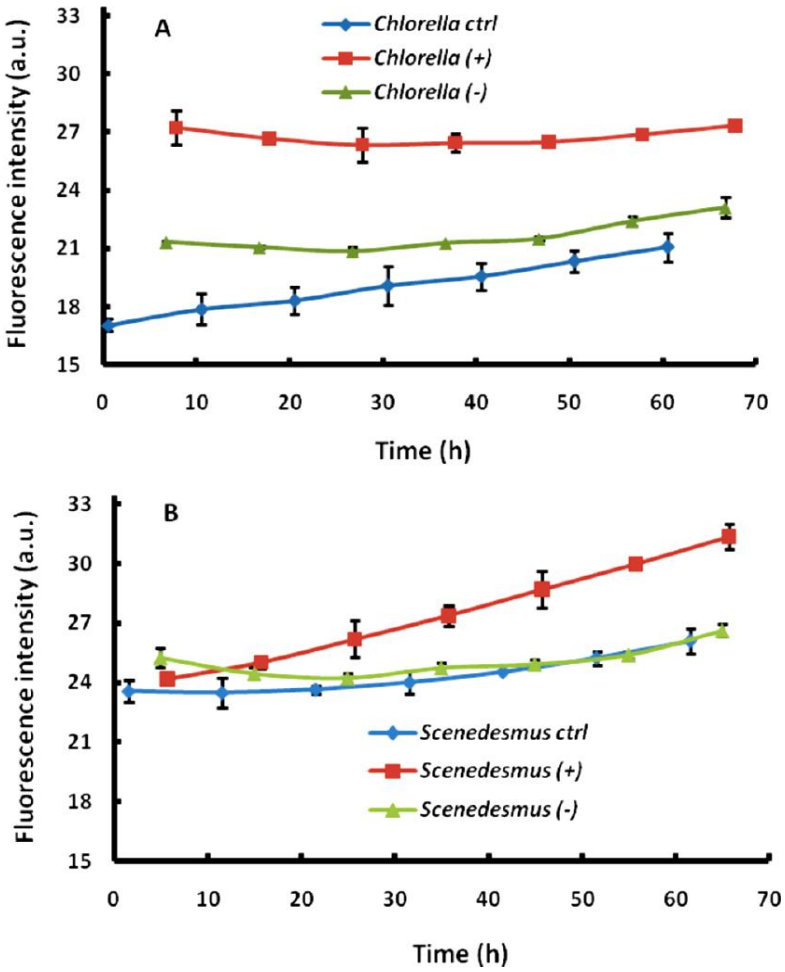

Figure 2-15. ROS production rates by (A) *Chlorella* (blue) and (B) *Scenedesmus* (blue) due to positive (maroon) and negative (green) PS adsorption. The fluorescence intensity is proportional to the level of the ROS produced. Concentrations of the positively and negatively charged PS beads: 6.5 mg/L of algal solution (178).

2.7. Discussions and Summary

We have carried out adsorption studies of synthetic NPs, specifically CdSe/ZnS QDs and both positively and negatively charged PS NPs on single and multi-celled green algae, and evaluated the effects of such adsorption on the photosynthesis of the algal species. It was found using the Freundlich adsorption model that both nanomaterials have a high

affinity for the algal cells and the adsorption could be facilitated by nonspecific interactions such as electrostatic interactions, as well as possible internalization through pore formation. While QDs coated with MUA adsorbed onto the porous cell wall structure of *Chlamydomonas* sp., positively coated PS NPs adsorbed more favorably onto both *Chlorella* and *Scenedesmus* sp. than their negative counterparts due to electrostatic interactions between the PS NPs and the negatively charged cellulose in the algal cell walls. The adsorptions depended logarithmically on the concentration of the NPs as well as on the physicochemical properties of the NPs and the morphological and biochemical properties of the algae. Further, the adsorptions hindered the photosynthetic activity of the algae, as evidenced by declined CO_2 depletion and O_2 production. In *Scenedesmus*, an increased respiration was observed due to restriction of the mobility of the algae as a result of PS binding with their flagella. Harmful ROS production was also noted as a result of PS NP adsorption onto algal cells.

PART II

ENVIRONMENTAL APPLICATIONS OF NANOMATERIALS

CHAPTER THREE

ENVIRONMENTAL APPLICATIONS OF NANOMATERIALS

I. Understanding the Physico-Chemical Behavior of Dendrimers in Hosting a Variety of Chemical Species

Chapter three aims at understanding the fundamental physico-chemical behavior of PAMAM dendrimers in hosting a diversity of chemical species for the purpose of environmental remediation. Specifically, the high capacity of a poly(amidoamine)-tris(hydroxymethyl)amidomethane dendrimer (tris-dendrimer) for the physical adsorption of various chemical species, namely, cationic copper, anionic nitrate, and PAH phenanthrene (PN) is discussed. A pH-dependent specificity was observed for the dendrimer, and the stoichiometric ratios of its binding with the chemical species were determined using UV-vis spectrophotometry. Cationic copper and anionic nitrate coordinated with the amine groups of the dendrimer through complexation and electrostatic interaction, while PN partitioned into the dendrimer interior through hydrophobic interaction. Furthermore, the efficiency of PAMAM dendrimer as a high capacity ligand for humic substances has been established based upon electrostatic and hydrophobic interactions, as well as hydrogen bonding. These proof-of-concept studies point to the vast potential of using PAMAM dendrimers for supramolecular assembly, environmental remediation, and nanomedicine.

3.1. Introduction

The most appealing characteristics of dendrimers such as their pH-dependent contraction and swelling, amphiphilicity, ample interior voids, high density of peripheral functional groups, thermal stability, flexibility, low viscosity and high biocompatibility (162) have stimulated research activities over the past few decades in polymer science (239), toxicology (240), environmental engineering (170, 241, 242), and gene and drug delivery (243-245). Molecular dynamics (MD) simulations (246) showed that the porous interior of a PAMAM dendrimer afforded numerous cavities for accommodating guest species. The primary and tertiary amines of the amine-terminated PAMAM dendrimer are fully protonated at pH 4 ($pK_a \sim 4$) and fully neutralized at pH 10 ($pK_a \sim 9$). Hence, at pH 7, the interior of the PAMAM dendrimer stays relatively hydrophobic, while the exterior is protonated affording it good water solubility (247). Recent studies have also shown that dendrimers such as PAMAM and poly(propylene imine) are capable of encapsulating PAHs,(248) inorganic solutes, and metal cations and anions and then reversibly releasing the contaminant loads upon changing the solvent pH and electrolyte strength or by a UV trigger (241, 242, 249). Such binding versatility implies that dendrimers may act as a host for a variety of chemical species and serve as a "nanosponge"(248) for the remediation of contaminated water and soils (250). It is noted that research to date has been primarily focused on dendrimers with either $-NH_2$ or -OH surface groups and for high concentrations of absorbates. For example, Diallo et al. first employed amine-terminated PAMAM dendrimers as a high capacity, recyclable, and nanoscale container for transition metal ions (251). Zhou et al. studied the interaction between OH-terminated PAMAM dendrimer and Cu(II) using matrix-assisted laser desorption (MALDI) (252). Lard et al. demonstrated the

energy transfer between phenanthrene (PN), a PAH, and a major environmental pollutant, and Alexa Fluor 350 labeled amine-terminated PAMAM dendrimer (166). In contrast, research on the commercially available tris-dendrimer has been surprisingly scarce. However, the tri-functional hydroxyl-surface groups and ample inner structural voids of the tris-dendrimer (Figure 3-1) suggest its high capacity in hosting cationic, anionic, and hydrophobic guest species, a characteristic not readily available from any specific mono-functional NH_2 or OH-terminated PAMAM dendrimer. Herein, we report the absorption of three different chemical species— cationic copper (Cu(II)), anionic nitrate (NO_3^-), and PAH (PN) by a tris-dendrimer. The selection of these chemicals ensures the consideration of surface charge and hydrophobicity of guest species and offers a comprehensive platform for evaluating the full-range hosting capacity of the tris-dendrimer. For example, Cu(II) is a transition metal ion which readily solubilizes in water to form complexes with *d-d* transitions throughout the near-ultraviolet, visible and near-infrared regions of the spectrum. Because of its unique electronic configuration, Cu(II) is capable of forming coordination complexes with a number of polydentate ligands. On the other hand, complexation of anions is a challenging task due to their large size and high free energy of solvation. NO_3^- is a weak base that does not readily form covalent bonds with metal cations or protons. However, it interacts in a non-coordinating manner with receptors through hydrogen bonding or electrostatic interactions. Hence the receptor should be able to form several non-covalent interactions simultaneously. In addition, the selectivity of the receptor toward NO_3^- in an aqueous environment is governed by its capability to host a mono-ionic, trigonal planar anion as opposed to other oxoanions such as sulfate, phosphate, and hydroxyls. In contrast to both cations and anions that have a significant solubility in water ($k_{Cu(II)}$ = 1250 g/L, k_{NO3-}

= 876 g/L) (254), PN is a PAH which is weakly soluble in water (k_{PN} = 1.29 mg/L) (255). Hence, its host should be able to partition PN into a hydrophobic environment in an aqueous solution. The unique chemistry of tris-dendrimer with a highly ordered chemical structure and tri-functional groups thus, could be exceptional in hosting chemical species of varying physical properties such as mentioned above. In the present work, specifically, the stoichiometric dendrimer-specie ratios are determined using UV-vis spectrophotometry, and the binding mechanisms are discussed thereafter. The use of Cu(II), NO_3^-, and PN is justified by their significant biological and environmental implications (256-259).

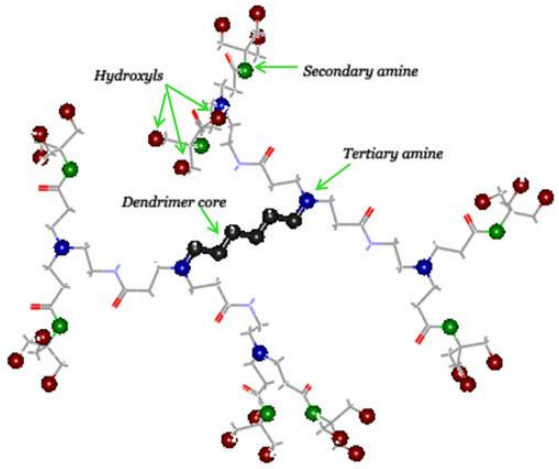

Figure 3-1. Structure of a generation 1 tris-dendrimer, the building block of the generation 4 tris-dendrimer used in the present study. Red, oxygen; green, secondary amine; blue, tertiary amine. (260).

In addition to the common toxic ions and PAHs found to pollute drinking water, humic substances also present severe environmental problems. Humic substances,

particularly humic acids (HA), form principle components of NOM which result from biodegradation and a chemical breakdown of animal and plant residues. Structurally, HA is a heterogeneous mixture of various aromatic and aliphatic molecules containing amines, catechols, quinones, carboxyl and phenolate functional groups which provide some hydrophilic character above pH 2. HA is resistant to further degradation and can therefore persist in natural and engineered systems. This may be problematic as HA can (i) pose as an environmental hazard by binding to trace metals, radionuclides and/or toxic and carcinogenic contaminants (261-263), (ii) regulate the transport and bioavailability of contaminants, and (iii) reduce the efficiency of water filtration membranes through fouling (264-266). Moreover, the complex and highly variable nature of HA often hinders their efficient removal. NOM poses a major challenge in drinking water purification systems owing to their high degree of fouling and disinfectant byproduct formation (264-267). The most commonly used methods for removal of NOM from drinking water include coagulation and flocculation, followed by sedimentation/flotation and sand filtration (268). Even though most of the NOM can be removed by coagulation, the hydrophobic fraction and high molar mass compounds of NOM are removed more efficiently than the hydrophilic fraction and the low molar mass compounds. Among the coagulants used, organic cationic polyelectrolytes such as chitosan and poly(DADMAC) have proved the most efficient (269). Regardless, a high dose of coagulants is usually required for the efficient removal of NOM, thus reducing the cost efficiency of the process. Furthermore, some of the coagulants also exhibit toxic effects (268). Therefore, alternative materials with enhanced coagulation properties must be developed for the better removal of NOM.

Dendritic nanotechnology is a promising new technology for the removal of NOM from water; these polymeric materials possess exceptional adsorption properties and their porous structures are ideal for trapping organic molecules. Further, the low viscosity, nano-size, and strong contaminant affinity of dendrimers facilitate enhanced contaminant removal via UF with minimal membrane fouling, allowing the system to be operated typically at low pressures (170). However, despite these apparent advantages, little attention has been paid to using dendrimers for membrane defouling. Herein, we report as a first study on the use of PAMAM dendrimers as an efficient, cost-effective, and re-usable nanotechnology for defouling of humic substances.

3.2. A Tris-dendrimer for Hosting Diverse Chemical Species

3.2.1. Materials and characterization

Generation 4 (G4) PAMAM tris-amidomethane dendrimer with a 1,6-diaminohexane core and 64 surface groups (MW = 18,178, 10 wt % in H_2O) was purchased from Sigma Aldrich and diluted in Milli-Q (pH 6.8) to 10 μM for use. The pH values of the dendrimer solution were adjusted to 2, 7, and 10 by titration using 1M NaOH or HCl. The hydrodynamic sizes of the dendrimers were measured by a Nanosizer (S90, Malvern Instruments), and the surface charges of the dendrimer at the three different pH values were determined by a Zetasizer (Nano ZS, Malvern Instruments). Copper nitrate hydrate ($Cu(NO_3)_2.xH_2O$, MW = 188), sodium nitrate ($NaNO_3$, MW = 85), and phenanthrene ($C_{14}H_{10}$, MW = 178) were obtained from Sigma-Aldrich and used as the sources of Cu(II), NO_3^-, and PN, respectively.

The tris-dendrimer possessed a zeta potential of -52.9mV at pH 10, -5.69mV at pH 7, and 6.5 mV at pH 2, respectively. The positive charge of the dendrimer at low pH was due to the protonation of its tertiary amines; however, the low charge can be attributed to the shielding of positive charge by the counterions (Cl^-) in solution. Significant penetration of counterions towards the dendrimer core has been observed in higher generation dendrimers (270). These counterions shield the excess polymer charge near the core due to backfolding of the surface groups with increasing generation (271). The large negative charge of the dendrimer at pH 10 can be regarded due to the electron cloud dislocation as a result of the effective OH bond stretching on the terminal methyl groups, triggered by the interactions between the OH^- ions from NaOH in solution and the trihydroxyl surface groups on the dendrimer. Deprotonation of the dendrimer surface hydroxyl groups can be ruled out based on the large pK_a value of CH_3OH ($pK_a = 15$). The low negative charge at neutral pH may be attributed to the aforedescribed bond stretching as well. The tris-dendrimer exhibited the largest hydrodynamic size (diameter) of 4.5 nm at pH 10 compared to that of 3.1 nm at pH 2 and 2.3 nm at pH 7. Such dependence of dendrimer size on solvent pH is understandable, since the electrostatic repulsion between the three partially charged hydroxyls of each dendrimer surface group at pH 10 favored an open structure, whereas the decrease in partial charge of each dendrimer surface group compromised the electrostatic repulsion to yield a relatively hydrophobic dendrimer interior at neutral pH. At low pH, in contrast, protonation of the tertiary amines and neutralization of the surface groups promoted the dendrimer interior to become hydrophilic and the dendrimer to swell in comparison with that at neutral pH (refer to Figure 3-1a). A 48.8% maximum swelling at high pH was observed for the dendrimer in our experiment. This is in accordance with previous molecular dynamics

simulations (272) on the pH response of charged dendrimers, where a 15% and a 50% maximum swelling were observed for the radius of gyration of the dendrimers, assuming rigid and soft bonds, respectively.

3.2.2. Characterization of dendrimer-chemical binding

To characterize the binding of the tris-dendrimer with the three different chemical species, the absorbance spectra of the dendrimer-specie complexes were measured against the control dendrimer and the chemicals using a UV-vis spectrophotometer (Biomate 3). All measurements were done using quartz cuvettes. The concentration of the dendrimer in each aqueous solution was kept constant at 10 μM while the concentrations of the species were varied. Specifically, the water-soluble Cu(II) and NO_3^- were diluted in Milli-Q, while the hydrophobic PN was dissolved in methanol. The mixtures of Cu(II), NO_3^-, and PN with the tris-dendrimer were prepared at pH 10, 2, and 7, respectively, with the molar ratio of tris-specie kept at 1:10. The mixtures were then incubated for 30 min on a shaker prior to the measurement. Survey scans of the absorbance of the control dendrimer, the chemicals, and the dendrimer-chemical complexes were conducted for the wavelength range of 190-800 nm. The signature peaks for the dendrimer-chemical complexes were identified. The binding dynamics of the tris-chemicals were established by measuring the absorbance of the complexes at their characteristic peak wavelengths, i.e., 300 nm for tris-Cu(II), 210 nm for tris-NO_3^-, and 250 nm for tris-PN.

The unique pH responses in the structure and net charge of the tris-dendrimer were utilized to absorb the charged and noncharged chemical species in aqueous solutions. Specifically, tris-Cu(II) and tris-NO_3^- showed characteristic broad absorbance peaks around

300 and 210 nm, respectively, whereas tris-PN displayed an increase in the PN absorbance peak at 250 nm (Figure 3-2(a-c)). The appearance of characteristic peaks for tris-Cu(II) and tris-NO_3^- indicates the formation of dendrimer-chemical complexes. The interaction mechanisms are discussed in detail below:

1. *Dendrimer-metal complexes:* Specifically, Cu(II) complexed with the secondary and tertiary amine groups of the tris-dendrimer at high pH to yield a broad absorbance peak at 300 nm (290-340 nm). Such an absorbance peak is attributed to the ligand-to-metal charge transfer (LMCT) (273) between Cu(II) and the ligand groups on the tris-dendrimer. Copper in aqueous solutions exists as hexadentate $Cu(H_2O)_6^{2+}$ complexes, which undergoes ligand exchange upon interaction with the tris-dendrimer. Plausible locations of the Cu(II) are indicated in Figure 3-2a (right panel), following the proposed model by Ottaviani et al. (274). Coordination of Cu(II) with terminal OH groups is, however, believed to be unfeasible (275). It has been shown earlier that metal ions, including Cu^{2+}, Ag^{+}, Pt^{2+}, Pd^{2+}, Ru^{3+}, and Ni^{2+}, partition into the interior of PAMAM dendrimers, where they are strongly complexed by interior functional groups (274, 276, 277). The band arising from LMCT was much stronger than that from the *d-d* transition between 600 and 800 nm (data not shown), possibly due to the low concentration (100 μM) of Cu(II) used. The low concentration of Cu(II) also did not result in the formation of copper clusters within the dendrimer. This could be inferred from the absence of the absorption peak around 570 nm that typically arises from the Mie plasmon resonance of small copper clusters (277).
2. *Dendrimer-anion binding* - At low pH, NO_3^- formed complexes with the protonated tertiary amines of the tris-dendrimer, as represented by an increase in the magnitude

and change in the absorbance profile of the tris-NO_3^- near 210 nm (Figure 3-2b). In the case of metal ions such as Cu(II), transition-metal receptors are Lewis bases that donate a pair (or pairs) of electrons to the metal via a coordinating bond. In anion coordination, the lone pair of electrons is donated in the reverse fashion from the anion to a hydrogen atom on the ligand, resulting in hydrogen-bond formation. The binding cavity then orients the H-bond in a trigonal planar coordination sphere in accordance with NO_3^- coordination.

3. *PAH encapsulation by dendrimers* - As illustrated in Figure 3-2c, at neutral pH, the interaction between the PN and the tris-dendrimer is indicated by an increase of the PN absorbance peak at 250 nm, reflecting the partitioning of PN from methanol to the dendrimer in the aqueous phase. It is worth noting that new absorbance bands emerged for Cu(II) and NO_3^- upon their electrostatic interactions with the tris-dendrimer. For PN, however, only an increase of the absorbance occurred resulting from its partitioning from the aqueous phase to the relatively hydrophobic dendrimer interior. The interactions of the π-electron orbitals of the PN with the surface hydroxyl groups of the dendrimer can be ruled out due to the physisorbed waters forming H-bonds with the surface hydroxyl groups.

Thus, the UV-vis measurement provided a direct evidence that tris-dendrimer can serve as a versatile host for guest species NO_3^- at low pH, PN at neutral pH, and Cu(II) at high pH. However, the projected locations of the chemical species within the dendrimer are still speculative at this point.

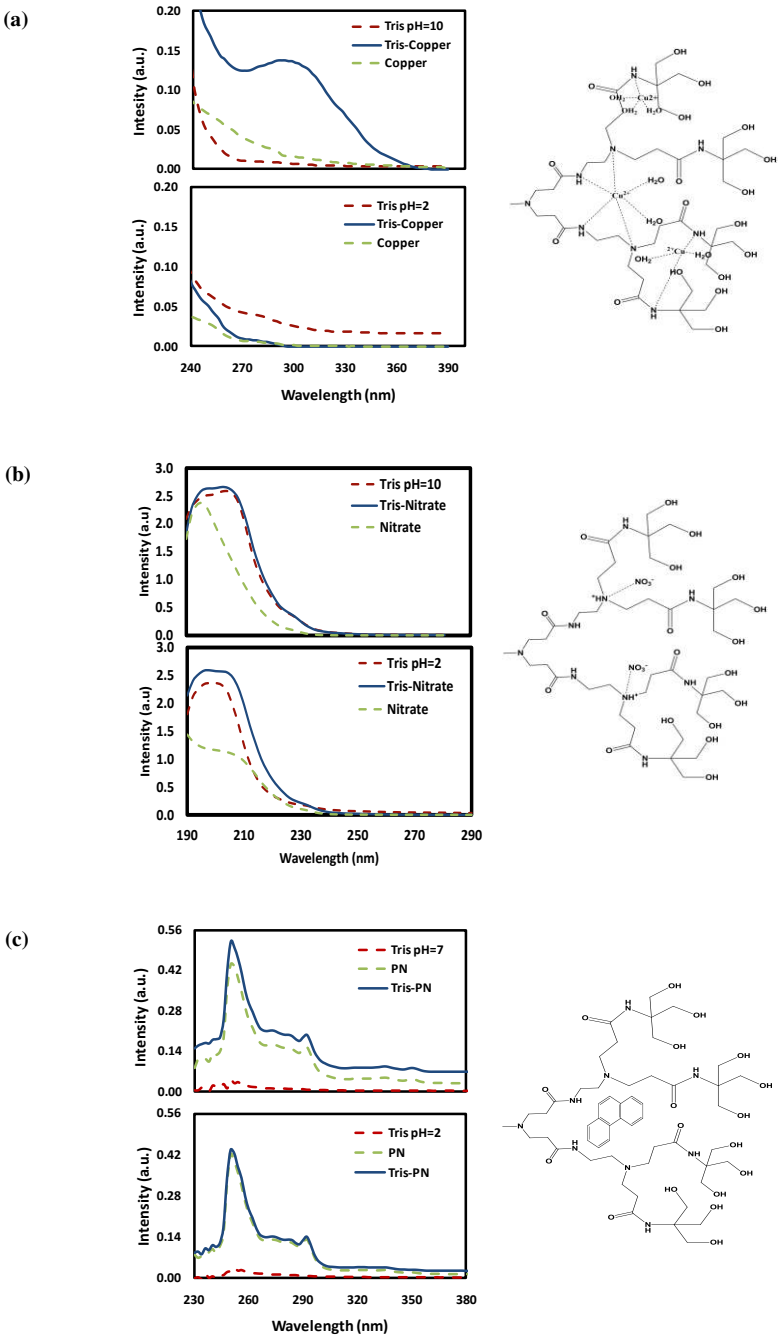

Figure 3-2. Absorbance spectra of (a) control tris-dendrimer, control copper, and tris-copper complex at pH 10 and 2, and enlarged branch of tris-dendrimer, and possible copper coordinations at pH 10, (b) control tris-dendrimer, control nitrate, and tris-nitrate complex at pH 10 and 2, and enlarged branch of tris-dendrimer and possible nitrate coordinations at pH 2, and (c) control tris-dendrimer, control PN, and tris-PN complex at pH 7 and 2, and enlarged branch of tris-dendrimer and possible PN localization at pH 7 (260).

The normalized binding dynamics between Cu(II), NO_3^-, and PN with the tris-dendrimer are presented in Figure 3-3. The optimum loading for tris-Cu(II) and tris-NO_3^- occurred immediately after their initial mixing and saturated over time. In comparison, the phase separation of PN started around 15 min but did not reach completion during our observation time of 48 h. This is a result of an incomplete evaporation of the methanol from solution. These dynamics further delineate the hypothesis that different binding processes took place for charged vs. noncharged chemical species with the tris-dendrimer. Such contrasting binding dynamics can also be attributed to the fundamental differences between the long-range electrostatic interactions for tris-Cu(II) and tris-NO_3^- and the hydrophobic interaction for tris-PN which occurred only within the dendrimer.

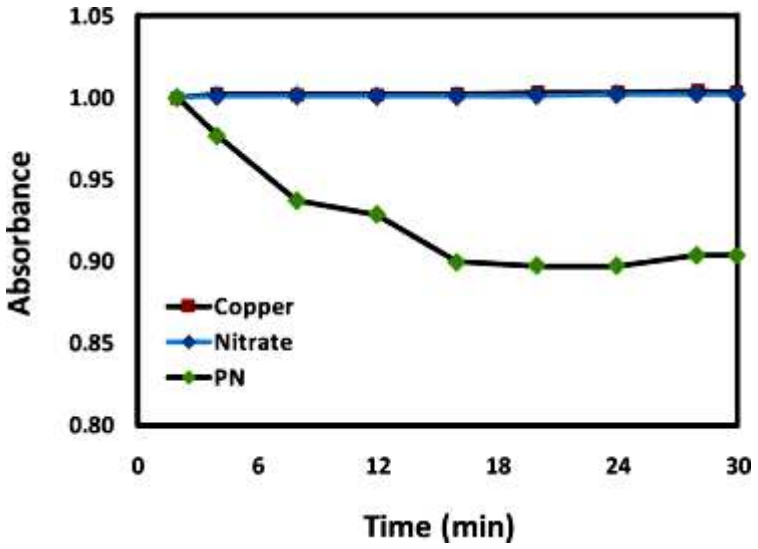

Figure 3-3.The binding dynamics of Cu(II), NO_3^- and PN with tris-dendrimer. The absorbance readings were obtained at 300 nm for tris-Cu(II), 210 nm for tris-NO_3^-, and 250 nm for tris-PN, respectively, immediately following their initial incubations (260).

To determine the maximum binding capacity of the tris-dendrimer for the chemical species, we further characterized the number of chemical species absorbed per dendrimer through spectrophotometric titration. Parts a-c of Figure 3-4 indicate that each tris-dendrimer absorbed up to 64 Cu(II) ions, 32 NO_3^- ions, and 10 PN molecules, respectively. It is therefore reasonable to infer that the Cu(II) ions coordinated with the 64 secondary amine surface groups of the tris-dendrimer at high pH whereas the NO_3^- ions electrostatically bound with the protonated tertiary amine groups of the dendrimer interior at low pH as well as through hydrogen bonding with the amido amines. These observations are consistent with previous research on the binding of Cu(II) onto a G4 hydroxyl-terminated dendrimer (277). However, for PN, we could approximately quantify the absorption capacity and dynamics in the following way. The amount of methanol which evaporated from solution was measured indirectly by measuring the absorbance of the control PN solution periodically. This gave us an estimated amount of PN partitioned to the air-water interface of the solution and the fraction of the partitioned PN absorbed by the tris-dendrimers. According to Beer-Lambert's law,

$$[PN]_n = I_{PNn} \times \frac{[PN]_0}{I_{PN0}} \qquad (3\text{-}1)$$

where $[PN]_n$ and $[PN]_0$ are the concentrations of PN in solution at time $t=n$ and 0 respectively, and I_{PNn} and I_{PN0} are their respective absorbance intensities. By assumption that the concentration of PN at time $t=0$ is the total concentration of PN in solution, i.e., $[PN]_0=[PN]_T$ and $I_{PN0}=I_{PNT}$, we have

$$[PN]_S = [PN]_T - [PN]_n \qquad (3\text{-}2)$$

$$[PN]_x = \frac{[PN]_T \times I_{mixn}}{I_{PNT}} \qquad (3\text{-}3)$$

where $[PN]_s$ is the concentration of the PN partitioned to the air-water interface, and $[PN]_x$ accounts for the concentration of the PN absorbed into the dendrimer and that is left in solution. Since the absorbance of the mixture is higher than the control PN at any time *t*, it is a good approximation to conclude that this extra absorbance can be attributed to the PN which has been absorbed by the tris-dendrimer from the PN partitioned to the air-water interface of the solution. Hence, the fraction of the total PN partitioned to the air-water interface of the solution absorbed by the dendrimer at the interface is given by

$$y = \frac{[PN]_x - [PN]_n}{[PN]_s} \qquad (3\text{-}4)$$

A plot of *y* vs. the ratio of PN to tris-dendrimer (Figure 3-4c) indirectly indicates that the tris-dendrimer reached its full capacity of capturing PN into its interior on reaching a ratio of 10:1 for PN:tris-dendrimer. Such a PN loading capacity of 98 mg/g was better than for a functionalized poly(propyleneimine) (PPI) (44-67 mg/g) earlier reported (248). This higher loading capacity could be attributed to the fact that in our experiment, the PAMAM dendrimers were free in solution and hence the entire 3D structure was available to the PN molecules, whereas in the above mentioned study, PPI dendrimers were rendered completely water insoluble by functionalization and the adsorption experiments were carried out on dendrimer thin films. The formation of thin films sacrificed partial dendrimer encapsulation capability due to their collapse on the substrate. At neutral pH, none of the tertiary amines of the tris-dendrimer were charged, and the neutral tris-dendrimer interior afforded a high affinity for the PN.

As mentioned in Chapter two (section 2.2.1), we employed viscometry to measure the increase in the hydrodynamic size of a PAMAM dendrimer on encapsulating PN. The intrinsic viscosity of a NP is a property which gives us information on the solute-solvent interactions during their transport behavior in aqueous state. The drag caused by relative motion of the fluid and a surface is a measure of the viscosity. An Ubbelohde viscometer which consists of a U-shaped glass tube is held vertically in a controlled temperature bath. The time taken for the level of the liquid to pass between two marked points in a bulb-shaped capillary, which is proportional to the kinematic viscosity, is measured. The determination of viscosity is based on Poiseuille's law:

$$\frac{dV}{dt} = \pi R^4 \frac{|\Delta P|}{8\eta L}, \qquad (3\text{-}5)$$

where t is the time it takes for a volume V to elute. The ratio dV/dt depends on R as the capillary radius, on the average applied pressure P, on its length L and on the dynamic viscosity η. The viscosity radius, which is also the hydrodynamic radius, is derived from the intrinsic viscosity, $[\eta]$ of the analyte from Equation 3-6:

$$R_\eta = \{3[\eta]M / 10\pi N_A\}^{1/3}. \qquad (3\text{-}6)$$

Since this method employs the infinite dilution assumption, the true molecular radius is obtained. It was observed that a G4-PAMAM dendrimer's radius increased from 2.03 nm for a pure G4-PAMAM to 2.35 nm for a G4-PAMAM encapsulating PN molecules at pH 10. This 15.8% increase in the radius suggests that about four PN molecules were encapsulated inside a single G4-PAMAM. The difference in the hosting capacity from the tris-dendrimer at pH 7 despite of both having similar repeating units is two-fold, one, at pH 10 the G4-PAMAM is completely uncharged and hence would provide a steric hindrance to

the entrance of PN molecules due to crowding of surface groups, whereas at pH 7, the relatively open structure of the tris-dendrimer owing to the electrostatic repulsions between the partially charged hydroxyl surface groups allows for an easier entrance of the PN molecules; and two, the comparatively more hydrophobic core of the tris-dendrimer (diaminohexane) vs. that of G4-PAMAM (ethylenediamine) favors the partitioning of PN molecules into the dendrimer core.

Since hydrophobic interaction is not as specific as electrostatic interaction, the titration curve of the tris-PN complex is less smooth than that of tris-Cu(II), and tris-NO_3^-. The fluctuations in the absorbance post the saturation point (10 PN molecules to 1 tris-dendrimer, Figure 3-4c) further corroborate the nonspecific nature of PN partitioning within the dendrimer. The solubilization in the hydrophobic environment in the interior of the dendrimers is further augmented by the formation of charge-transfer complexes between the PN aromatics and the dendrimer tertiary amines (248).

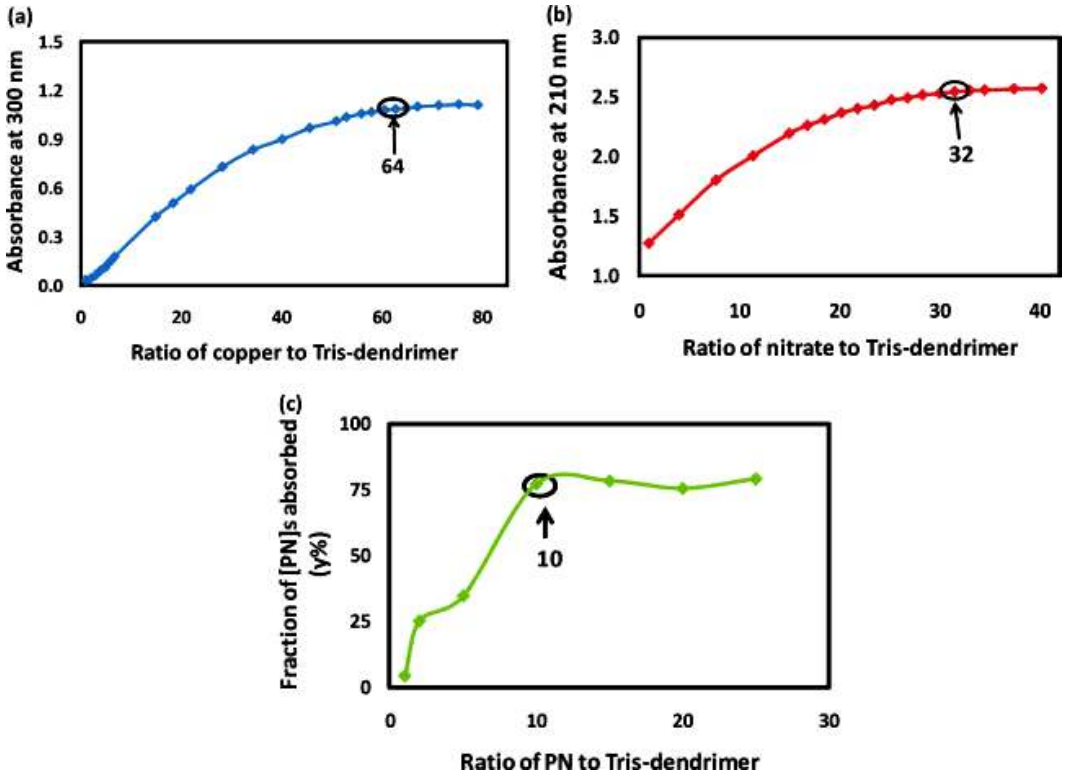

Figure 3-4. Spectrophotometric titration plots for (a) tris-Cu(II) at 300 nm, (b) tris-NO_3^- at 210 nm, and (c) tris-PN at 250 nm (260).

3.2.3. Regeneration of tris-dendrimer

Binding of chemical species to the tris-dendrimer is pH dependent. Hence by simply subjecting the complexes to elevated or reduced pH, one can regenerate the dendrimer. To investigate such a regeneration, the pH of the tris-chemical mixtures with the highest concentrations of chemicals absorbed were altered by titrating 1 M NaOH or 1 M HCl. The samples were then equilibrated for 30 min by constant mixing and their spectra recorded using a UV-vis spectrophotometer against the respective blanks.

We observed that on lowering the tris-Cu(II) solution pH to 2, the complex absorbance peak disappeared (Figure 3-2a). At low pH, H^+ competed with Cu^{2+} for tertiary

amine sites resulting in decomplexation of Cu^{2+}, and it was therefore possible to release Cu^{2+} from the dendrimer interior. Note there was a ligand exchange reaction from amines to the Cl^- (from the HCl added to lower the solution pH) and hence a formation of $CuCl_2$ was highly probable to limit hexadentate $Cu(H_20)_6^{2+}$ reformation.

A similar decomplexation can be observed for NO_3^- upon increasing the tris-NO_3^- solution pH to 10, as indicated by the similarity of the complex peak and the control tris-dendrimer peak at 210 nm (Figure 3-2b). This resulted in a hydrophobic dendrimer interior due to tertiary amine deprotonation and repulsion of the NO_3^- from the dendrimer interior. The change in the control NO_3^- peak with pH could be attributed to the excess of NaOH at high pH and HCl at low pH, each resulting in ion association with NO_3^- (278). It is well-known that the UV absorption spectrum of aqueous NO_3^- consists of two bands—a highly intense peak at approximately 200 nm and a much weaker peak at approximately 300 nm (279). However, because of the low concentration of NO_3^- used in our study, the peak at 300 nm was not observed.

By lowering the tris-PN solution pH to 2, the dendrimer interior became protonated, and the resulting decrease in the hydrophobicity of the dendrimer interior rejected the PN out of the dendrimer. This was indicated by a decrease in the complex peak and its resemblance to the control PN peak at low pH (Figure 3-2c). We have earlier reported (166) through adsorption-induced fluorescence resonance energy transfer (FRET) that an optimum energy transfer between PN and a labeled amine terminated G5-PAMAM dendrimer takes place around pH 8. MD simulations therein showed that at low pH, PN-PN interactions were energetically favorable as opposed to PN-dendrimer interactions at neutral pH. Further, at high pH, due to the contracting dendrimer size and surface crowding of

functional groups, as also noticed from our viscometry results above, PN molecules only adsorbed on the surface of the dendrimers and were prevented from partitioning into it. Atomistic MD simulations by Lin et al. (280) exhibited that buried water molecules, i.e. water molecules in the interior of the PAMAM dendrimers are thermodynamically unfavorable compared to that in the bulk water well outside the dendrimer at neutral pH. However, at low pH, the free energy of the buried water molecules becomes comparable to that in the bulk. This further corroborates our hypothesis that due to the increased hydrophilicity of the inter of the dendrimers at low pH, the hydrophobic PN molecules would be energetically unfavored inside the dendrimer and hence are released from the interior and interact with other PN molecules through π–π stacking.

Thus, tris-dendrimers could be efficiently regenerated by acid or base washing for all the three different types of chemical species.

3.3. A PAMAM Dendrimer for Mitigating Humic Foulant

3.3.1. Materials and characterization

Generation 5 amine-terminated PAMAM dendrimers (G5-NH_2, MW 28,826 g/mol) were purchased from Dendritech, Inc. in aqueous solutions and used as received. HA was obtained from Sigma Aldrich in powdered form and dissolved in deionized (DI) water to make a concentration of 500 mg/L. The HA solution was filtered using 0.2 μm syringe filters (Whatman) prior to all experiments. All experiments were performed at room temperature. The hydrodynamic size of the control HA and G5-PAMAM solutions were measured using dynamic light scattering in 1 mm path length plastic cuvettes (S90, Malvern

Instruments). The hydrodynamic sizes of the supernatants of the G5-HA complexes were also measured under identical conditions. Zeta potential measurements were conducted in disposable zeta potential plastic cuvettes using a Zetasizer (Nano ZS, Malvern Instruments).

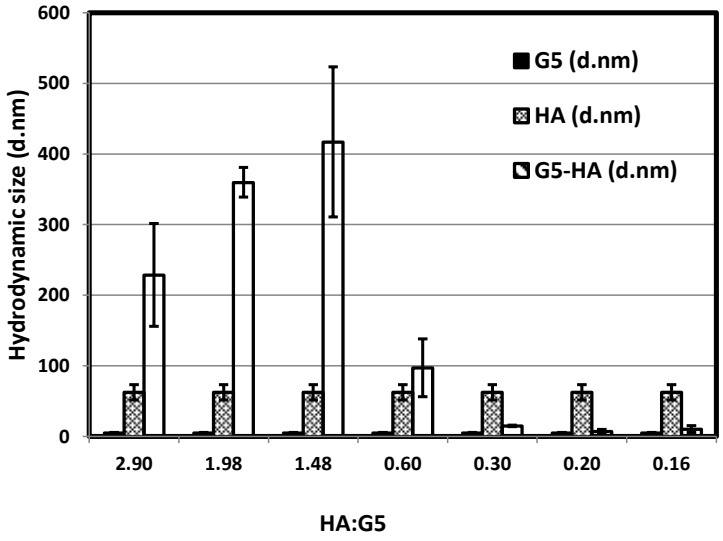

Figure 3-5. Hydrodynamic sizes of HA, G5-PAMAM and G5-HA complexes in the respective supernatants at different HA:G5-PAMAM ratios (353).

The hydrodynamic size of G5-NH_2 at a concentration between 42-450 mg/L ranged between 4.8-5.6 nm at pH 7 (Figure 3-5). At this pH value, only the primary amines of the dendrimers remain protonated while the interior of the dendrimers is hydrophobic. The HA at 75 -125 mg/L (the use of such high concentrations was to accommodate the instrument resolution for DLS, zeta potential and UV-vis measurements) and pH 5.5 showed a high inter-molecular association (d = 62.53 nm). Although the complex nature of HA prevents an

accurate characterization of its chemical composition, it is accepted (281) that carboxyl and phenol are the major functional groups, and HA at neutral pH is known to form clusters stabilized by the hydrophobic effect and intermolecular hydrogen bonds (282). Operationally, HA is defined as the component of humic substances which is insoluble at and below pH 2, due to protonation of the anionic groups (283). The zeta potential of HA at a pH of 5.5 was measured to be -34.5 mV due to the deprotonation of carboxyl functional groups.

3.3.2. Dendrimer-HA association constants

In a preliminary batch experiment, G5-NH_2 at pH 7.5 was added to a HA solution at pH 5.5 in an Eppendorf tube at several mass ratios to determine the optimum dendrimer concentration at which visual precipitation of the dendrimer-HA complex took place. The mixtures were mounted on a rotary shaker for 24 h and indeed an optimum ratio of HA to G5-PAMAM was observed at which flocculation of the complexes occurred. This suggests that an electrostatic interaction between the cationic dendrimers and the anionic HA led to the formation of strong complexes that cross-linked to form large precipitates. In order to further assess the binding affinity between the dendrimers and the HA, a fluorescence quenching method was developed for determining the equilibrium constants of the complex. HA solution was prepared by diluting from the stock in DI water and increasing concentrations of G5-PAMAM were added to the HA solution in a 1 mm path length quartz cuvette. After 30 sec of gentle shaking, the mixtures were allowed to incubate for 5 min and their fluorescent emission spectra between 400-600 nm were recorded for an excitation of 320 nm and Ex/Em slit widths of 10/20 nm on a Cary Eclipse fluorescence

spectrophotometer (Varian, Inc.). The emission spectra were corrected for their respective blanks (HA and dendrimers only). Measurements were recorded on three samples for statistical error analysis.

The phenol, amine, catechol, and quinone groups within humic substances give rise to strong fluorescence signals which are characteristic of the source of the humic substance. We observed that complexation with cationic dendrimers quenched the fluorescence of the HA. The fractional decrease in the fluorescence as a function of added dendrimers was examined using the Stern-Volmer equation:

$$\frac{F_0}{F} = 1 + K_{SV}[Q] \qquad (3\text{-}7)$$

Here, F_0 and F are the fluorescence intensities of HA in the absence and presence of the quencher (dendrimers), respectively, and $[Q]$ is the concentration of the quencher. K_{SV} is the Stern-Volmer constant. An HA solution was prepared by diluting the stock in DI water to reach 15 mg/L, the average concentration of humic substances found in natural ground and surface waters in the U.S. (284). Increasing concentrations of G5-PAMAM were added to the HA solution. The fluorescence of the HA was recorded between 400-600 nm upon excitation at 320 nm, showing a broad emission spectrum with a peak around 460 nm. Slight quenching of the HA fluorescence was observed upon dilution with DI water, resulting from charge transfer between the HA and dissolved oxygen in water (Figure 3-6 (a)) (285). Dendrimers, in contrast, exhibited negligible fluorescence in the range examined (Figure 3-6(b)).

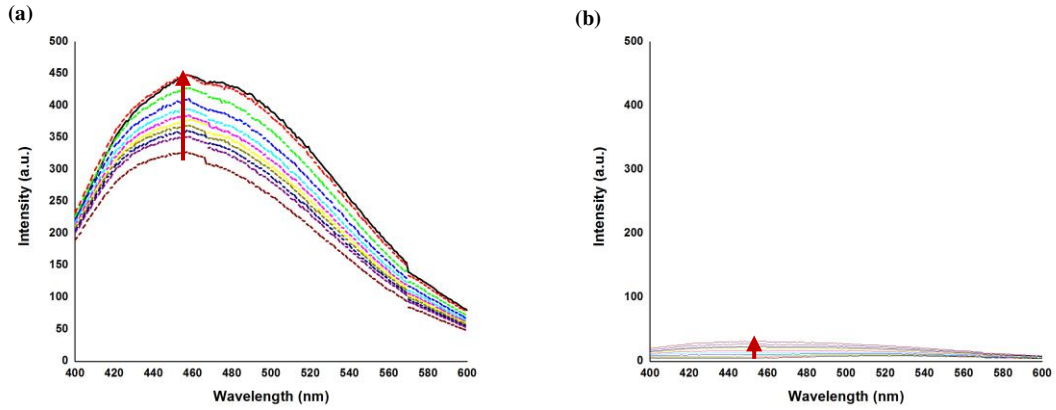

Figure 3-6. Fluorescence emission spectra of (a) HA and (b) G5-PAMAM at different concentrations. Arrow indicates direction of increasing concentrations (353).

However, a significant quenching was observed upon adding dendrimers to the HA solution (Figure 3-7 (a)). The Stern-Volmer plot derived from the fluorescence emission was linear (Figure 3-7 (b)), and the Stern-Volmer constant K_{SV} was determined to be 1.3×10^{7} M^{-1}. At a mass ratio of 5.25 mg of HA per mg of G5-PAMAM, corresponding to a G5-PAMAM concentration of 2.85 mg/L, the fluorescence intensity of the initial HA solution decreased by approximately 50%, implying that approximately half of the HA molecules were associated with the dendrimers. Linearity of the Stern-Volmer plot may imply either static or dynamic quenching. For dynamic quenching, the Stern-Volmer constant K_{SV} is equal to the bimolecular quenching constant k_q multiplied by the fluorescence lifetime in the absence of the quencher. The fluorescence lifetime of the commercial Aldrich HA is of the order of 0.6-8.4 ns (MW 3-50 kDa) at pH 6.3 (286). Therefore kq is determined to be $0.16\text{-}2.3\times10^{16}$ $M^{-1}s^{-1}$, much higher than the largest possible value for diffusion-controlled processes in aqueous solution (287). Hence, the quenching process here is concluded as a static process

arising from complex formation between G5-PAMAM and HA, primarily mediated by electrostatic interactions. Other interactions such as hydrogen bonding between the hydrogens of the dendrimer amines and the oxygens of the phenol and carboxyl groups of the HA are also feasible. The static Stern-Volmer constant, K_{SV}, can be interpreted as the ground-state association constant for the dendrimers and the HA, indicating a high affinity of HA for the G5-PAMAM dendrimers.

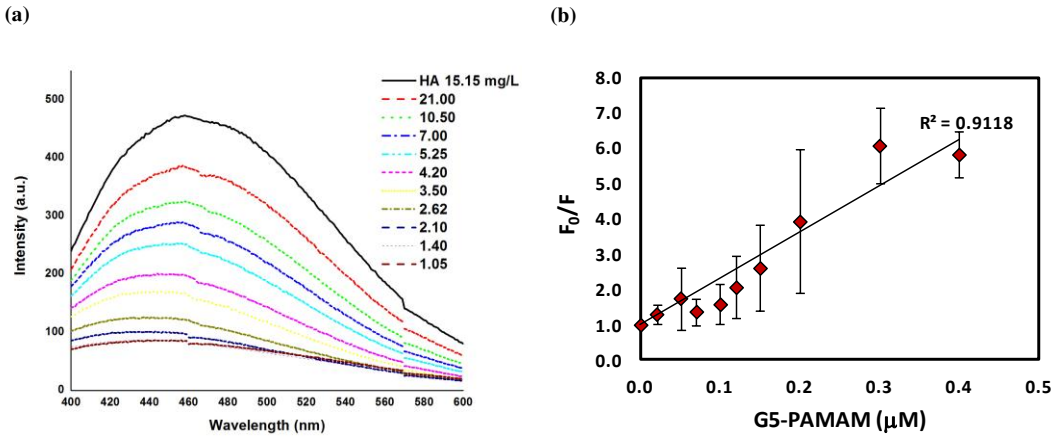

Figure 3-7. (a) Fluorescence emission of HA in the presence of decreasing amounts of HA per G5-PAMAM (g/g) = 21, 10.5, 7, 5.25, 4.2, 3.5, 2.62, 2.1, 1.4, and 1.05. (b) Stern-Volmer plot for G5-HA complexes. The linearity of the plot indicates static quenching due to the complex formation (353).

3.3.3. Efficiency of HA removal by PAMAM dendrimers

Given the high affinity of HA for dendrimers, it is of interest to assess the efficiency of the removal of dissolved HA in aqueous solutions by dendrimers. For this purpose, we carried out UV-vis absorbance measurement to quantify the amount of HA removed from the solution. HA has a broad absorption spectrum which decreases with increasing wavelength in an approximately exponential fashion, exhibiting no distinct bands. This

observed tailing in the HA absorption spectrum is attributed to the intramolecular charge-transfer between the hydroxyl-aromatic donors and quinoid acceptors formed by the partial oxidation of lignin precursors (288).

HA solutions of 75-125 mg/L were prepared by diluting the stock solution with DI water. The pH of the prepared HA solutions was 5.5. G5-PAMAM of gradient concentrations were then added to the HA solutions in 2 mL Eppendorf tubes. The final pH of the mixture was noted to be neutral. The mixtures were allowed to incubate on a rotor (Labquake, Barnstead) for 24 h, after which, visible precipitates were observed in the tube for optimal dendrimer concentrations (Figure 3-8 inset).

No visible precipitates were observed for the control HA, confirming strong interactions between the oppositely charged dendrimers and HA in the mixtures. The mixtures were centrifuged in a Minispin (Eppendorf) at the rate of 5,000 rpm (4,515g RCF) for 15 min and the absorbance of the supernatants was read on a UV-vis spectrophotometer (Biomate 3) in quartz cuvettes. The supernatants showed no new absorbance peaks, but were lower in intensity than the corresponding control HA samples for the entire range. The difference in intensities at 254 nm was then used to infer the fraction of HA left in the aqueous phase. Figure 3-8 shows the fraction of HA remaining in the aqueous phase vs. the ratio of HA to G5-PAMAM in solution. The fraction of remaining HA initially decreased followed by an increase with increasing dendrimer concentrations. Narkis and Rebhun (289) and Edzwald et al. (290) reported that cationic polyelectrolytes can destabilize high molecular weight polymers such as HA by charge neutralization. Such charge neutralization results in the formation of neutral species which can aggregate to form relatively large molecular weight compounds and precipitate out of the solution. The electrostatic

interaction between the cationic G5-PAMAM and the anionic HA led to the formation of complexes which cross-linked to form floc particles. The optimal concentration of G5-PAMAM at which maximum precipitation was observed was 50 mg/L, corresponding to ~2g HA per gram of G5-PAMAM added. Interestingly, this is also the stoichiometric ratio at which complete fluorescence quenching of HA of 15 mg/L occurred (Figure 3-7 (a)) (353). At this concentration, only 10% of the HA remained in the aqueous phase. This removal efficiency is twice as good as previously reported by Glaser and Edzwald (291), where 20% HA remained in the aqueous phase when the mass ratio of HA to branched polyethyleneimine (PEI) was ~1.25. In addition, compared to branched PEI, PAMAM dendrimers have a well-defined number of surface functionalities and hence a uniform surface charge distribution. In our experiment, a pseudo-exponential increase in the remaining fraction was observed for dendrimer concentrations above the optimal concentration (i.e., data points < 2.0 g/g in Figure 3-8). This can be explained as follows.

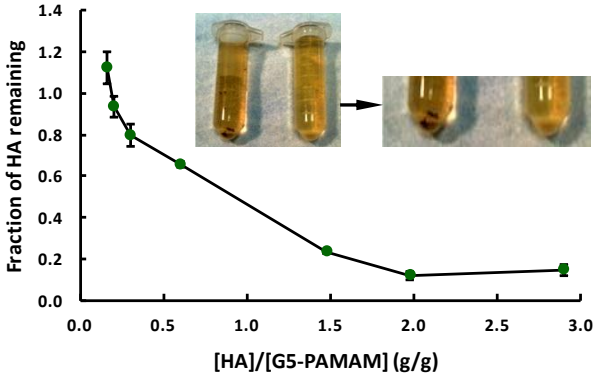

Figure 3-8. Fraction of HA remaining in solution vs. ratio of HA per G5-PAMAM added. Insets: Images of G5-HA precipitates in the left tube and HA alone in the right tube for the same HA concentration corresponding to 2g HA per gram of G5-PAMAM (353).

Initially, flocculation of the dendrimer-HA complexes was rapid due to the presence of a large number of sub-micrometer anionic HA particles and cationic dendrimers (Scheme 3-1, I). As the complexes started to aggregate through cross-linking, mediated by hydrophobic interactions, the number of charged particles/complexes decreased (Scheme 3-1, II). Once the charge neutralization is achieved at the optimal concentration of added dendrimers, further addition of the dendrimers re-stabilized the neutral hydrophobic flocs by providing steric and electrostatic repulsions between the formed complexes and hence increased absorbance of the HA (Scheme 3-1, III).

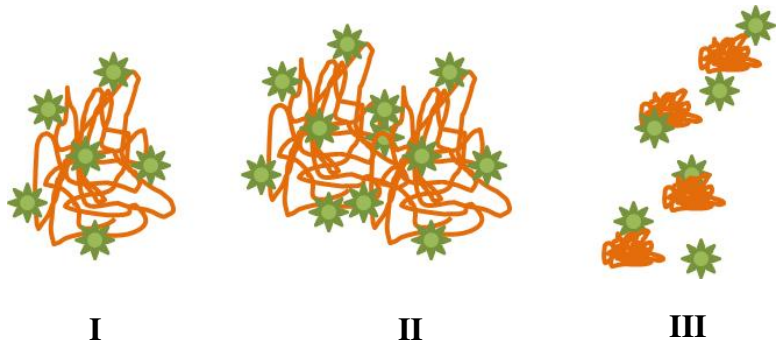

Scheme 3-1: Schematic of complexation (I), aggregation (II) and re-stabilization (III) processes in dendrimer-HA interactions. Dendrimers are shown in green and HA in orange (353).

Since G5-PAMAM dendrimers each possesses 128 surface amines, the optimal amount of the dendrimer amines is 224 μM (6.45 g/L) to neutralize a 100 mg/L HA solution. Potentiometric titrations (292) of the dissociation of Aldrich HA provide its total acidity to be 648 μM. This implies that ~2-3 HA molecules are neutralized by a single G5-PAMAM dendrimer. This is further confirmed by the DLS and zeta potential measurements

of the supernatants. Results from the DLS measurement showed formation of sub-micrometer sized soluble complexes at the optimal dendrimer dose (Figure 3-5). However, partial dissociations of the complexes occurred below and above the optimal dendrimer concentration. The zeta potential of the complexes shifted from negative (-18.3 mV) for dendrimers below the optimal concentration, to neutral (-2.24 mV) at the optimal concentration, and positive (+16.1 mV) for just above the optimal concentration. For higher doses, zeta potential measurements were unattainable due to the small sizes of the complexes (<3 nm) that were below the instrument resolution. This corroborates our hypothesis that further addition of dendrimers beyond the optimal concentration caused fragmentation of the large micron-sized aggregates into smaller complexes stabilized by cationic dendrimers (Scheme 3-1, III). Below the optimal concentration, all dendrimers were complexed with the HA and precipitation was observed. The negative zeta potentials under this condition were therefore indicative of the remaining HA in the solution. At the optimal concentration, hydrophobic interactions between the charge neutral complexes resulted in the formation of precipitates. Further absence of aggregation between the complexes may be attributed to steric effects and entropically driven release of encapsulated water and structural reorganization (293). Such entropic gain could compensate for the hydrophobic interactions between the complexes. Above the optimal concentration, excess dendrimers restabilized the neutralized complexes via electrostatic repulsions by interacting with them through hydrogen bonding (353).

3.3.4. Physico-chemistry of dendrimer-HA binding

To further investigate the specific chemical groups involved in the complex formation, attenuated total reflectance-Fourier transform infrared spectra (ATR-FTIR) were collected on the pellets obtained from experiments at the optimal dendrimer concentration described above. The precipitate shown in the Figure 3-8 inset was recovered by centrifugation, dried at 45°C, and then placed directly onto the ATR crystal for ATR-FTIR analysis. ATR-FTIR analyses were performed on a Thermo Nicolet 6700 FTIR with a single bounce diamond Smart iTR cell. Standard data collection parameters were 32 scans at 4 cm^{-1} resolution. A flux of nitrogen was passed through the instrument to remove $CO_2(g)$.

The chemical activity of HA is dominated by a high concentration of oxygen-containing functional groups, particularly carboxyl groups. Despite the complexity of HA molecules, IR spectroscopy is useful in resolving carboxyl groups due to their high polarizability and hence high IR activity. The chemical behavior of carboxyl groups also depends upon their structural environment, i.e. the types and orientations of other functional groups neighboring the carboxyls. A carboxyl group gives rise to two main features in the IR absorption spectra depending on its protonation state. The protonated carboxylic acids is characterized by absorption bands corresponding to a carbonyl stretch ($\nu_{C=O}$) between 1690 and 1750 cm^{-1}, and C-OH vibrations (ν_{C-OH}) between 1200 and 1300 cm^{-1}. Upon deprotonation, the vibrational mode of $\nu_{C=O}$ becomes coupled to that of the other deprotonated oxygen and its energy shifts to a lower energy level. This gives rise to an asymmetric stretching feature (ν_{as}) between 1540 and 1650 cm^{-1}. The C-OH band also shifts to higher energies upon deprotonation, giving rise to a symmetric COO^- mode (νs) between 1300 and 1420 cm^{-1}. The NH stretching vibrations occur near 3300-3500 cm^{-1}. Due to

hydrogen bonding in the solid state, these bands are broadened and are characteristic of amides (294).

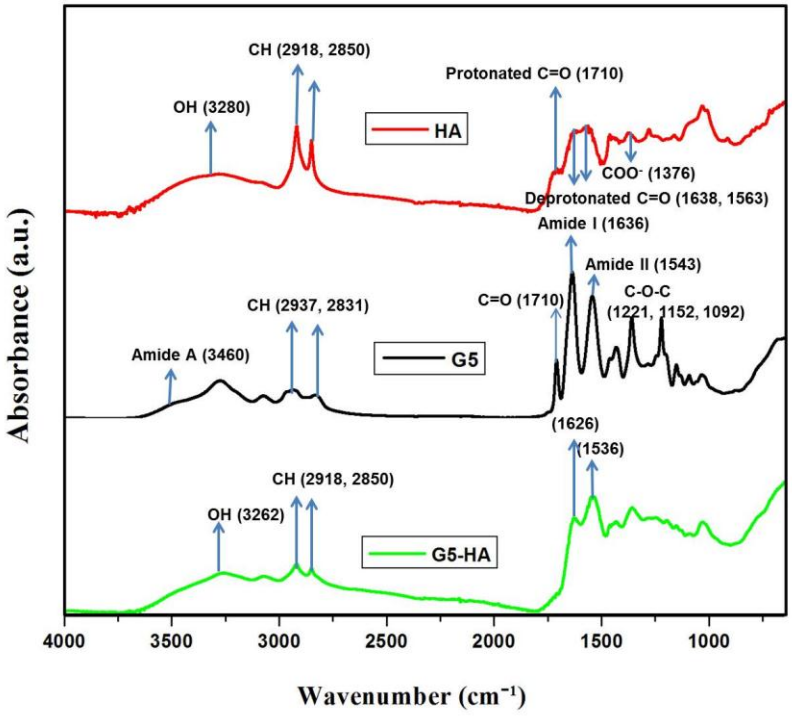

Figure 3-9. ATR-FTIR spectra of HA (red), G5-PAMAM (black) and G5-HA complex (green) (353).

As shown in Figure 3-9, the ATR-FTIR spectrum of the dendrimer-HA complex is a convolution of the spectra of the G5-PAMAM dendrimers and the HA, exhibiting several features suggestive of the interactive sites as follows (353).

1. The amide A band (3460 cm^{-1}) originating from a combination of amide II stretching and NH in-plane bending vibrations of the G5-PAMAM broadens to suggest hydrogen bonding with the deprotonated phenolic and/or carboxylic groups of the HA.

2. The amide II band at 1543 cm^{-1} of the G5-PAMAM and the 1563 cm^{-1} band of the HA that is associated with the N-H bending vibrations significantly downshifts to 1536 cm^{-1} for the G5-HA complex, suggesting direct, electrostatic interactions between carboxylic and amine functional groups of the HA and G5-PAMAM, respectively.
3. The asymmetric carbonyl stretch (1612 cm^{-1}) within the HA and the amide I peak (1636 cm^{-1}) within the G5-PAMAM are essentially combined within the G5-HA complex spectra. The apparent broadening of the spectral peaks within the G5-HA complex may be only due to the incorporation of the broad HA peaks. However, the minimal shift in peak positions of approximately 10 cm^{-1} could imply interactions with the dendrimer primary amines.
4. The disappearance of the C=O stretch at 1710 cm^{-1} in the G5-HA complex implies deprotonation of the carboxylic acid groups upon formation of the G5-HA complex. This indicates the presence of electron withdrawing groups, such as the dendrimer amines.

3.4. Discussions and Summary

In summary, with regard to dendrimer environmental applications we have demonstrated through UV-vis absobance measurements that tris-dendrimer can serve as a full-range host for the adsorption and dispersion of cationic, anionic, and PAH species. The tri-functionality of the tris-dendrimer could be advantageous owing to its higher surface charge density than the cationic or anionic monofunctional PAMAM dendrimers. The primary interactions governing the encapsulation of the species by tris-dendrimer were Lewis acid-base interactions and complexation with cationic Cu(II), electrostatic and hydrogen

bonding interactions with anionic NO_3^-, and hydrophobic interactions with PAH PN. The encapsulation of the species could also be reversed by changing solution pH. We have further demonstrated through UV-vis spectrophotometry efficient removal of dissolved HA using biocompatible PAMAM dendrimers. In addition to complex formation due to electrostatic interactions between the cationic dendrimers and the anionic HA at neutral pH as evidenced by our fluorescence quenching studies, our ATR-FTIR study has further identified the specific chemical groups involved in the dendrimer-HA complexation. Once charge neutralization is reached at a stoichiometric ratio of ~2 g/g for HA:G5-PAMAM, subsequent fast aggregation occurred resulting from hydrogen bonding and hydrophobic interactions between the neutralized complexes, leading to precipitation of the micron-sized aggregates. However, loading of additional dendrimers re-stabilized and resuspended the aggregates via electrostatic repulsion.

Thus, PAMAM dendrimers provide a more thermodynamically spontaneous adsorption process towards various chemical species, in contrast to conventional water purification procedures such as RO which require energy to drive the process to completion.

CHAPTER FOUR

ENVIRONMENTAL APPLICATIONS OF NANOMATERIALS

II. An Enhanced Detection of Pollutants Using Dendrimers

In chapter four, a new physical scheme is presented for the detection of copper, based on the use of a fluorescently labeled dendrimer anchored on a gold nanowire. Upon light illumination surface plasmon resonance was generated from the gold nanowire, which promoted quenching of the labeled dendrimer fluorescence as a result of the energy transfer between the dye on the dendrimer and the copper ions. The monotonic dependence of the fluorescence quenching on copper concentration was exploited to reach a copper detection sensitivity of 2 nM. In addition, the fluorescence of the labeled dendrimers was quenched specifically by copper in a matrix of common metal ions (295).

4.1. Introduction

Detection of metal ions in aqueous solutions is important for environmental protection and the sensitivity as well as selectivity of such detection is a challenge in a matrix of metal ions present in the environment. The detection of copper has both biological and environmental implications, and has been an active area of research in the recent decades. Copper is physiologically essential for bone formation, cellular respiration, and connective tissue development, and excessive amounts of copper can result in eczema, kidney disease, and damage to the central nerve system (296). Copper is also one of the major transition metals that are under environmental surveillance. For example, the U.S- EPA has set the safe limit of copper in drinking water at 20 μM (297). Among the various techniques available,

atomic absorption spectroscopy and inductively coupled plasma mass spectroscopy are the most commonly used tools for copper detection (298). In addition, there have been continued developments of electrochemical and fluorescence methods for copper detection (299-307). Most of these methods are costly and require skilled handling. Furthermore, the detection limits of these methods are usually low.

Having discussed the unique physico-chemical properties of PAMAM dendrimers as high capacity, recyclable, nanoscale hosts for transition metal ions such as Cu(II) in chapter three, here we present a facile optical method for enhancing the detection of Cu(II). Such a scheme could be extended to most metal ions in aqueous solutions. The detection of Cu(II) adsorbed by a dendrimer nanosponge was enhanced via the surface plasmon resonance (SPR) of a gold nanowire (Au-NW) substrate for the dendrimer. Specifically, upon light excitation the fluorescence of labeled Cu-adsorbed dendrimers anchored on an Au-NW substrate is quenched to a fuller extent (Figure 4-1, scheme). Based on the specific and selective response of dendrimers to Cu(II), an optical scheme well capable of the nanomolar copper detection has been developed.

4.2. Materials

G4 poly(amido-amine) PAMAM dendrimers (G4-Sac) with a 1,4-diaminobutane core and 64 succinamic acid surface groups (MW: 20,647, 10 wt % in H_2O) were purchased from Sigma Aldrich and used as received. Carboxylic reactive fluorescent Alexa Fluor® hydrazide bis(triethylammonium salt) 633 dye with a maximum absorption at 624 nm and emission at 666 nm was obtained from Molecular Probes and dissolved in Milli-Q prior to use. Copper(II) nitrate hydrate ($Cu(NO_3)_2 \cdot xH_2O$, MW: 188), chromium(III) chloride hexahydrate

($CrCl_3 \cdot 6H_2O$, MW: 266.45), manganese(II) chloride hydrate ($MnCl_2 \cdot xH_2O$, MW: 125.84), lead(II) chloride ($PbCl_2$), MW: 278.11), and mercury(II) chloride ($HgCl_2$), MW: 271.50) were purchased from Sigma Aldrich and dissolved in Milli-Q prior to use. Cationic cetyltrimethylammonium-bromide (CTAB)-coated Au-NWs (30 nm in diameter, 6 μm in length, stock concentration: 50 μg/mL in H_2O) were purchased from Sigma Aldrich and used as received.

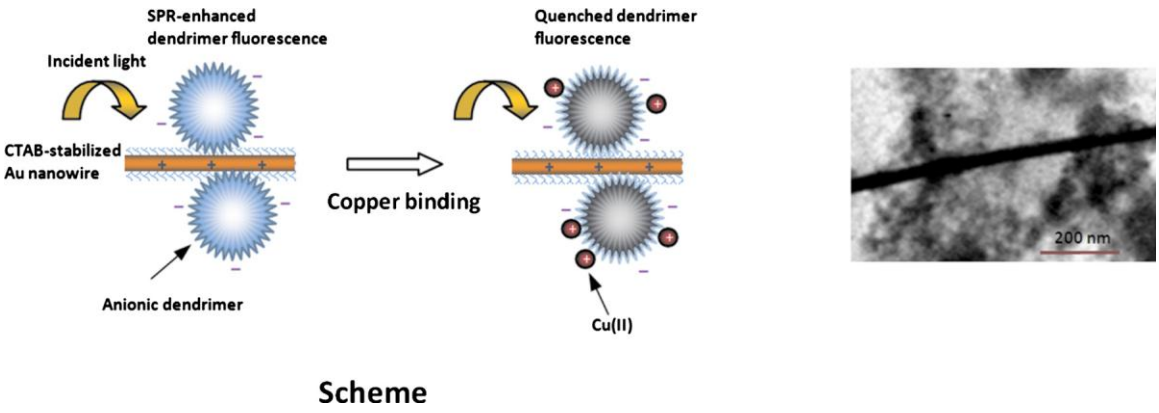

Figure 4-1. (Left) Experimental scheme showing detection of Cu(II) using G4-Sac dendrimers and Au-NW-induced SPR. (Right) TEM image showing the adsorption of G4-Sac dendrimers (in gray and black) onto a single Au-NW. A total volume of 1 mL of Au-NW-G4-Sac mixed with 2 mM Cu(II) was pipetted onto a 200 mesh carbon coated copper grid (Ted Pella) and incubated for 1 h prior to imaging. Images were acquired on a Hitachi H7600 operated at 80 kV (295).

4.3. Characterization of Dendrimer-Cu(II) Binding

Measurements of Cu(II) binding to G4-Sac PAMAM dendrimers in aqueous solutions were carried out using a UV-vis spectrophotometer (Biomate 3). A dendrimer pH of 9–9.5 was adjusted by the addition of 1 M HCl or NaOH and used for all experiments.

This optimum pH value was adopted from a previous work (169). The binding capacity of the anionic dendrimers was determined through titration of Cu(II) at a Cu(II)-G4-Sac volume ratio of 1:1. The G4-Sac concentration was maintained at 10 μM while the Cu(II) concentration was lowered from 0.25 mM to 1 μM. Our experimental procedure consisted of mixing and equilibrating the aqueous solutions of Cu(II) and G4-Sac at room temperature for 30 min. A survey scan of the absorbance of control G4-Sac, Cu(II), and the mixture of Cu(II) and G4-Sac was carried out in the wavelength range of 250–350 nm, where Cu(II) was found to show strong absorbance.

Figure 4-2 shows a plot of the absorbance of Cu(II)-G4-Sac complex for different concentrations of Cu(II). At pH 9, the fraction of tertiary amine groups of the G4-Sac that remained charged was 0.003 and that of terminal carboxyl groups was 0.91 (169). The dendrimer structure was therefore enclosed as a result of this low charge density within its interior. Hence, at pH 9 Cu(II) binding occurred primarily with the negatively charged deprotonated carboxyl terminal groups. Coordination of Cu(II) with the nitrogen atoms in the tertiary amine groups was also feasible (308).

As shown in Figure 4-2, Cu(II)-G4-Sac absorbed in the range of 250–350 nm with a broad peak occurring around 300 nm. This broad peak was attributed to a strong ligand-to-metal charge transfer between the G4-Sac and the Cu(II) (273). For the concentrations used, both the control dendrimer and Cu(II) showed negligible absorbance in this wavelength range (data not shown). However, the absorbance of the Cu(II)-G4-Sac complex was detectable until the Cu(II) concentration was reduced down to 10 μM. Below 10 μM, the

peak flattened and Cu(II) was no longer detectable. Hence, 10 μM was regarded as the detection limit of Cu(II) by the UV-vis spectrophotometer.

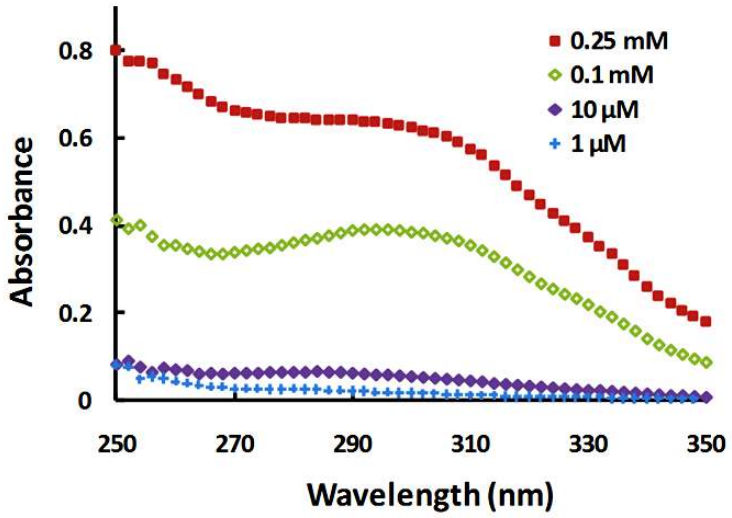

Figure 4-2. Absorbance of the Cu(II)-G4-Sac complex, where Cu(II) becomes undetectable below 10 μM (295).

4.4. Enhancing the Limit of Cu(II) Detection by Dendrimers

For the fluorescence measurements, the G4-Sac dendrimers were labeled with Alexa Fluor 633 dye at an optimized molar ratio of G4-Sac:dye=1:10. The dendrimer-dye mixture was covered in aluminum foil and shaken for 3 h at 4°C. Dialysis was performed to remove free dyes using a 10,000 MWCO Spectra/Por RC Float-A-Lyzer membrane (Spectrum Laboratories). The molecular cutoff of the membrane enabled unlabeled dyes (MW 1,150 Da) to exit and the dye-dendrimer conjugates (MW larger than 20,647 Da) to be retained.

After washing the membrane to remove its preservative, the dendrimer-dye mixture was injected into the membrane and secured with a cap. The membrane was suspended in Milli-Q in a 2 L beaker while continuously being stirred on a magnetic mixer for 24 h. The mixture was then removed from the membrane, covered in foil, and kept at 4°C for use. According to the labeling protocol, it was estimated that approximately one fourth to one third of the dyes would conjugate to the primary and/or tertiary amines of the dendrimers, which would yield a labeling molar ratio of G4-Sac:dye at 1:2 to 1:3. The pH of the labeled dendrimer solution was adjusted to 9.5 for all measurements.

Approximately 500 μL of 25 μM Au-NW solution was mixed and incubated with 500 μL of 48 μM G4-Sac for 30 min to measure the change in zeta potential (NanoZS, Malvern Instruments) of Au-NWs induced by their binding with anionic dendrimers. The zeta potential of the CTAB-coated Au-NWs (+52.1±11.6 mV) decreased sharply to a stable negative value (−57.5±4.27 mV) after mixing the NWs with G4-Sac dendrimers for 30 min. It is therefore inferred from this measurement that G4-Sac dendrimers adsorbed efficiently onto the Au-NWs and their complexes remained stable in the aqueous solutions. Then, 40 μL of 0.12 mM Au-NW solution was incubated with 100 μL of the labeled dendrimers (2 μM) for 30 min in a standard black 96-well flat-bottomed plate. Cu(II) was added in gradually decreasing concentrations to the Au-dendrimer mixture from 20 μM to 2 nM and each mixture was incubated for 30 min. Fluorescence intensities were recorded (Cary Eclipse fluorescence spectrophotometer, Varian Inc.) for the control labeled dendrimers, Cu(II)-dendrimers, Au-dendrimers, and Au-dendrimer-Cu(II) at an excitation wavelength of 580 nm and emission wavelength ranging between 600–900 nm. Each sample was measured

three times to establish error bars. The response time of Cu(II) binding with G4-Sac was established by measuring the time evolution of the FRET efficiency using Equation 4-1 as follows:

$$|(I_F - I_{F0})/I_{F0}|\% \qquad (4\text{-}1)$$

where I_F and I_{F0} are the fluorescence intensities of the G4-Sac in the presence and absence of Cu(II), respectively. The concentration of Cu(II) used was 20 μM.

Transition metals like Cu(II) form complexes with water to give strong *d-d* electronic transitions throughout the near ultraviolet, visible, and near-infrared regions of the spectrum. Figure 4-3 shows the aqueous absorption spectrum of Cu(II) and the fluorescence emission spectrum of the Alexa Fluor 633 dye between 600–900 nm. Due to the overlap between the two spectra, Cu(II) quenched the fluorescence of the dye as a result of the occurrence of FRET. Furthermore, when Cu(II) was bound to a G4-Sac dendrimer, a weak charge transfer from the dendrimer to the Cu(II) could have also contributed to the quenching process. Hence, a significant decrease was registered for the fluorescence intensity of the Cu(II)-G4-Sac complex, compared with the control labeled dendrimer (Figure 4-3 (b)). Figure 4-3 (b) shows the fluorescence spectra of the control labeled G4-Sac, control Au-G4-Sac, Cu(II)-labeled G4-Sac complex, and Au-G4-Sac-Cu(II) complex. The spectra of the complexes can be clearly distinguished from the controls.

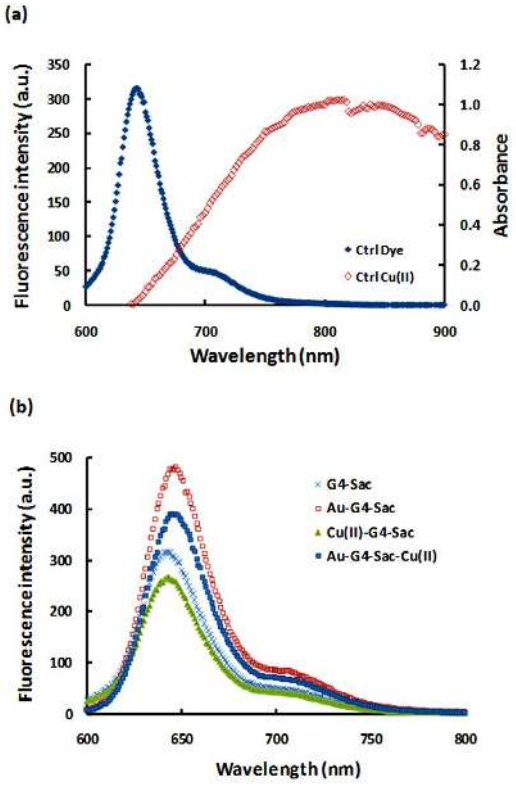

Figure 4-3. (a) Fluorescence emission spectrum of Alexa Fluor 633 dye (vertical axis, left, solid diamonds) and absorbance of Cu(II) (vertical axis, right, hollow diamonds) in aqueous solution. (b) Fluorescence emission spectra of labeled G4-Sac, Au-G4-Sac complex, Cu(II)-G4-Sac complex, and Au-G4-Sac-Cu(II) complex. The Cu(II) concentration is 20 μM for all samples. Note a spectral shift of 3–5 nm in the presence of Au-NWs (hollow and solid squares), indicating the occurrence of SPR (295).

Specifically, the labeled dendrimers displayed a strong absorbance peak at 645 nm when excited at 580 nm (crossed curve). In aqueous solutions, Au-NWs under illumination are assumed to exhibit strong plasmon and longitudinal bands. The strong interaction with light occurs because the conduction electrons on the metal surface undergo a collective oscillation when excited by light at specific wavelengths. This phenomenon is known as SPR and this oscillation results in unusually strong scattering and absorption properties. Shifts in the SPR peak wavelength can be obtained by changing the local refractive index near the

particle surface. When dendrimers were adsorbed onto an Au-NW via electrostatic interaction, a spectral shift of 3–5 nm was induced in the dendrimer fluorescence (hollow squared curve versus crossed curve). This spectral shift suggests the occurrence of a charge transfer between the dendrimer and the Au-NW, conceivably associated with a conformational change in the dendrimer. The observed redshift can also be attributed to the lowered vibration frequency of the dyes labeling the dendrimer, due to their mutual aggregation promoted by the Au-NWs. In addition to the spectral shift a significant increase in fluorescence intensity was also detectable for the Au-G4-Sac sample, likely resulting from the SPR of the Au-NWs (hollow squared curve). Fluorescence enhancement by gold nanostructures is a well-established phenomenon (309). In our current scheme the SPR enhancement of dendrimer fluorescence by an Au-NW was exploited to improve the detection of Cu(II).

As shown in Figure 4-4, fluorescence quenching was observed when the Cu(II) concentrations were 20 μM and 2 μM (vertical bars for "without Au-NWs"), where the molar ratio of G4-Sac:Cu(II) was less than 1. However, when the Cu(II) concentrations were below 2 μM, or the molar ratios of G4-Sac:Cu(II) were greater than 1, Cu(II) enhanced the fluorescence of the labeled dendrimers (data not shown). Such metal-enhanced fluorescence (MEF) has been observed before (310) for Cu(II)-dye interaction and is understood as distance dependent. For example, low concentrations of the Cu(II) ions could result in formation of Cu(II) nanoclusters, while high concentrations of the Cu(II) ions could form continuous thick film like aggregation with G4-Sac dendrimers through their mutual

coordination. In the former case the fluorescence of labeled G4-Sac dendrimers could be

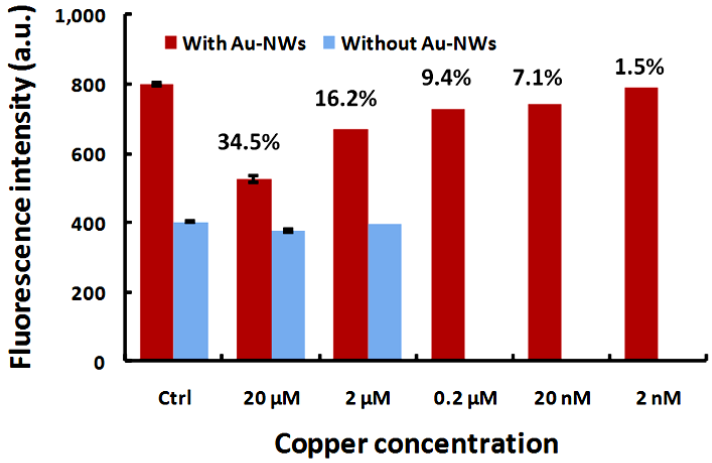

Figure 4-4. Average fluorescence emission intensity of G4-Sac- Cu(II) complexes with (red bars) and without (blue bars) Au-NWs (295).

enhanced by the plasmons coupled from the Cu(II) nanoclusters. In other words, a mirror electric dipole could first be induced in the metal by the fluorophore and the surface plasmons associated with the metal could in turn be efficiently coupled back to excite the fluorophore. Since the scattering capability of Cu(II) responsible for the MEF effect is relatively weak (311), the differences in fluorescence enhancement were unremarkable for Cu(II) ranging between 0.2 µM to 2 nM. In contrast, the fluorescence of dendrimers conjugated with Au-NWs was quenched for Cu(II) of 20 µM to 2 nM. This quenching was induced by the Cu(II) ions bound to the dyes of the dendrimers that were adsorbed onto the Au-NWs. The absorption cross-section of Cu (σ_{Cu}=5.80 at 520 nm) is much larger than that of Au (σ_{Au}=1.86 at 520 nm) (310), while the MEF of Cu is less pronounced compared to

Au. The enhanced fluorescence due to the SPR scattering by the Au-NWs favored the optical absorption of Cu(II) and, hence, quenching was observed for Cu(II) even at a concentration of 2 nM. Also indicated in Figure 4-4 are the percents of fluorescence quenching observed with decreasing Cu(II) concentrations, calculated as:

$$[(Io - I)/Io]\% \qquad (4\text{-}2)$$

where I_0 is the intensity of the control with Au-NWs, and I is the intensity of the Au-G4-Sac-Cu(II) complexes. We therefore conclude that the detection limit for Cu(II) by our experimental scheme is 2 nM, equaling or exceeding the performance of most copper detection techniques reported in the recent literature (299-307).

4.5. Evaluating the Selectivity of Dendrimers towards Cu(II)

To investigate the cation selectivity of G4-Sac toward copper Cu(II), other environmentally metal ions of chromium, manganese, lead, and mercury were used. Solutions of the metal ions mixed with G4-Sac, in the absence or presence of Cu(II), were prepared with a final concentration of 20 μM of each metal ion and equilibrated for 30 min prior to measurements. The emission spectra were recorded in the wavelength range of 625–665 nm upon excitation at 580 nm. Each curve was averaged over three measurements.

In the solution containing the transition metal ions in the absence of Cu(II) (Figure 4-5), no significant quenching of the G4-Sac fluorescence was observed (dashed versus solid curve). However, after Cu(II) was included in the metal matrix, the fluorescence intensity of the labeled G4-Sac was quenched by a maximum 4.8% at 642 nm (dotted curve). The dendrimer used in our experiment had succinamic acid surface groups which offered typical carboxylic acid reactivity. Although the anionic surface groups of the dendrimer are expected

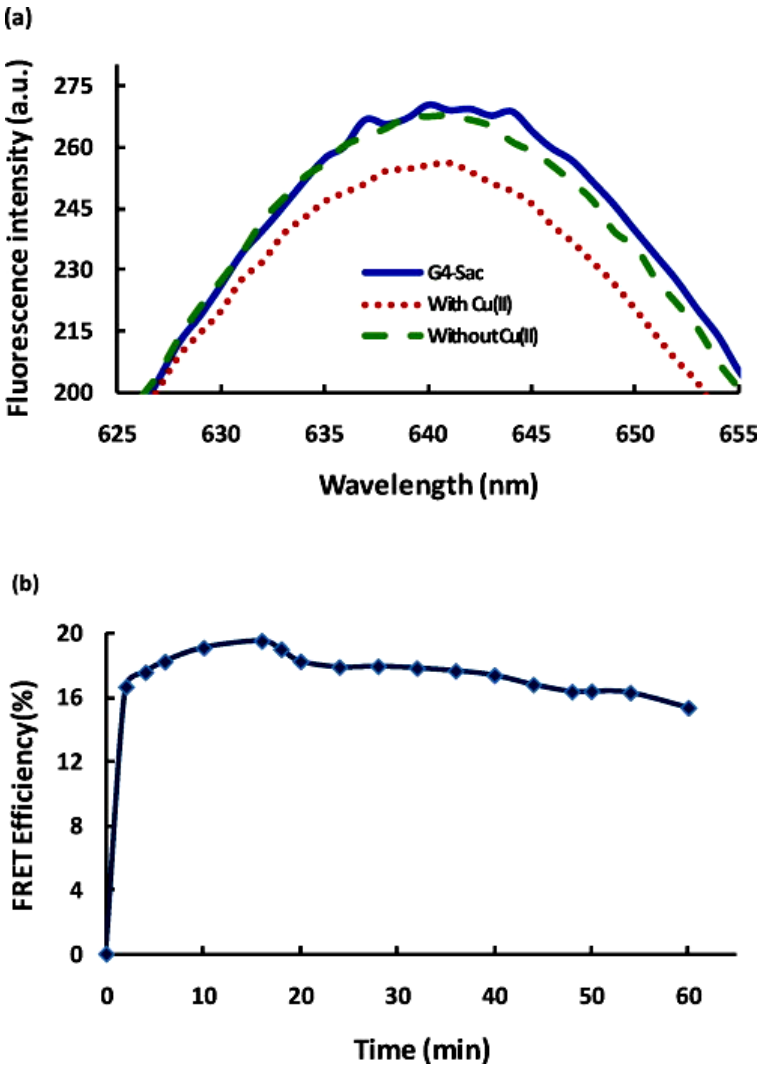

Figure 4-5. (a) Selectivity of G4-Sac toward Cu(II). Solid curve–control labeled G4-Sac; dashed curve—labeled G4-Sac and metal matrix containing Cr(III), Mn(II), Pb(II), and Hg(II); dotted curve—labeled G4-Sac, metal matrix, and Cu(II). The concentrations of each metal ion was 20 μM. (b) Time evolution of FRET efficiency between labeled G4-Sac and Cu(II) (295).

to bind with all the metal ions in solution (273), it is well known that Cu(II) has a higher propensity compared to other metal ions in binding with carboxylates (312). In addition, Cu(II) quenches more efficiently than other metal ions due to its strong paramagnetic properties (301, 313). Nevertheless, the observed small percent of fluorescence quenching by

Cu(II) in Figure 4-5 (a) further emphasizes the significance of our scheme of utilizing the SPR of Au-NWs. Also shown in Figure 4-5 (b) is the time evolution of the FRET efficiency between labeled G4-Sac and Cu(II). A maximum efficiency of 19.5% was observed 15 min after the Cu(II) was added to the dendrimer solution, indicating occurrence of maximum interaction between the Cu(II) and the dendrimer. The subsequential reduction in the FRET efficiency could be due to the increased interaction between the G4-Sac-Cu(II) complexes, which would hinder the loading of copper onto the dendrimer.

4.6. Discussions and Summary

In summary, a new scheme has been devised for the selective and sensitive detection of Cu(II). This method combines the advantages of established dendrimer physical chemistry with the field enhancing effect of Au-NWs under light illumination. Using this assembly of dendrimer-Au-NW we have successfully detected Cu(II) down to the concentration of 2 nM (295). This sensitivity is comparable with the sensing schemes based on silver and gold nanoclusters (312, 314), and is advantageous due to the facile design of our approach. The detection limit of our scheme could be substantially improved in principle by optimizing the polarization direction of the illumination light, diameter of the Au-NWs, generation/size of the dendrimers, pH and temperature of the solvent, or by integrating with nanoelectronic devices such as NW-field effect transistors or nanofluidics. Further, the specificity of the detection scheme can be enhanced by maximizing the spectral overlap between the dendrimer label and the metal ions under study, or combining the current technique with analytical tools such as NMR and Raman spectroscopy.

CHAPTER FIVE

ENVIRONMENTAL APPLICATIONS OF NANOMATERIALS

III. Dendritic Nanotechnology for Remediating Discharged Nanoparticles

Chapter five focuses on the use of dendritic nanotechnology and molecular self-assembly for capturing potentially harmful discharged nanoparticles in the aqueous environment. Here we show that PAMAM dendrimers of both generations 1 (G1) and 4 (G4) can host 1 fullerenol per 2 dendrimer primary amines as evidenced by isothermal titration calorimetry (ITC), DLS and spectrofluorometry (354). Thermodynamically, the interactions were similarly spontaneous between both generations of dendrimers and fullerenols, however, G4 formed stronger complexes with fullerenols resulting from their higher surface charge density and more internal voids, as demonstrated by spectrofluorometry. In addition to hydrogen bonding that existed between the dendrimer primary amines and the fullerenol oxygens, hydrophobic and electrostatic interactions also contributed to complex formation and dynamics. Such hybrid of soft and condensed nanoassembly may have implications for environmental remediation of discharged nanomaterials and entail new applications in drug delivery.

5.1. Introduction

Nanoscale assembly is an area of active research that has great implications for molecular design, biological sensing, environmental remediation, nanofabrication, supramolecular chemistry, energy, and catalysis (315, 316). Within the pH range of 7-10, PAMAM dendrimers bind to ions through multiple mechanisms, including Lewis acid-base complexation with their primary and tertiary amines serving as donors, ion-pairing with

charged terminal groups, and non-specific interactions that result from the physical encapsulation of ions in interior cavities which may involve interactions with trapped counterions or water molecules (170, 242, 295, 317). Generally, lower-generation dendrimers bind to guest molecules or ions more effectively due to their more accessible interior which offers decreased mass transfer resistance and facilitates more guest-host collisions than their higher generation counterparts (317). Importantly, dendrimers can also reversibly release contaminant loads through changes in the solvent pH and electrolyte strength, or via a UV trigger. For example, using PAMAM and PPI dendrimers Diallo et al. (170, 242) selectively removed Cu(II) and perchlorate (ClO_4^-) from water. Once dendrimer-Cu(II) or dendrimer-ClO_4^- complexes were formed, they were eliminated from aqueous solutions by UF. Regeneration of the dendrimers, at 90% or above, was realized when the solution pH was lowered to 4 to release Cu(II) and raised to 9 to unload ClO_4^-. The primary mechanism behind the regeneration was attributed to the pK_a values of the primary (~7) and tertiary (~4) amine groups of the PAMAM dendrimers (318). Protonation of the tertiary amines at pH 4 coordinating with the Cu(II) resulted in electrostatic repulsions, whereas deprotonation of the primary amines at pH 9 reduced the attractions between the ClO_4^- and the deprotonated amines. Recently, there has been increased interest in dendrimer host-guest supramolecular assembly (319). Indeed molecular dynamics simulations have shown that protonation of the dendrimer amines favor intermolecular hydrogen bonding with guest species, in addition to other non-covalent intermolecular forces such as ionic bonding, polar and van der Waal's forces(320).

In addition to environmental and industrial applications, dendrimers can bind either covalently or noncovalently with small and macro-biomolecules as well as metal ions, and act

as transporters for the delivery of genes, drugs, prodrugs, MRI contrast agents, and viral inhibitors (171, 239, 321). The feasibility of such applications is established upon the understanding that PAMAM dendrimers interact readily with phospholipids and show high permeability through cell membranes (321-325), thereby rendering them non-viral transporters with high efficacy (324). The biocompatibility of dendrimers has been a topic of concern, but toxicities were reported for PAMAM dendrimers of generations seven and larger, and only minimally (326). Additionally, such toxicity can be reduced by neutralizing the surface charge of the dendrimer or converting the surface charge to anionic (172).

In contrast to the "soft" polymeric dendrimers, fullerenes and their derivatives are carbon-based, single-molecular particulates that possess appealing mechanical, thermal, electrical, physicochemical, and redox properties; the last two aspects endowed them a name of "nanopharmaceuticals" (327). Consequently, fullerenes and their derivatives are building blocks for designing nanoscaled assemblies for promising physical, biological, and medicinal applications. For example, photovoltaic devices made of polymer-fullerene derivatives -- where the polymer acts as the electron donor and the fullerene as the electron acceptor – have been studied and commercialized (328-331). Conjugation of murine anti-gp240 melanoma antibody to fullerene C_{60} with cross-linker N-succinimidyl-3-(2-pyridyldithio)propionate (SPDP), has been shown to preserve the drug potency and facilitate the development of fullerene immunotherapy (332).

Hydrophobic fullerenes C_{60} and C_{70} show a propensity for the amphiphilic lipid bilayer and can potentially impact cellular processes including electron transport in the photosystems of plant species. Water-soluble fullerene derivatives $C_{60}(OH)_x$ -- or fullerenols -- have been found effective in suppressing ROS and the toxicity of copper, and have been

employed as glutamate receptor antagonists and antiproliferative, neuroprotective or anticancer agents (331, 333). Along with these biological and medicinal applications, the fate of fullerenes and their derivatives in living systems has become a topic of much research effort, especially over the past decade (32, 334-336). Using *in vitro* and *in silico* studies Sayes et al. (337-341) and Qiao et al. (338) delineated the differential cytotoxicities of pristine and functionalized fullerenes, and attributed such contrasting cell responses to lipid peroxidation, hydrophobicity, and distribution of potential of mean force associated with the nanoparticles in a lipid bilayer. Others (339) and our group (342) showed that fullerenol could inhibit polymerase chain reaction and microtubule polymerization *in vitro*. Specifically, the surface hydroxyls of fullerenol $C_{60}(OH)_{20}$ complexed with the triphosphate oxygens of nucleotides and nucleic acids and with the alpha helices and the junctions of tubulin dimers through hydrogen bonding (H-bonding), as well as hydrophobic and electrostatic interactions. In addition, water-soluble $C_{60}(OH)_{20}$ compromised plasma membranes to induce necrosis in *Allium cepa* cells, driven by concentration gradient of the NPs across the hydrophobic plant cell wall (343, 344).

In view of the promises of fullerenes and dendrimers for nanomedicine, and in view of the crucial need for developing new strategies for mitigating the potential adverse effects of environmental discharge of nanomaterials, here we show a novel self-assembly of PAMAM dendrimers and fullerenols and elucidate the underlying physical chemistry and thermodynamics for such assembly. Both generations 1 and 4 (i.e., G1 and G4) dendrimers have been employed to take advantage of their versatile morphology, charge density (8 and 64 primary amines per G1 and G4 dendrimer, respectively), and radius of gyration. In addition to providing a fundamental basis for dendrimer environmental applications and

drug delivery, this study also serves as a proof-of-concept that nanomaterial discharge -- an emerging environmental concern – may be remedied by alternative nanotechnologies.

5.2. Materials

Amine terminated PAMAM dendrimers with ethylenediamine cores of generations 1 (MW 1430, 9.98 wt % in H_2O) and 4 (MW 14,215, 14.04 wt % in H_2O) (G1 and G4, respectively) were purchased as aqueous solutions from Dendritech, Inc. Polyhydroxy-C60 ($C_{60}(OH)_n$, fullerenol hereafter, n~18-22) was purchased from BuckyUSA. An average of 20 OH groups per fullerenol molecule was assumed for all measurements. All materials were used as received. The stock fullerenol suspension of 1 mM was prepared in deionized water by bath sonication for 30 min.

5.3. An Empirically Determined Ratio of Dendrimer-Fullerenol Assembly

The average hydrodynamic diameter, particle size distribution and polydispersity indices (PDI) of the dendrimer-fullerenol assemblies were measured using a Nanosizer (S90, Malvern Instruments). The pristine dendrimer and fullerenol aqueous solutions were filtered with Anotop filters (Whatman) of 20 nm pore size prior to the measurements. 19 injections of dendrimer solutions of 8 μL each were added to 1.46 mL of fullerenol suspension in a standard plastic macro-cuvette of path length 1 cm. The dendrimer-fullerenol mixtures were allowed to incubate for 5 min after each successive injection and 30 sec mixing prior to the measurements. The pH of the final mixture was 6.5. Three repeats were performed for statistical error analysis. Surface charges of the pristine dendrimer and fullerenol suspensions

and that of the dendrimer-fullerenol mixtures at different stoichiometric ratios were measured using a Zetasizer (NanoZS, Malvern Instruments).

As shown in Table 5-1, the hydrodynamic diameter of fullerenol averaged 4.4 ± 3.8 nm at 10 μM and 5.1 ± 5.1 nm at 100 μM, indicating the association of fullerenols as a result of hydrophobic and hydrophilic partitioning. The zeta potentials of both G1 and G4 dendrimers were positive due to their protonated primary amines at neutral pH (Table 5-1). Upon addition of G1 and G4 dendrimers to fullerenol solutions, however, the average hydrodynamic diameter of the dendrimer-fullerenol assembly increased immediately by an order of magnitude (Figure 5-1). Also, the stoichiometric ratio of greater than one fullerenol per primary amine suggested that their binding was more complex than ionic bonding, likely also involving H-bonding and hydrophobic interaction. For G1 dendrimer, saturation in the aggregate size was observed ranging between 710-955 nm, for a G1/fullerenol molar ratio of 0.27 (corresponding to 2.19 primary amines per fullerenol) or higher (Figure 5-1 (a)). For G4 dendrimer, uniform sized aggregates were formed until the ratio of dendrimer/fullerenol reached ~0.03 (corresponding to 2.14 primary amines/fullerenol, Figure 5-1 (b)). As more dendrimers were added to the suspensions, the fullerenols associated with one dendrimer started to interact with those bound to neighboring dendrimers to trigger the formation of dendrimer-fullerenol supramolecular complexes, likely mediated by H-bonding. Such inter-cluster interactions also occurred in the case of G1/fullerenol system. Interestingly, the number of primary amines/fullerenol at which inter-cluster aggregation occurred was ~2 for both G1 and G4 dendrimers. Whereas the sizes of the G1/fullerenol and G4/fullerenol complexes were comparable (1,000 – 1,300 nm) at a primary amine/fullerenol ratio of ~2,

precipitation occurred more rapidly for G4 dendrimers (Figure 5-1 (a-c)), implying a stronger G4/fullerenol association (354).

Table 5-1. Characterizations of fullerenols, PAMAM dendrimers and their assemblies (354).

Particle	Hydrodynamic size (nm)	Polydispersity index (PDI)	Zeta potential (mV)
$C_{60}OH_{20}$ (10 μM)	4.4 ± 3.8	1.00 ± 0.00	-21.8 ± 10.9
$C_{60}OH_{20}$ (100 μM)	5.1 ± 5.1	0.68 ± 0.22	-53.8 ± 10.5
G1-NH_2 (200 μM)	2.5 ± 1.6	0.84 ± 0.12	24.7 ± 3.0
G4-NH_2 (50 μM)	5.3 ± 1.3	0.74 ± 0.06	23.6 ± 4.8
[G1]/[$C_{60}OH_{20}$] = 0.05	79.18	0.25 ± 0.03	-25.0 ± 6.5
[G1]/[$C_{60}OH_{20}$] =1.37	1071	0.24 ± 0.04	9.7 ± 6.4
[G4]/[$C_{60}OH_{20}$]= 0.001	196.7	0.18 ± 0.02	-52.1 ± 4.9
[G4]/[$C_{60}OH_{20}$]= 0.04	403.2	0.20 ± 0.03	-12.7 ± 7.8

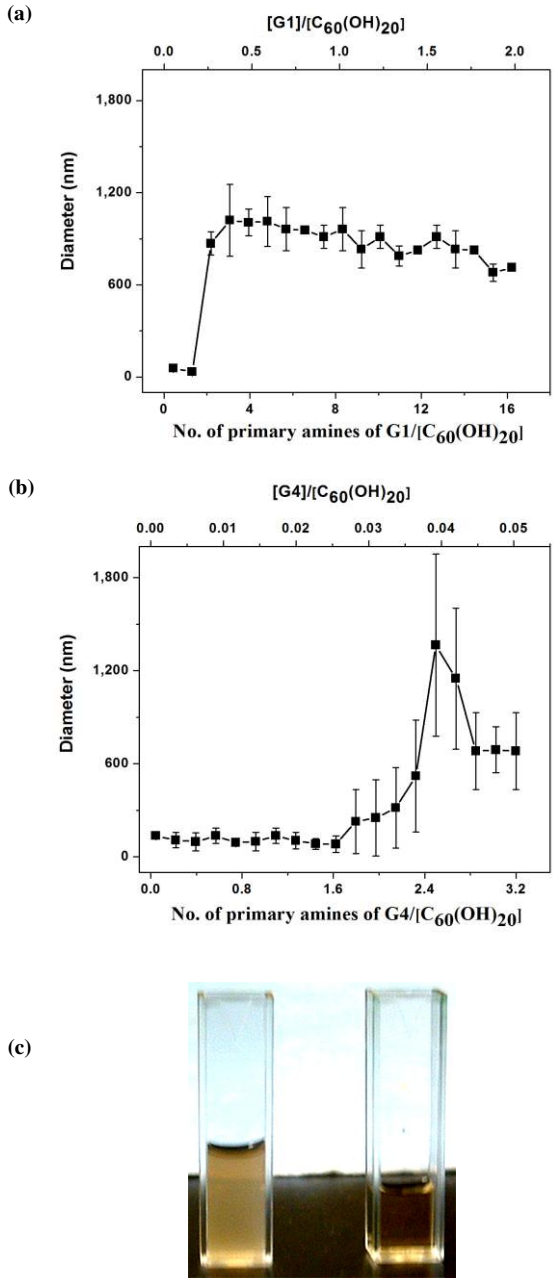

Figure 5-1. DLS measurements of (a) G1/fullerenol and (b) G4/fullerenol assemblies, and (c) image of G4/fullerenol complexes at a ratio of number of primary amines of G4/fullerenol = 3 (left) and 2.2 (right). An abrupt increase in the hydrodynamic size of the complexes was observed for both G1/fullerenol and G4/fullerenol mixtures at a ratio of number of primary amines of dendrimer/fullerenol ≈ 2 (354).

5.4. Thermodynamics of Dendrimer-Fullerenol Assembly

ITC was performed with a VP-ITC Isothermal Titration Microcalorimeter (MicroCal, Inc.) with dendrimers in the injection syringe and fullerenol in the experimental cell, while the reference cell contained deionized water. Concentration of fullerenol in the experimental cell was 10 μM (0.0106 g/L) for reactions with G1 dendrimer and 100 μM (0.106 g/L) for G4 dendrimer. The concentrations of G1 and G4 dendrimers in the injection syringe were 200 μM and 50 μM, respectively. The initial volume of fullerenol in the reaction cell was 1.46 mL. Each experimental run consisted of 31 to 35 injections of 8 μL each at an interval of 3 min between successive injections. The sample cell was maintained at 25°C and stirred at 200 rpm. Heats of dilution of dendrimers were subtracted from the final ITC results. Due to the negligible dilution of fullerenol, heats of dilution of fullerenol were minimal. Apparatus cleaning was performed according to the manufacturer's recommendations prior to the experiments. Baseline corrections and data fitting were performed using automated routines in Origin v.7.0 data analysis and acquisition software (OriginLab Corp.). Minor corrections were done at user's discretion. Figure 5-2 shows the raw ITC data of power vs. time and the resulting peak integrations are plotted as energy per mole of injectant (ΔH) vs. the molar ratio of dendrimers per fullerenol (n) in the sample cell after each injection. Analysis of the ITC data was done using the *One set of sites* model. Due to the larger size of dendrimers compared to fullerenols, in our experiments, dendrimers were considered as macromolecules and fullerenols as ligands. Hence, during data analysis, a selection of 'Ligand in Cell' was made. A much larger raw heat was observed in the case of G4 dendrimers than in the case of G1 dendrimers since, in the case of G4 dendrimers, 44

fullerenols bound to each dendrimer instantaneously releasing a larger amount of heat, whereas only one fullerenol binds to G1. It is noted that with fullerenols in the injection syringe and dendrimers in the experimental cell, we would have observed a lesser raw heat release due to the presence of excess dendrimers and fewer fullerenols. In such case, it would have taken a longer time to reach saturation in heat release.

The enthalpic change (ΔH) of dendrimer-fullerenol binding indicated a net exothermic reaction (Figure 5-2). As fullerenols in suspension were being consumed by dendrimers, the heat released upon each dendrimer-fullerenol binding decreased to reach a near saturation. The reactions were spontaneous, as indicated by the negative Gibbs free energy ΔG. Upon binding to fullerenols the much lower entropy ΔS of G1 dendrimers in contrast to that of G4 dendrimers implies a higher degree of ordering in the G1/fullerenol system. G1 being more flexible than G4 is arrested on complexation with the fullerenols leading to an increase in its order in contrast to the highly ordered structure of the pristine G4 dendrimers. For G1 dendrimer, whose size is comparable to that of fullerenol, the binding stoichiometric ratio n of fullerenol to dendrimer was ~1. In consistency with the DLS data, which showed formation of dendrimer-fullerenol supramolecular complexes of nearly uniform sizes above a G1/fullerenol molar ratio of 0.27 (corresponding to 2.19 primary amines of G1/fullerenol), a gradually decreasing heat release above this ratio was observed; this suggests lingering interactions between the dendrimer-fullerenol aggregates. For G4 dendrimer, by contrast, the binding stoichiometric ratio was nearly proportional to the number of primary amines (64) on the dendrimer, at 44.1. The binding curves also suggest that saturation was reached faster in the case of G4 dendrimer at a G4/fullerenol ratio of 0.04 (corresponding to 2.14 primary amines of G1/fullerenol), implying completion

of the binding and in agreement with the DLS data (Figure 5-1). Such saturation was not reached for G1 dendrimers, perhaps due to the presence of free fullerenols (354).

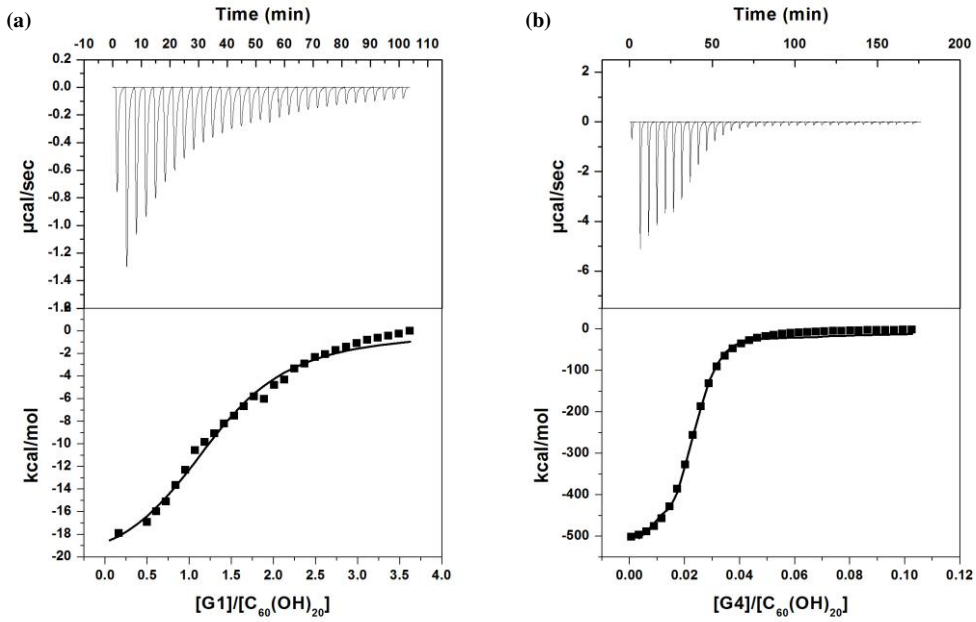

Figure 5-2. ITC raw data and analysis plots of (a) G1/fullerenol and (b) G4/fullerenol complexes. The interactions between dendrimers and fullerenols resulted in significant heat release (ΔH = -21.8 kcal/mol for G1/fullerenol and -19.5 kcal/mol for G4/fullerenols). The fullerenol:dendrimer stoichiometric ratios obtained from data analysis were 1.34 ± 0.04 for G1/fullerenol and 44.1 ± 0.43 for G4/fullerenol. The ΔG values for both G1/fullerenol (-7.69 kcal/mol) and G4/fullerenol (-7.24 kcal/mol) indicate the reactions are similarly spontaneous. G1/fullerenol complexes are also more ordered (ΔS = -47.4 × 10^{-3} kcal/mol) than G4/fullerenol complexes (ΔS = -15.8 × 10^{-3} kcal/mol) (354).

Whereas the spontaneity of the interactions between G1 and G4 dendrimers with fullerenols was similar, the entropy and enthalpy of the G4 dendrimer-fullerenol interaction were slightly less than that between G1 dendrimer and fullerenols. This could be attributed to the more open and hydrophilic structure of G1 over G4 dendrimers. At neutral pH, both

the interiors of G1 and G4 PAMAM dendrimers remained hydrophobic, while their exterior primary amines were protonated. Fullerenols, however, were partially negatively charged at neutral pH, resulting from the high electronegativity of the surface oxygens and deprotonation of the surface hydroxyl groups ($pK_a \sim 4$) (345). The assembly of dendrimer-fullerenol was therefore possibly mediated by ionic interactions between the protonated dendrimer amines and the negatively charged fullerenol oxygens, as well as by H-bonding between the fullerenol surface oxygens and the hydrogens on the dendrimer amine groups.

5.5. Intermolecular Interactions in Dendrimer-Fullerenol Assembly

A Cary Eclipse fluorescence spectrophotometer (Varian, Inc.) was used to measure the fluorescence of the dendrimer-fullerenol assemblies. 1 μL of aqueous dendrimer solution was added in gradient concentrations to 500 μL of fullerenol in a 1 mm path length quartz cuvette and allowed to incubate for 5 min after a 30 sec mixing. Spectrum scans between 400-600 nm of the fluorescence emitted by the control samples and the mixture upon excitation at 340 nm were conducted after 5 min incubation each time. Fluorescence intensities were recorded until complete quenching was observed. Measurements were repeated with three samples for statistical error analysis. Recorded fluorescence spectra were corrected for their respective blanks (i.e., fullerenols and dendrimers only).

As shown in Figure 5-5, increased dendrimer concentrations resulted in the quenching of fullerenol fluorescence (346), which was accompanied by a shift in the fluorescence maximum. This indicates that upon excitation, dendrimers and fullerenols formed charge-transfer complexes. In the case of G1 dendrimer, above a ratio of 1.9 for the number of primary amines/fullerenol, scattering from large aggregates resulted in a slight

increase in fluorescence, whereas precipitation of the large aggregates above that ratio in the case of G4/fullerenol prevented further measurements. The fluorescence intensity of fullerenols alone was linearly dependent on its concentration (Figure 5-3 (a,b)). Dendrimers, in comparison, displayed weak concentration dependence for their autofluorescence (Figure 5-4 (a,b)). However, quenching and peak shift upon fullerenol binding with dendrimers were notable. Specifically, a blue shift of 21 nm, averages for both G1 and G4-fullerenol, was observed for increased concentrations of dendrimers bound with fullerenols. Charge-transfer complexes could be formed between the hydroxyl groups of fullerenol and the protons on the amines of dendrimers.

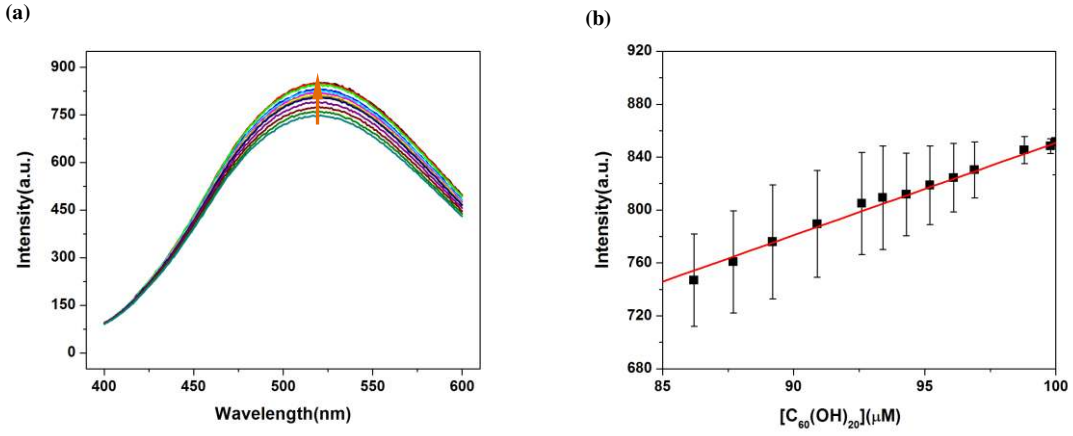

Figure 5-3. (a) Fluorescence emission of $C_{60}(OH)_{20}$ at different concentrations. Ex.: 340 nm. Arrow indicates the direction of increasing concentration. (b) Plot of intensity of fluorescence emission of $C_{60}(OH)_{20}$ vs. concentration at Ex/Em = 340/520 nm (354).

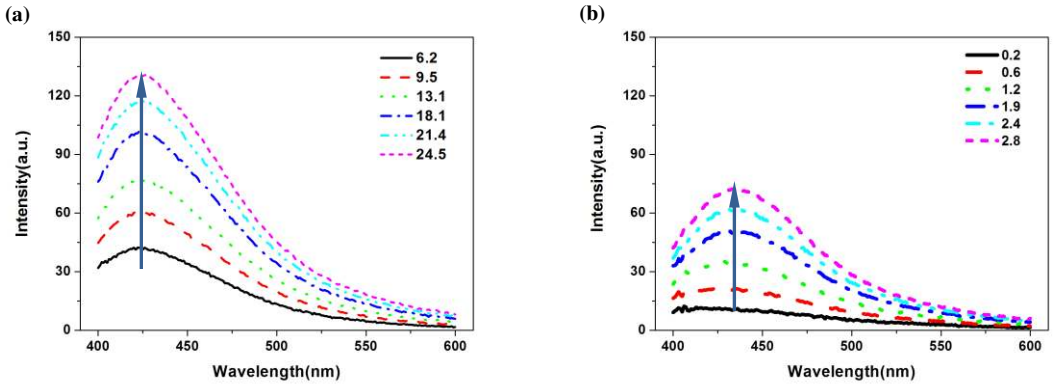

Figure 5-4. Fluorescence emission of (a) G1 and (b) G4 at different concentrations. Ex.: 340 nm. Arrow indicates the direction of increasing concentrations (on the right) in μM (354).

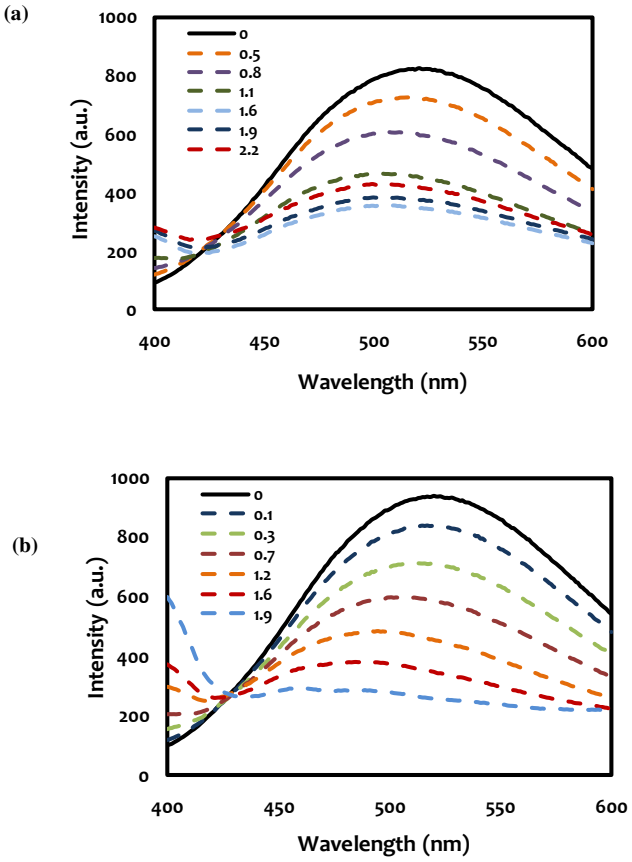

Figure 5-5. Fluorescence emission of fullerenol in the presence of increasing amounts of (A) number of primary amines of G1 per fullerenol = 0, 0.5, 0.8, 1.1, 1.6, 1.9, and 2.2; and (B) number of primary amines of G4 per fullerenol = 0, 0.1, 0.3, 0.7, 1.2, 1.6, and 1.9 (354).

Quenching of fluorescence can be described by the Stern-Volmer equation as (347, 348):

$$\frac{F_0}{F} = (1 + K_{SV}[Q\})(\exp V[Q]) \qquad (5\text{-}1)$$

where F_o and F are the fluorescence intensities of the fluorophore (fullerenol) in the absence and presence of a quencher (dendrimer), respectively, K_{SV} and V are the Stern-Volmer and sphere-of-action quenching constants, and $[Q]$ is the concentration of the quencher (dendrimer). As seen in Figure 5-6, the Stern-Volmer plot is nonlinear with a positive deviation for G1/fullerenol complexes, indicating simultaneous occurrence of both dynamic and static quenching. For low dendrimer concentrations, sphere-of-action quenching dominated. The value of V calculated from the data fitted with Equation 5-1 yielded 0.028×10^5 M^{-1}. For higher dendrimer concentrations, dynamic or collisional quenching through charge-transfer, H-bonding and electrostatic interactions between the already formed complexes and newly added dendrimers dominated, yielding $K_{SV} = 0.96 \times 10^5$ M^{-1}. A smaller value of V indicates that the fullerenol fluorescence was quenched primarily by dynamic quenching between the two species. In the case of G4/fullerenol, the Stern-Volmer plots are linear throughout (Figure 5-6), indicating the quenching was primarily dynamic. The linear Stern-Volmer constant K_{SV} obtained from the fitted data is 3.3×10^5 M^{-1}. The three-fold higher value of K_{SV} for G4/fullerenol complexes is due to the larger surface area of the G4 dendrimers which offers many more intermolecular contacts with fullerenol aggregates than those observed for G1 dendrimers, thus increasing their efficiency for quenching fullerenols.

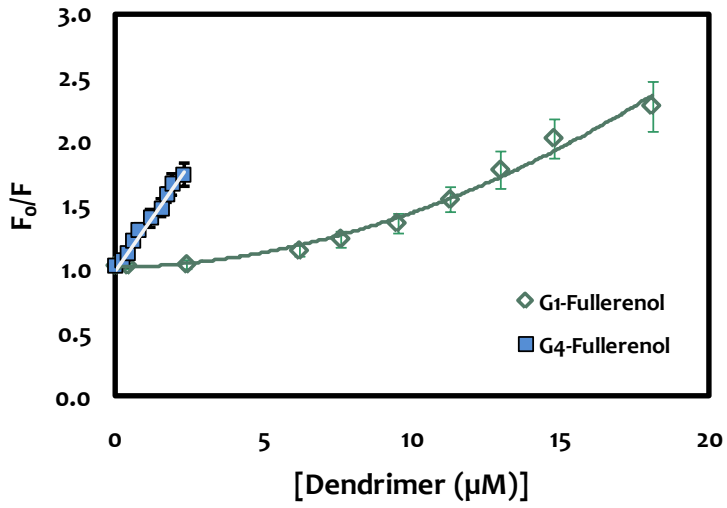

Figure 5-6. Stern-Volmer plots for G1/fullerenol and G4/fullerenol complexes. G1/fullerenol complexes show coexistence of static and dynamic quenching with a positive deviation in the plot, whereas G4/fullerenol complexes show primarily dynamic quenching, indicated by the linearity of the plot (354).

A modified Stern-Volmer equation (Equation 5-2) offers new insight into the binding affinity of the static quenching process (287).

$$\frac{F}{\Delta F} = \frac{1}{f_a K_a [Q]} + \frac{1}{f_a} \qquad (5\text{-}2)$$

ΔF is the difference of the fluorescence intensities in the absence and presence of a quencher, K_a is the effective quenching constant for accessible fluorophores and is directly related to the binding constant for the quencher-acceptor system (assuming the decrease in fluorescence stems from static collision due to complex formation), and f_a is the fraction of the fluorophore that is initially accessible to the quencher. The values of K_a (binding constant between fullerenols and dendrimers) and f_a (fraction of accessible fullerenols) are calculated from plot of $F_o/\Delta F$ vs $[Q]^{-1}$. The value of binding constant obtained in case of

G4/fullerenol (2.64×10^5 M^{-1}) is in excellent agreement with our ITC results (2.69×10^5 M^{-1}). In contrast, the value in the case of G1/fullerenol (1.0×10^5 M^{-1}) is much lower than our ITC measurement (4.35×10^5 M^{-1}). Note that ITC measures the binding constant as a result of combined electrostatic interactions, complex formations, H-bonding, as well as hydrophobic interactions, whereas those obtained from fluorescence measurements primarily resulted from complex formation via ionic bonding and Lewis acid-base reaction. This reiterates our hypothesis that G4 formed stronger complexes with fullerenols than G1 throughout the concentration range used. However, complex formation between G1 and fullerenols was the strongest in the lower concentration region, after which, large agglomerates were formed (as shown from the DLS data) due to other interactions through H-bonding and hydrophobic interactions. The fraction of accessible fullerenols calculated from the modified Stern-Volmer equation (f_a = 1.09 for G1/fullerenol and 1.23 for G4/fullerenol) implies that, initially, there might be more than one binding site of fullerenol for dendrimers and the molecular environment of fullerenol was easily accessible to the dendrimer (354). In addition, the spectral shift observed could be attributed to selective quenching of exposed vs. buried fluorophore sites of the fullerenol (349).

5.6. Discussions and Summary

The thermodynamics, stoichiometric ratio and binding mechanisms of dendrimer-fullerenol assembly have been studied by the experimental techniques of DLS, ITC, and spectrophotometry. The formation of dendrimer-fullerenol assemblies, at a maximum loading capacity of ~2 or 44 fullerenols per G1 or G4 dendrimer (corresponding to ~2 primary amines per fullerenol in both cases) was found to be energetically favorable. In

addition, inter-cluster interactions were evident, as a result of electrostatic forces, H-bonding, ionic bonding, as well as Lewis acid-base reaction as evidenced from the Stren-Volmer constants. Apparently, such inter-cluster formation can be controlled by adjusting both the concentrations of the fullerenol and the dendrimer, and by tuning the molar ratio of dendrimer to fullerenol. While inter-cluster interaction should be minimized for the delivery of fullerene derivatives by a dendrimer -- in light of their diffusion in the bloodstream and eventual cell uptake, inter-cluster interaction is deemed desirable for mitigating the accidental release of nanomaterials in the environment. Based on our study, we recommend a G1/fullerenol loading ratio of 0.2-1.6, and G4/fullerenol loading ratio of 0.005-0.02 for drug delivery (the range below precipitation), and a G1/fullerenol loading ratio of above 1.6, and a G4/fullerenol loading ratio of above 0.02 for environmental remediation. Furthermore, for both nanomedicinal and environmental applications, the assembly of dendrimer and fullerenol -- as exemplified in the current study -- may be extended to that of branched/hyperbranched polymers and nanoparticles of opposite charge.

CHAPTER SIX

CONCLUSION AND FUTURE WORK

This dissertation had two major goals: furthering the fundamental understanding of the *implications* of nanomaterials on ecosystems (Part I), and advancing the *applications* of nanomaterials for environmental remediation (Part II) -- both aspects were investigated using the principles of physics and physical chemistry. With these focuses, the following major observations have been made:

6.1. Part I: Environmental Implications of Nanomaterials

In Chapter two, the effects of the adsorption of two types of synthetic NPs – QDs and PS NPs on the photosynthetic activities of green algae were investigated. We found that

- water-soluble CdSe/ZnS QDs, a major class of ENPs, have a high affinity for *Chlamydomonas* sp. The adsorption of QDs to the algal cell surfaces was a combined result of nonspecific interactions such as possible electrostatic interactions between the amine groups of the glycoproteins and the carboxylate groups of the MUA ligands coated on the QDs, as well as hydrogen bonding between polysaccharides on the algal cell walls and the latter. The porous structure of the algal cell wall could have afforded ample binding sites for the QDs;
- the amount of QDs adsorbed onto algae logarithmically depended upon the equilibrium concentration of the QDs;
- no clear evidence of QDs internalization by algae was found from our TEM study, although QD adsorption on the algae surface was apparent from our bright field and

confocal fluorescence imaging. This lack of internalization may be explained as a result of the thick algal cell wall, the size and mutual aggregation of the QDs, and a lack of endocytosis capability of the algae;

- the adsorption of QDs hindered the photosynthetic activity of algae, as indicated by both reduced CO_2 depletion for QDs over 100 ppm and declined O_2 production for small doses of QDs. These physiochemical phenomena were likely caused by the adsorbed QDs which impeded gas flow and nutrients uptake for the algae; although no apparent algal cell death was observed in our current study implying limited adversity administered by algal exposure to QDs.

Similarly to QDs, the adsorption of nanosized plastic beads was also found to hinder algal photosynthetic activities and promote their ROS production. Specifically, we found that

- such adsorption depended upon the physicochemical properties of the plastic and the morphological and biochemical properties of the algae. The plausible physical chemistry for the adsorption, much in favor of the positively charged plastic, included electrostatic interaction, hydrogen bonding, and hydrophobic interaction between the algal species and the plastic. A recent study (287) showed that adsorption of carbonaceous nanomaterials like CNTs and soot did inhibit algal growth due to the shading effect induced by agglomeration and adsorption of the nanomaterials onto the algal cells. However, no change in the photosynthetic activities of the algal cells was observed in that study based on a measurement of the quantum yield of photosystem II in the thylakoids. Since such approach was focused on the efficiency of energy conversion at the photosynthetic centers, it yielded

relative not absolute photosynthetic activity. Conceivably, the relative photosynthetic activity would reduce only if the protein complex of the photosystem would be impaired, or viability of the algal cells would be reduced. Since none of these phenomena were observed in their study, the major contributing factor to the reduced photosynthetic activity in our study was most likely hindered gas exchange as a result of NP adsorption onto the porous algal cell walls;

- one possible benefit of the hindered algal photosynthesis lies in the removal of toxic algal blooms from reservoirs that are used to store drinking water, and from other aquatic ecosystems where overabundance of algae poses significant economic concerns.

Since algae are a primary food source for aquatic organisms, further studies to decipher the mechanisms and long-term effects of the interactions between algae and various types of ENPs are deemed necessary. It should be noted that not all QDs are alike. The absorption, distribution, metabolism, excretion, and toxicity of QDs may depend on multiple factors derived from both their inherent physicochemical properties, concentration, capping material bioactivity, and oxidative, photolytic, and mechanical stability. In addition, very little is known about the stability of QDs in the environment and into which environmental compartment (air, water or soil) they would partition into. Such knowledge is an important prerequisite for evaluating the degradation kinetics of QDs in the environment, which will in turn dictate their toxicity. In consideration of the biosphere in the environment, the stability of QDs should also be considered for determining their toxicity *in vivo*. A study by Hoshino et al. (350) found that treatment with the QD capping material MUA alone (without QDs) for 12 h caused severe cytotoxicity in murine T-cell lymphoma

(EL-4) cells at 100 μg/mL. Under oxidative and photolytic conditions, QD core–shell coatings may degrade, thus exposing potentially toxic capping material or resulting in dissolution of the core complex to metal components (e.g., Cd, Se). Such released metals may enter the cell through specific transport channels across cell membrane and once inside the cell, metals may activate various intracellular enzymes and entire cascades of intracellular reactions. While several mechanisms are known for the entry of NPs into plant cells (binding to carrier proteins, aquaporins, ion channels, endocytosis or the creation of new pores) (351), it is not yet known which mechanisms are at play for *Chlamydomonas* sp. and further studies in elucidating such mechanisms are necessary for fully understanding the ecotoxicological effects of NPs.

6.2. Part II: Environmental Applications for Nanomaterials

Part II of this dissertation aimed at advancing the fundamental physico-chemical understanding of dendritic polymers for enabling their application in environmental remediation, particularly drinking water treatment. To this end, I have (a) described the essential characteristics of a PAMAM dendrimer in hosting a variety of chemical species (Chapter three), (b) devised a novel analytical scheme for improving the detection limits of pollutants by PAMAM dendrimers (Chapter four), and (c) characterized these soft, environmentally benign nanomaterials for mitigating potentially harmful discharged nanoparticles from the aqueous environment (Chapter five).

6.2.1. Chapter Three - Understanding the physico-chemical behavior of dendrimers in hosting a variety of chemical species

The goal of this chapter was to establish the hosting and releasing capacity of PAMAM dendrimers for a variety of chemical species. The selective absorption and maximum loading of a tris-dendrimer was characterized for major chemical species of environmental relevance, namely – cationic copper, anionic nitrate, and PAH PN at different pH values. The tri-functionality of the tris-dendrimer could be advantageous owing to its higher surface charge density than the cationic or anionic monofunctional PAMAM dendrimers.

The primary host-guest interactions ranged from LMCT complex formation (Cu(II)) to electrostatic (NO_3^-) and hydrophobic (PN) interactions. Due to its uncharged interior at high pH, tris-dendrimer afforded relatively hydrophobic and ample cavities for PN molecules to sequester within. PN molecules are in a high-energy state in an aqueous environment and hence encapsulation in a hydrophobic dendrimer interior was energetically favorable. Furthermore, charge-transfer complexation between the aromatic rings of PN and the tertiary dendrimer amines were also feasible. On the other hand, Cu(II) formed complexes with the tertiary amines of the dendrimer interior at high pH values. Remarkably, when the pH was lowered to 2, both PN and Cu(II) were released from the dendrimer interior. At low pH values, the dendrimer tertiary amines become protonated to render dendrimer interior hydrophilic; since water molecules are in a lower free energy state inside the dendrimer than in the bulk exterior, PN molecules were released from the relatively more hydrophilic interior while Cu(II) ions were ejected due to enhanced electrostatic repulsions by the protonated amines. In contrast, NO_3^- ions interacted with the protonated amines via electrostatic attractions, but were only released when the pH was raised and the amines became deprotonated. The G4-tris-dendrimer used in this study demonstrated an

exceptional hosting capacity towards Cu(II) at 64 ions per dendrimer (pH = 10), NO_3^- at 32 ions per dendrimers (pH = 2), and PN at 10 molecules per dendrimer (pH = 7).

In addition, we have demonstrated efficient removal of dissolved humic acid using PAMAM dendrimers. HA is an extremely complex molecule consisting of several anionic chemical groups at neutral pH including carboxyls, hydroxyls, ketones and quinones. PAMAM dendrimers due to their high degree of surface functionalities behaved as a "nanosponge" in adsorbing such complex molecular species. Central to this method was complex formation resulting from electrostatic interactions between the cationic dendrimers and the anionic HA at neutral pH, whose specific chemical bonds were identified by ATR-FTIR. Once charge neutralization was reached, at a stoichiometric ratio of ~2 g/g for HA:G5-PAMAM, subsequent fast aggregation occurred resulting from hydrogen bonding and hydrophobic interactions between the neutralized complexes and leading to precipitation of micron-sized aggregates. However, loading of additional dendrimers re-stabilized and re-suspended the aggregates via electrostatic repulsion.

Taken together, this above laboratory-scale study has demonstrated that PAMAM dendrimers cater to a more thermodynamically spontaneous adsorption process towards various chemical species and environmental pollutants than other conventional water purification procedures such as RO which require energy to drive the process to completion. Such properties of PAMAM dendrimers should appeal to future generations of water treatment devices.

6.2.2. Chapter Four- An enhanced detection of pollutants using dendrimers

In Chapter four, a novel optical scheme based on the field enhancing effect of an Au-NW was developed to selectively detect Cu(II) in aqueous solutions, down to the nM range by PAMAM dendrimers electrostatically immobilized on the Au-NW substrate. Such a detection limit is by far the lowest and most feasible amongst commonly used analytical schemes for metal ion detection. Furthermore, the detection limit of our scheme could be substantially improved in principle by optimizing the polarization direction of the illumination light, diameter of the Au-NWs, generation/size of the dendrimers, pH and temperature of the solvent, or by integrating with nanoelectronic devices such as NW-field effect transistors or micro- and nanofluidics (352). Additionally, the specificity of the detection scheme can be enhanced by maximizing the spectral overlap between the dendrimer label and the metal ions under study, or combining the current technique with analytical tools such as NMR and Raman spectroscopy.

6.2.3. Chapter Five - Dendritic nanotechnology for remediating discharged nanoparticles

In Chapter five, the unique physico-chemistry of two generations (G1 and G4) of amine-terminated PAMAM dendrimers were exploited to bind discharged fullerenols in aqueous systems. Specifically, we found that

- each fullerenol bound with two primary amines per dendrimer (both G1 and G4) through ionic bonding, and the formation of large aggregates due to inter-cluster interactions facilitated by H-bonding and hydrophobic interactions were evident.

Apparently, such inter-cluster formation can be controlled by adjusting both the concentrations of the fullerenol and the dendrimer, and by tuning the molar ratio of dendrimer to fullerenol;

- the formation of dendrimer-fullerenol assemblies, at a maximum loading capacity of ~2 or 44 fullerenols per G1 or G4 dendrimer was energetically favorable and thermodynamically spontaneous;
- complex formation was the strongest between G1 and fullerenols at lower G1/fullerenol molar ratios, after which large agglomerates were formed due to inter-complex interactions through H-bonding, whereas G4 formed stronger complexes in a wider molar ratio range due to the larger surface area of the G4 dendrimers which offered many more intermolecular contacts with fullerenol aggregates than G1 dendrimers.

Such inter-cluster interactions between dendrimer-fullerenol complexes are deemed desirable for mitigating the accidental release of nanomaterials in the environment; however they should be minimized for the drug delivery of fullerene derivatives by a dendrimer -- in light of their diffusion in the bloodstream and eventual cell uptake. Based on this study, we recommend a G1/fullerenol loading ratio of 0.2-1.6, and G4/fullerenol loading ratio of 0.005-0.02 for drug delivery (the range below precipitation), and a G1/fullerenol loading ratio of above 1.6, and a G4/fullerenol loading ratio of above 0.02 for environmental remediation. Furthermore, for both nanomedicinal and environmental applications, the scope of this study may be extended to that of branched/hyperbranched polymers and NPs of opposite charge.

6.3. Future Work

During my PhD research, I have thoroughly studied the fundamental physico-chemical properties of PAMAM dendrimers with the goal of promoting their broad application in drinking water remediation. Results of this dissertation suggest that dendritic nanotechnology could be developed or integrated into advanced, sustainable, cost and energy efficient, and biocompatible water treatment technologies.

I'd like to further research on using dendritic polymers for water treatment in the following areas:

1. *Extending the scope of contaminant detection by dendritic polymers and comparing binding capacity with hyperbranched polymers:* Very little is known about interactions between dendritic polymers and radionuclides. Although, based on preliminary investigations of using dendrimers as MRI contrast agents and hosting differently charged ions in their interiors provide a good basis for extending their usage for radionuclides, thorough experimental detection schemes need to be devised. Much is to be explored in terms of the binding capacity of hyperbranched polymers towards different chemical species. Another area to be explored is the ability of these dendritic polymers to disperse spilled oil (355), a paramount environmental hazard associated with the daily operation of the petroleum industry offshore. Energetically, the hydrophobic interior of these polymers at ambient water pH provide for ample space for hydrophobic oil molecules to partition in. I intend to explore the above with leading scientists at the Pacific Northwest National Laboratory during my postdoctoral research.

2. *Understand the behavior of membrane bound dendritic polymers in small systems:* Employing dendritic polymers in water quality control systems involves designing separation methodologies such as functionalizing membranes with these polymers, thereafter subjecting them to pressure and temperature gradients existing in small water treatment systems, understanding their binding capacity with the membranes, as well as the capture, retention and release of the targeted species. Future work may be devoted to fill this gap between dendritic polymer science and development of sustainable systems utilizing these polymeric nanomaterials. Such research will enable the design, optimization, and large-scale applications of dendritic polymers towards sustainable water treatment technologies. For example, functioning of tight UF membranes coated with dendrimers – either through specific (covalent functionalization) or non-specific (electrostatic) interactions – and other novel nanostructured membranes such as graphene nanosheets, could be optimized under ambient water temperature and pressure conditions, and regeneration of these dendritic polymers *in situ* could be evaluated.
3. *Evaluate the biocompatibility of dendritic polymers used for water treatment:* To fully capitalize on the promising properties of dendritic polymers for sustainable environmental remediation, effort must be spent on evaluating the ecological impact of such synthetic materials. Although a number of dendrimer toxicity and biodistribution studies have been carried out during the last five years, effects of dendrimer core and terminal group chemistry, size, shape, hydrophobicity on cell membranes and whole organisms are not well understood. Furthermore, only a handful

studies have been published on the fate and transport of dendrimers in the environment. Hence, a systematic study of the impacts of dendritic and hyperbranched polymers on ecosystems, especially on the cellular level, is one of my future research plans.

While over 70% of the earth's surface is covered by water, only about 3% of it is available for human consumption. Even worse, in developing countries, 80% of illnesses are water related. There are 3.3 million deaths in the world every year due to diarrheal diseases. Research in recent years and in this dissertation has shown great promise of using CNTs, graphene and dendritic polymers for alleviating this global water crisis. In addition to providing technical solutions to the staggering challenge for potable drinking water, regulatory and public acceptance to using nanotechnology for drinking water treatment must be established. In addition, life cycle assessments of the risks and benefits of these nanomaterials are crucially necessary.

In addition to environmental remediation, dendritic nanomaterials also show promise in efficient energy storage and improving fuel cell technology. Due to their enormous surface area and a high degree of surface functionalities, these polymers can serve as excellent catalysts as well as energy transfer and storage materials. One of the key areas I plan to explore is the use of dendritic polymers as electrolytes to prevent the formation of Li dendrites as a result of overcharging in Li ion battery cells.

It is through this PhD training that I have gained the knowledge and come to the realization that my future career resides in the truly interdisciplinary and exciting fields of water treatment and energy applications.

APPENDIX

A: Glossary of Terms

Symbol	Quantity
AuNW	gold nanowire
CNT	carbon nanotube
CTAB	cetyltrimethylammonium-bromide
DCF	dichlorofluorescein
DCFH-DA	dichlorodihydrofluorescin diacetate
DI	deionization
DLS	dynamic light scattering
EM	electron microscopy
ENP	engineered nanoparticle
EPS	extended poly(styrene)
H-bonding	hydrogen bonding
HA	humic acid
HAA	haloacetic acid
ITC	isothermal titration calorimetry
LOD	limit of detection
MALDI	matrix-assisted laser desorption
MBR	membrane bioreactor
MF	microfiltration
MUA	mercaptoundecanoic acid

MWCNT	multiwalled carbon nanotube
NF	nanofiltration
NOM	natural organic matter
NZVI	nanoscale zero valent iron
NP	nanoparticle
PAH	poly(aromatic) hydrocarbon
PAMAM	poly(amidoamine)
PCB	polychlorinated biphenyl
PE	poly(ethylene)
PN	phenanthrene
POP	persistent organic pollutant
PP	poly(propylene)
PS	poly(styrene)
QD	quantum dot
RO	reverse osmosis
ROS	reactive oxygen species
SAMMS	self-assembled monolayers on mesoporous supports
SEM	scanning electron microscopy
SPR	surface plasmon resonance
TCE	trichloroethylene
TEM	transmission electron microscopy
THM	trihalomethane
UF	ultrafiltration

US-EPA	United States Environmental Protection Agency
UV	ultra-violet
ZVI	zero valent iron

REFERENCES

1. Robbens, J.; Vanparys, C.; Nobels, I.; Blust, R.; Van Hoecke, K.; Janssen, C.; De Schamphelaere, K.; Roland, K.; Blanchard, G.; Silvestre, F.; Gillardin, V.; Kestemont, P.; Anthonissen, R.; Toussaint, O.; Vankoningsloo, S.; Saout, C.; Alfaro-Moreno, E.; Hoet, P.; Gonzalez, L.; Dubruel, P.; Troisfontaines, P. Eco-, geno- and human toxicology of bio-active nanoparticles for biomedical applications. *Toxicology* **2010,** *269,* 170-181.

2. Savolainen, K.; Alenius, H.; Norppa, H.; Pylkkanen, L.; Tuomi, T.; Kasper, G. Risk assessment of engineered nanomaterials and nanotechnologies-A review. *Toxicology* **2010,** *269,* 92-104.

3. Stern, S.T. and McNeil, S.E. Nanotechnology safety concerns revisited. *Toxicological Sciences* **2008,** *101,* 4-21.

4. Hannah, W. and Thompson, P.B. Nanotechnology, risk and the environment: a review. *J. Environ. Monit.* **2008,** *10,* 291-300.

5. Kahru, A. and Dubourguier, H.-. From ecotoxicology to nanoecotoxicology. *Toxicology* **2010,** *269,* 105-119.

6. Colvin, V.L. The potential environmental impact of engineered nanomaterials. *Nat. Biotechnol.* **2003,** *21,* 1166-1170.

7. Bernhardt, E.S.; Colman, B.P.; Hochella, M.F.,Jr.; Cardinale, B.J.; Nisbet, R.M.; Richardson, C.J.; Yin, L. An ecological perspective on nanomaterial impacts in the environment. *J. Environ. Qual.* **2010,** *39,* 1954-1965.

8. Brouwer, D. Exposure to manufactured nanoparticles in different workplaces. *Toxicology* **2010,** *269,* 120-127.

9. Forinash, K. *Foundations of Environmental Physics: Understanding energy use and human impacts.* Island Press: Washington, DC, **2010**; pp. 440.

10. American Elements Nanotechnology Information Center: Properties, Applications, Research, and Safety Guidelines. *May 9, **2012**,*

11. Jolivet, J.P.; Barron, A.R. Nanomaterials fabrication, In *Environmental Nanotechnology: Applications and Impacts of Nanomaterials,* Wiesner, M.R.; Bottero, J.Y., Eds.; The McGraw-Hill Companies: New York, **2007**; pp. 30.

12. Zong, R.; Zhou, J.; Li, B.; Fu, M.; Shi, S.; Li, L. Optical properties of transparent copper nanorod and nanowire arrays embedded in anodic alumina oxide. *J. Chem. Phys.* **2005,** *123,* 094710-1-5.

13. Risha, G.A.; Son, S.F.; Yetter, R.A.; Yang, V.; Tappan, B.C. Combustion of nano-aluminum and liquid water. *Proceedings of the Combustion Institute* **2007,** *31,* 2029-2036.

14. Sanchez, A.; Abbet, S.; Heiz, U.; Schneider, W.; Hakkinen, H.; Barnett, R.; Landman, U. When gold is not noble: Nanoscale gold catalysts. *J. Phys. Chem. A* **1999,** *103,* 9573-9578.

15. Bhattacharya, P.; Gohil, S.; Mazher, J.; Ghosh, S.; Ayyub, P. Universal, geometry-driven hydrophobic behaviour of bare metal nanowire clusters. *Nanotechnology* **2008,** *19,* 075709-1-5.

16. Zhang, P.; Tevaarwerk, E.; Park, B.; Savage, D.; Celler, G.; Knezevic, I.; Evans, P.; Eriksson, M.; Lagally, M. Electronic transport in nanometre-scale silicon-on-insulator membranes. *Nature* **2006,** *439,* 703-706.

17. Navarro, E.; Baun, A.; Behra, R.; Hartmann, N.; Filser, J.; Miao, A.; Quigg, A.; Santschi, P.; Sigg, L. Environmental behavior and ecotoxicity of engineered nanoparticles to algae, plants, and fungi. *Ecotoxicology* **2008,** *17,* 372-386.

18. Guldi, D.M.; Prato, M. Excited-state properties of C60 fullerene derivatives. *Acc. Chem. Res.* **2000,** *33,* 695-703.

19. Brunner, T.J.; Wick, P.; Manser, P.; Spohn, P.; Grass, R.N.; Limbach, L.K.; Bruinink, A.; Stark, W.J. In vitro cytotoxicity of oxide nanoparticles: Comparison to asbestos, silica, and the effect of particle solubility. *Environ. Sci. Technol.* **2006,** *40,* 4374-4381.

20. Warheit, D.B.; Laurence, B.R.; Reed, K.L.; Roach, D.H.; Reynolds, G.A.M.; Webb, T.R. Comparative pulmonary toxicity assessment of single-wall carbon nanotubes in rats. *Toxicological Sciences* **2004,** *77,* 117-125.

21. Lam, C.; James, J.T.; McCluskey, R.; Hunter, R.L. Pulmonary toxicity of single-wall carbon nanotubes in mice 7 and 90 days after intratracheal instillation. *Toxicological Sciences* **2004,** *77,* 126-134.

22. Georgakilas, V.; Pellarini, F.; Prato, M.; Guldi, D.M.; Melle-Franco, M.; Zerbetto, F. Supramolecular self-assembled fullerene nanostructures. *PNAS* **2002,** *99,* 5075-5080.

23. Guo, Z.; Sun, N.; Li, J.; Dai, L.; Zhu, D. Nanoscale aggregation of fullerene in nafion membrane. *Langmuir* **2002,** *18,* 9017-9021.

24. Mylon, S.E.; Chen, K.L.; Elimelech, M. Influence of natural organic matter and ionic composition on the kinetics and structure of hematite colloid aggregation: Implications to iron depletion in estuaries. *Langmuir* **2004,** *20,* 9000-9006.

25. Bernhardt, E.S.; Colman, B.P.; Hochella, M.F.; Cardinale, B.J.; Nisbet, R.M.; Richardson, C.J.; Yin, L. An ecological perspective on nanomaterial impacts in the environment. *J. Environ. Qual.* **2010,** *39,* 1954-1965.

26. Tabata, Y.; Murakami, Y.; Ikada, Y. Photodynamic effect of polyethylene glycol-modified fullerene on tumor. *Cancer Science* **1997,** *88,* 1108-1116.

27. Tokuyama, H.; Yamago, S.; Nakamura, E.; Shiraki, T.; Sugiura, Y. Photoinduced biochemical activity of fullerene carboxylic acid. *J. Am. Chem. Soc.* **1993,** *115,* 7918-7919.

28. Tsao, N.; Kanakamma, P.P.; Luh, T.; Chou, C.; Lei, H. Inhibition of Escherichia coli-induced meningitis by carboxyfullerence. *Antimicrobial Agents and Chemotherapy* **1999,** *43,* 2273-2277.

29. Käsermann, F. and Kempf, C. Buckminsterfullerene and photodynamic inactivation of viruses. *Rev. Med. Virol.* **1998,** *8,* 143-151.

30. Nakamura, E.; Tokuyama, H.; Yamago, S.; Shiraki, T.; Sugiura, Y. Biological activity of water-soluble fullerenes. Structural dependence of DNA cleavage, cytotoxicity, and enzyme inhibitory activities including HIV-protease inhibition. *Bulletin of the Chemical Society of Japan* **1996,** *69,* 2143-2151.

31. Tabata, Y.; Murakami, Y.; Ikada, Y. Antitumor effect of poly(ethylene glycol)-modified fullerene. *Fullerene Sci Technol* **1997,** *5,* 989-1007.

32. Oberdorster, E. Manufactured nanomaterials (fullerenes, C_{60}) induce oxidative stress in the brain of juvenile largemouth bbass. *Environ. Health Perspect.* **2004,** *112,* 1058-1062.

33. Baun, A.; Hartmann, N.; Grieger, K.; Kusk, K. Ecotoxicity of engineered nanoparticles to aquatic invertebrates: a brief review and recommendations for future toxicity testing. *Aquatic Toxicology* **2008,** *17,* 387-395.

34. Knox, J. The extracellular matrix in higher plants. 4. Developmentally regulated proteoglycans and glycoproteins of the plant cell surface. *The FASEB Journal* **1995,** *9,* 1004-1012.

35. Stanislav, V.; Tomas, R.; Pavel, K. Biosorption of Cd^{2+} and Zn^{2+} by cell surface-engineered Saccharomyces cerevisiae. *Int. Biodeterior. Biodegrad.* **2007,** *60,* 96-102.

36. Zemke-White, W.; Clements, K.D.; Harris, P.J. Acid lysis of macroalgae by marine herbivorous fishes: effects of acid pH on cell wall porosity. *J. Exp. Mar. Biol. Ecol.* **2000,** *245,* 57-68.

37. Fleischer, A.; O'Neill, M.A.; Ehwald, R. The pore size of non-graminaceous plant cell walls is rapidly decreased by borate ester cross-linking of the pectic polysaccharide rhamnogalacturonan II. *Plant Physiology* **1999,** *121,* 829-838.

38. Moore, M.N. Do nanoparticles present ecotoxicological risks for the health of the aquatic environment? *Environ. Int.* **2006,** *32,* 967-976.

39. Jia, G.; Wang, H.; Yan, L.; Wang, X.; Pei, R.; Yan, T.; Zhao, Y.; Guo, X. Cytotoxicity of carbon nanomaterials: single-wall nanotube, multi-wall nanotube, and fullerene. *Environ. Sci. Technol.* **2005,** *39,* 1378-1383.

40. Silva, L.; Oliva, M.; Azevedo, A.; Araújo, J. Responses of restinga plant species to pollution from an iron pelletization factory. *Water, Air, & Soil Pollution* **2006,** *175,* 241-256.

41. Imahori, H.; Mori, Y.; Matano, Y. Nanostructured artificial photosynthesis. *Journal of Photochemistry and Photobiology C: Photochemistry Reviews* **2003,** *4,* 51-83.

42. Hund-Rinke, K.; Simon, M. Ecotoxic effect of photocatalytic active nanoparticles (TiO_2) on algae and daphnids. *Environmental Science and Pollution Research* **2006,** *13,* 225-232.

43. Yang, L.; Watts, D.J. Particle surface characteristics may play an important role in phytotoxicity of alumina nanoparticles. *Toxicol. Lett.* **2005,** *158,* 122-132.

44. Lin, D.; Xing, B. Phytotoxicity of nanoparticles: Inhibition of seed germination and root growth. *Environmental Pollution* **2007,** *150,* 243-250.

45. Wong, S.; Leung, P.; Djurišić, A.; Leung, K. Toxicities of nano zinc oxide to five marine organisms: influences of aggregate size and ion solubility. *Analytical and Bioanalytical Chemistry* **2010,** *396,* 609-618.

46. Gélabert, A.; Pokrovsky, O.S.; Viers, J.; Schott, J.; Boudou, A.; Feurtet-Mazel, A. Interaction between zinc and freshwater and marine diatom species: Surface complexation and Zn isotope fractionation. *Geochim. Cosmochim. Acta* **2006,** *70,* 839-857.

47. Wong, S.; Leung, P.; Djurišić, A.; Leung, K. Toxicities of nano zinc oxide to five marine organisms: influences of aggregate size and ion solubility. *Analytical and Bioanalytical Chemistry* **2010,** *396,* 609-618.

48. Franklin, N.M.; Rogers, N.J.; Apte, S.C.; Batley, G.E.; Gadd, G.E.; Casey, P.S. Comparative toxicity of nanoparticulate ZnO, bulk ZnO, and $ZnCl_2$ to a Freshwater Microalga (Pseudokirchneriella subcapitata): The Importance of Particle Solubility. *Environ. Sci. Technol.* **2007,** *41,* 8484-8490.

49. Sondi, I. and Salopek-Sondi, B. Silver nanoparticles as antimicrobial agent: a case study on E. coli as a model for Gram-negative bacteria. *J. Colloid Interface Sci.* **2004,** *275,* 177-182.

50. Pal, S.; Tak, Y.K.; Song, J.M. Does the antibacterial activity of silver nanoparticles depend on the shape of the nanoparticle? A study of the gram-negative bacterium Escherichia coli. *Applied and Environmental Microbiology* **2007,** *73,* 1712-1720.

51. Fernandes, T.; Nielsen, H.; Burridge, T.; Stone, V. Toxicity of nanoparticles to embryos of the marine macroalgae Fucus serratus *2nd International conference on the environmental effects of nanoparticles and nanomaterials* **September 24-25, 2007,** *London, UK,*

52. Badireddy, A.R.; Hotze, E.M.; Chellam, S.; Alvarez ‖, P.; Wiesner, M.R. Inactivation of bacteriophages via photosensitization of fullerol nanoparticles. *Environ. Sci. Technol.* **2007,** *41,* 6627-6632.

53. Adams, L.K.; Lyon, D.Y.; Alvarez, P.J. Comparative eco-toxicity of nanoscale TiO_2, SiO_2, and ZnO water suspensions. *Water Res* **2006,** *40,* 3527-3532.

54. Kim, J.S.; Kuk, E.; Yu, K.N.; Kim, J.; Park, S.J.; Lee, H.J.; Kim, S.H.; Park, Y.K.; Park, Y.H.; Hwang, C.; Kim, Y.; Lee, Y.-.; Jeong, D.H.; Cho, M. Antimicrobial effects of silver nanoparticles. *Nanomedicine: Nanotechnology, Biology and Medicine* **2007,** *3,* 95-101.

55. McDonnell, G. and Russell, A.D. Antiseptics and disinfectants: Activity, action, and resistance. *Clinical Microbiology Reviews* **1999,** *12,* 147-179.

56. Hussain, S.M.; Hess, K.L.; Gearhart, J.M.; Geiss, K.T.; Schlager, J.J. In vitro toxicity of nanoparticles in BRL 3A rat liver cells. *Toxicology in Vitro* **2005,** *19,* 975-983.

57. Navarro, E.; Piccapietra, F.; Wagner, B.; Ka¨gi, R.; Odzak, N.; Sigg, L.; Behra, R. Toxicity mechanisms of silver nanoparticles to Chlamydomonas reinhardtii. *2nd International conference on the environmental effects of nanoparticles and nanomaterials* **September 24-25, 2007,** *London, UK.*

58. Miao, A.J.; Quigg, A.; Schwehr, K.; Xu, C.; Santschi, P. Engineered silver nanoparticles (ESNs) in coastal marine environments: bioavailability and toxic effects to the phytoplankton Thalassiosira weissflogii. *2nd International conference on the environmental effects of nanoparticles and nanomaterials* **September 24-25, 2007,** *London, UK.*

59. Derfus, A.M.; Chan, W.C.W.; Bhatia, S.N. Probing the cytotoxicity of semiconductor quantum dots. *Nano Lett.* **2004,** *4,* 11-18.

60. Domingos, R.F.; Simon, D.F.; Hauser, C.; Wilkinson, K.J. Bioaccumulation and effects of CdTe/CdS quantum dots on Chlamydomonas reinhardtii – Nanoparticles or the free ions? *Environ. Sci. Technol.* **2011,** *45,* 7664-7669.

61. Kloepfer, J.A.; Mielke, R.E.; Wong, M.S.; Nealson, K.H.; Stucky, G.; Nadeau, J.L. Quantum Dots as strain- and metabolism-specific microbiological labels. *Applied and Environmental Microbiology* **2003,** *69,* 4205-4213.

62. Jackson, B.P.; Bugge, D.; Ranville, J.F.; Chen, C.Y. Bioavailability, toxicity, and bioaccumulation of quantum dot nanoparticles to the amphipod Leptocheirus plumulosus. *Environ. Sci. Technol.* **2012,** *46,* 5550-5556.

63. Soldo, D.; Hari, R.; Sigg, L.; Behra, R. Tolerance of Oocystis nephrocytioides to copper: intracellular distribution and extracellular complexation of copper. *Aquatic Toxicology* **2005,** *71,* 307-317.

64. Baun, A.; Sørensen, S.N.; Rasmussen, R.F.; Hartmann, N.B.; Koch, C.B. Toxicity and bioaccumulation of xenobiotic organic compounds in the presence of aqueous suspensions of aggregates of nano-C60. *Aquatic Toxicology* **2008,** *86,* 379-387.

65. Knauer, K.; Sobek, A.; Bucheli, T.D. Reduced toxicity of diuron to the freshwater green alga Pseudokirchneriella subcapitata in the presence of black carbon. *Aquatic Toxicology* **2007,** *83,* 143-148.

66. Thompson, R.C.; Swan, S.H.; Moore, C.J.; vom Saal, F.S. Our plastic age. *Philosophical Transactions of the Royal Society B: Biological Sciences* **2009,** *364,* 1973-1976.

67. Cole, M.; Lindeque, P.; Halsband, C.; Galloway, T.S. Microplastics as contaminants in the marine environment: A review. *Mar. Pollut. Bull.* **2010,** *62,* 2588-2597.

68. Moore, C.J. Synthetic polymers in the marine environment: A rapidly increasing, long-term threat. *Environ. Res.* **2008,** *108,* 131-139.

69. Hansen, J. Draft position statement on plastic debris in marine environments. *Fisheries* **1990,** *15,* 16-17.

70. Laist, D.W. Overview of the biological effects of lost and discarded plastic debris in the marine environment. *Mar. Pollut. Bull.* **1987,** *18,* 319-326.

71. Pruter, A.T. Sources, quantities and distribution of persistent plastics in the marine environment. *Mar. Pollut. Bull.* **1987,** *18,* 305-310.

72. Goldberg, E.D. Plasticizing the seafloor: An overview. *Environ. Technol.* **1997,** *18,* 195-201.

73. Goldberg, E.D. The health of the oceans - A 1994 update. *Chem. Ecol.* **1995,** *10,* 3-8.

74. Ryan, P.G. The origin and fate of artefacts stranded on islands in the African sector of the Southern Ocean. *Environmental Conservation* **1987,** *14,* 341-346.

75. Derraik, J.G.B. The pollution of the marine environment by plastic debris: a review. *Mar. Pollut. Bull.* **2002,** *44,* 842-852.

76. Arthur, C.; Baker, J.; Bamford, H. Proceedings of the International Research Workshop on the Occurrence, Effects and Fate of Micro-plastic Marine Debris. *NOAA Technical Memorandum NOS-OR&R-30* **September 9-11, 2008,**

77. Barnes, D.K.A.; Galgani, F.; Thompson, R.C.; Barlaz, M. Accumulation and fragmentation of plastic debris in global environments. *Philosophical Transactions of the Royal Society B: Biological Sciences* **2009,** *364,* 1985-1998.

78. Roy, P.K.; Hakkarainen, M.; Varma, I.K.; Albertsson, A. Degradable polyethylene: Fantasy or reality. *Environ. Sci. Technol.* **2011,** *45,* 4217-4227.

79. Rios, L.M.; Jones, P.R.; Moore, C.; Narayan, U.V. Quantitation of persistent organic pollutants adsorbed on plastic debris from the Northern Pacific Gyre's "eastern garbage patch". *J. Environ. Monit.* **2010,** *12,* 2226-2236.

80. Hopewell, J.; Dvorak, R.; Kosior, E. Plastics recycling: challenges and opportunities. *Philosophical Transactions of the Royal Society B: Biological Sciences* **2009,** *364,* 2115-2126.

81. Laist, D. Impacts of marine debris: entanglement of marine life in marine debris including a comprehensive list of species with entanglement and ingestion records, In *Marine debris: sources, impacts, and solutions. ,* Coe, J.M. and Rogers, D.B., Eds.; Springer Series on Environmental Management. Springer-Verlag: New York, **1997**; Vol.432 pp. 99-139.

82. Gouin, T.; Roche, N.; Lohmann, R.; Hodges, G. A thermodynamic approach for assessing the environmental exposure of chemicals absorbed to microplastic. *Environ. Sci. Technol.* **2011,** *45,* 1466-1472.

83. Ogata, Y.; Takada, H.; Mizukawa, K.; Hirai, H.; Iwasa, S.; Endo, S.; Mato, Y.; Saha, M.; Okuda, K.; Nakashima, A.; Murakami, M.; Zurcher, N.; Booyatumanondo, R.; Zakaria, M.P.; Dung, L.Q.; Gordon, M.; Miguez, C.; Suzuki, S.; Moore, C.; Karapanagioti, H.K.; Weerts, S.; McClurg, T.; Burres, E.; Smith, W.; Velkenburg, M.V.; Lang, J.S.; Lang, R.C.; Laursen, D.; Danner, B.; Stewardson, N.; Thompson, R.C. International pellet watch: Global monitoring of persistent organic pollutants (POPs) in coastal waters. 1. Initial phase data on PCBs, DDTs, and HCHs. *Mar. Pollut. Bull.* **2009,** *58,* 1437-1446.

84. Rios, L.M.; Moore, C.; Jones, P.R. Persistent organic pollutants carried by synthetic polymers in the ocean environment. *Mar. Pollut. Bull.* **2007,** *54,* 1230-1237.

85. Mato, Y.; Isobe, T.; Takada, H.; Kanehiro, H.; Ohtake, C.; Kaminuma, T. Plastic resin pellets as a transport medium for toxic chemicals in the marine environment. *Environ. Sci. Technol.* **2001,** *35,* 318-324.

86. Ashton, K.; Holmes, L.; Turner, A. Association of metals with plastic production pellets in the marine environment. *Mar. Pollut. Bull.* **2010,** *60,* 2050-2055.

87. Davison, P. and Asch, R.G. Plastic ingestion by mesopelagic fishes in the North Pacific Subtropical Gyre. *Mar. Ecol. Prog. Ser.* **2011,** *432,* 173-180.

88. Browne, M.A.; Dissanayake, A.; Galloway, T.S.; Lowe, D.M.; Thompson, R.C. Ingested microscopic plastic translocates to the circulatory system of the mussel, Mytilus edulis (L.). *Environ. Sci. Technol.* **2008,** *42,* 5026-5031.

89. Thompson, R.C.; Olsen, Y.; Mitchell, R.P.; Davis, A.; Rowland, S.J.; John, A.W.G.; McGonigle, D.; Russell, A.E. Lost at sea: Where is all the plastic? *Science* **2004,** *304,* 838-838.

90. Carpenter, E.J.; Anderson, S.J.; Harvey, G.R.; Miklas, H.P.; Peck, B.B. Polystyrene spherules in coastal waters. *Science* **1972,** *178,* 749-750.

91. Murray, F. and Cowie, P.R. Plastic contamination in the decapod crustacean Nephrops norvegicus (Linnaeus, 1758). *Mar. Pollut. Bull.* **2011,** *62,* 1207-1217.

92. Teuten, E.L.; Saquing, J.M.; Knappe, D.R.U.; Barlaz, M.A.; Jonsson, S.; Björn, A.; Rowland, S.J.; Thompson, R.C.; Galloway, T.S.; Yamashita, R.; Ochi, D.; Watanuki, Y.; Moore, C.; Viet, P.H.; Tana, T.S.; Prudente, M.; Boonyatumanond, R.; Zakaria, M.P.; Akkhavong, K.; Ogata, Y.; Hirai, H.; Iwasa, S.; Mizukawa, K.; Hagino, Y.; Imamura, A.; Saha, M.; Takada, H. Transport and release of chemicals from plastics to the environment and to wildlife. *Philosophical Transactions of the Royal Society B: Biological Sciences* **2009,** *364,* 2027-2045.

93. vom Saal, F.S.; Hughes, C. An extensive new literature concerning low-dose effects of Bisphenol A shows the need for a new risk assessment. *Environ. Health Perspect.* **2005,** *113,* 926-933.

94. Teuten, E. L.,Rowland, S.J.; Galloway, T.S.; Thompson, R.C. Potential for plastics to transport hydrophobic contaminants. *Environ. Sci. Technol.* **2007,** *41,* 7759-7764.

95. Browne, M.A.; Galloway, T.S.; Thompson, R.C. Spatial patterns of plastic debris along estuarine shorelines. *Environ. Sci. Technol.* **2010,** *44,* 3404-3409.

96. George, G.A. Weathering of polymers. **Mater. Forum (Australia), 1995,** *19,* 145-161.

97. Boerger, C.M.; Lattin, G.L.; Moore, S.L.; Moore, C.J. Plastic ingestion by planktivorous fishes in the North Pacific Central Gyre. *Mar. Pollut. Bull.* **2010,** *60,* 2275-2278.

98. Frias, J.P.G.L.; Sobral, P.; Ferreira, A.M. Organic pollutants in microplastics from two beaches of the Portuguese coast. *Mar. Pollut. Bull.* **2010,** *60,* 1988-1992.

99. Zitko, V.; Hanlon, M. Another source of pollution by plastics: skin cleaners with plastic scrubbers. *Marine Pollution Bulletin MPNBAZ* **1991,** *22,* 41-42.

100. Gregory, M.R. Plastic 'scrubbers' in hand cleansers: a further (and minor) source for marine pollution identified. *Mar. Pollut. Bull.* **1996,** *32,* 867-871.

101. US-EPA http://www.epa.gov/garbage/pubs/06data.pdf. **2012***,* 7.

102. Browne, M.A.; Crump, P.; Niven, S.J.; Teuten, E.; Tonkin, A.; Galloway, T.; Thompson, R. Accumulation of microplastic on shorelines woldwide: sources and sinks. *Environ. Sci. Technol.* **2011,** *45,* 9175-9179.

103. Hidalgo-Ruz, V.; Gutow, L.; Thompson, R.C.; Thiel, M. Microplastics in the marine environment: A review of the methods used for identification and quantification. *Environ. Sci. Technol.* **2012,** *46,* 3060-3075.

104. Morét-Ferguson, S.; Law, K.L.; Proskurowski, G.; Murphy, E.K.; Peacock, E.E.; Reddy, C.M. The size, mass, and composition of plastic debris in the western North Atlantic Ocean. *Mar. Pollut. Bull.* **2010,** *60,* 1873-1878.

105. Kartar, S.; Abou-Seedo, F.; Sainsbury, M. Polystyrene spherules in the Severn Estuary - A progress report. *Mar. Pollut. Bull.* **1976,** *7,* 52.

106. Carpenter, E.J.; Smith, K.L. Plastics on the Sargasso sea surface. *Science* **1972,** *175,* 1240-1241.

107. Zitko, V. Expanded polystyrene as a source of contaminants *Mar. Pollut. Bull.* **1993,** *26,* 584-585.

108. Minchin, D. Tar pellets and plastics as attachment surfaces for lepadid cirripedes in the North Atlantic Ocean. *Mar. Pollut. Bull.* **1996,** *32,* 855-859.

109. Clark, R.B. *Marine Pollution.* Oxford: Clarendon Press: Oxford, **1997**; Vol. 4, pp. 161.

110. Winston, J.E. Drift plastic—An expanding niche for a marine invertebrate? *Mar. Pollut. Bull.* **1982,** *13,* 348-351.

111. Grassle, J.F.; Lassere, P.; McIntyre, A.D.; Ray, G.C. Marine biodiversity and ecosystem function. *Biology International Special Issue* **1991,** *23,* 1-19.

112. Maynard, A. Nanotechnology: a research strategy for addressing risk. *Woodrow Wilson International Center for Scholars Project on Emerging Nanotechnologies* **2006,** *2012,* http://www.nanotechproject.org/file_download/files/PEN3_Risk.pdf.

113. Fendall, L.S. and Sewell, M.A. Contributing to marine pollution by washing your face: Microplastics in facial cleansers. *Mar. Pollut. Bull.* **2009,** *58,* 1225-1228.

114. Srinivasa, R.M.; Basha, S.; Adimurthy, S.; Ramachandraiah, G. Description of the small plastics fragments in marine sediments along the Alang-Sosiya ship-breaking yard, India. *Estuar. Coast. Shelf Sci.* **2006,** *68,* 656-660.

115. Uitz, J.; Claustre, H.; Gentili, B.; Stramski, D. Phytoplankton class-specific primary production in the world's oceans: Seasonal and inter-annual variability from satellite observations. *Glob. Biogeochem. Cycles* **2010,** *24,* 3016-3035.

116. Brown, D.M.; Wilson, M.R.; MacNee, W.; Stone, V. Donaldson, size-dependent pro-inflammatory effects of ultrafine polystyrene particles: a role for surface area and oxidative stress in the enhanced activity of ultrafines. *Toxicol. Appl. Pharmocol.* **2001,** *175,* 191-199.

117. Prentice, T. and Reinders, L.T. The world health report 2007: a safer future : global public health security in the 21st century. *World Health Organization.* **2007,** 1-96.

118. Baker, R.W. Ultrafiltration, In *Membrane Technology and Applications,* Esposito, R., Ed.; McGraw-Hill: New Jersey, **2000**; pp. 267.

119. Baker, R.W. Reverse Osmosis, In *Membrane Technology and Applications,* Esposito, R., Ed.; McGraw-Hill: New Jersey, **2000**; pp. 202.

120. Van, d.B.; Lejon, L.; Vandecasteele, C. Reuse, Treatment, and discharge of the concentrate of pressure-driven membrane processes. *Environ. Sci. Technol.* **2003,** *37,* 3733-3738.

121. Mohsen, M.S.; Jaber, J.O.; Afonso, M.D. Desalination of brackish water by nanofiltration and reverse osmosis. *Desalination* **2003,** *157,* 167.

122. Committee to Review the Desalination and Water Purification Technology. Roadmap Review of the Desalination and Water Purification Technology Roadmap. *National Research Council of the National Academies* **2004,** 1-73.

123. Zhang, W.; Elliott, D.W. Applications of iron nanoparticles for groundwater remediation. *Remediation Journal* **2006,** *16,* 7-21.

124. Lowry, G.V. Nanomaterials for groundwater remediation, In *Environmental Nanotechnology: Applications and Impacts of Nanomaterials,* Wiesner, M.R. and Bottero, J., Eds.; McGraw-Hill: New Jersey, **2007**; pp. 298.

125. Liu, Y.; Majetich, S.A.; Tilton, R.D.; Sholl, D.S.; Lowry, G.V. TCE dechlorination rates, pathways, and efficiency of nanoscale iron particles with different properties. *Environ. Sci. Technol.* **2005,** *39,* 1338-1345.

126. Nutt, M.O.; Heck, K.N.; Alvarez, P.; Wong, M.S. Improved Pd-on-Au bimetallic nanoparticle catalysts for aqueous-phase trichloroethene hydrodechlorination. *Applied Catalysis B: Environmental* **2006,** *69,* 115-125.

127. Tungittiplakorn, W.; Lion, L.W.; Cohen, C.; Kim, J. Engineered polymeric nanoparticles for soil remediation. *Environ. Sci. Technol.* **2004,** *38,* 1605-1610.

128. Zhang, W. Nanoscale iron particles for environmental remediation: An overview. *Journal of Nanoparticle Research* **2003,** *5,* 323-332.

129. Moore, A.M.; De Leon, C.H.; Young, T.M. Rate and extent of aqueous perchlorate removal by iron surfaces. *Environ. Sci. Technol.* **2003,** *37,* 3189-3198.

130. Cao, J.; Elliott, D.; Zhang, W. Perchlorate reduction by nanoscale iron particles. *Journal of Nanoparticle Research* **2005,** *7,* 499-506.

131. Databases of innovative technologies. *US-EPA* **2003,** *2012,* <http://www.epa.gov/tio/databases/>.

132. Pisanic II, T.R.; Blackwell, J.D.; Shubayev, V.I.; Fiñones, R.R.; Jin, S. Nanotoxicity of iron oxide nanoparticle internalization in growing neurons. *Biomaterials* **2007,** *28,* 2572-2581.

133. Valls, M.; de Lorenzo, V. Exploiting the genetic and biochemical capacities of bacteria for the remediation of heavy metal pollution. *FEMS Microbiol. Rev.* **2002,** *26,* 327-338.

134. Kirschling, T.L.; Gregory, K.B.; Minkley, E.G.J.; Lowry, G.V.; Tilton, R.D. Impact of nanoscale zero valent iron on geochemistry and microbial populations in trichloroethylene contaminated aquifer materials. *Environ. Sci. Technol.* **2010,** *44,* 3474-3480.

135. Adesina, A.A. Industrial exploitation of photocatalysis: progress, perspectives and prospects. *Catalysis Surveys from Asia* **2004,** *8,* 265-273.

136. Chong, M.N.; Jin, B.; Chow, C.W.K.; Saint, C. Recent developments in photocatalytic water treatment technology: A review. *Water Res.* **2010,** *44,* 2997-3027.

137. Chitose, N.; Ueta, S.; Seino, S.; Yamamoto, T.A. Radiolysis of aqueous phenol solutions with nanoparticles. 1. Phenol degradation and TOC removal in solutions containing TiO_2 induced by UV, γ-ray and electron beams. *Chemosphere* **2003,** *50,* 1007-1013.

138. Wu, P.; Xie, R.; Shang, J.K. Enhanced visible-light photocatalytic disinfection of bacterial spores by palladium-modified nitrogen-doped titanium oxide. *J Am Ceram Soc* **2008,** *91,* 2957-2962.

139. Baker, C.; Pradhan, A.; Pakstis, L.; Pochan Darrin, J.; Shah, I.S. Synthesis and antibacterial properties of silver nanoparticles. *J. Nanosci. Nanotechnol.* **2005,** *5,* 244-249.

140. Savage, N. and Diallo, M.S. Nanomaterials and water Purification: Opportunities and challenges. *Journal of Nanoparticle Research* **2005,** *7,* 331-342.

141. Pan, B. and Xing, B. Competitive and complementary adsorption of bisphenol A and 17α-ethinyl estradiol on carbon nanomaterials. *J. Agric. Food Chem.* **2010,** *58,* 8338-8343.

142. Li, Y.; Ding, J.; Luan, Z.; Di, Z.; Zhu, Y.; Xu, C.; Wu, D.; Wei, B. Competitive adsorption of Pb^{2+}, Cu^{2+} and Cd^{2+} ions from aqueous solutions by multiwalled carbon nanotubes. *Carbon* **2003,** *41,* 2787-2792.

143. Peng, X.; Luan, Z.; Ding, J.; Di, Z.; Li, Y.; Tian, B. Ceria nanoparticles supported on carbon nanotubes for the removal of arsenate from water. *Mater Lett* **2005,** *59,* 399-403.

144. Li, Y.; Luan, Z.; Xiao, X.; Zhou, X.; Xu, C.; Wu, D.; Wei, B. Removal of Cu^{2+} ions from aqueous solutions by carbon nanotubes. *Adsorpt. Sci. Technol.* **2003,** *21,* 475-485.

145. Kang, S.; Herzberg, M.; Rodrigues, D.F.; Elimelech, M. Antibacterial effects of carbon nanotubes: Size does matter! *Langmuir* **2008,** *24,* 6409-6413.

146. Upadhyayula, V.K.K.; Deng, S.; Mitchell, M.C.; Smith, G.B. Application of carbon nanotube technology for removal of contaminants in drinking water: A review. *Sci. Total Environ.* **2009,** *408,* 1-13.

147. Zhang, S.; Shao, T.; Kose, H.S.; Karanfil, T. Adsorption of aromatic compounds by carbonaceous adsorbents: A comparative study on granular activated carbon, activated carbon fiber, and carbon nanotubes. *Environ. Sci. Technol.* **2010,** *44,* 6377-6383.

148. Hummer, G.; Rasaiah, J.C.; Noworyta, J.P. Water conduction through the hydrophobic channel of a carbon nanotube. *Nature* **2001,** *414,* 188-190.

149. Holt, J.K.; Park, H.G.; Wang, Y.; Stadermann, M.; Artyukhin, A.B.; Grigoropoulos, C.P.; Noy, A.; Bakajin, O. Fast mass transport through sub-2-nanometer carbon nanotubes. *Science* **2006,** *312,* 1034-1037.

150. Fornasiero, F.; Park, H.G.; Holt, J.K.; Stadermann, M.; Grigoropoulos, C.P.; Noy, A.; Bakajin, O. Ion exclusion by sub-2-nm carbon nanotube pores. *PNAS* **2008,** *105,* 17250-17255.

151. Cheng, X.; Kan, A.T.; Tomson, M.B. Naphthalene adsorption and desorption from aqueous C60 fullerene. *J. Chem. Eng. Data* **2004,** *49,* 675-683.

152. Ãlvarez-Ayuso, E.; Garcia-Sanchez, A.; Querol, X. Purification of metal electroplating waste waters using zeolites. *Water Res.* **2003,** *37,* 4855-4862.

153. Yantasee, W.; Lin, Y.; Fryxell, G.E.; Busche, B.J.; Birnbaum, J.C. Removal of heavy metals from aqueous solution using novel nanoengineered sorbents: self-assembled carbamoylphosphonic acids on mesoporous silica. *Sep. Sci. Technol.* **2003,** *38,* 3809-3825.

154. Lin, Y.; Fiskum, S.K.; Yantasee, W.; Wu, H.; Mattigod, S.V.; Vorpagel, E.; Fryxell, G.E.; Raymond, K.N.; Xu, J. Incorporation of hydroxypyridinone ligands into self-assembled monolayers on mesoporous supports for selective actinide sequestration. *Environ. Sci. Technol.* **2005,** *39,* 1332-1337.

155. Srivastava, A.; Srivastava, O.N.; Talapatra, S.; Vajtai, R.; Ajayan, P.M. Carbon nanotube filters. *Nat Mater* **2004,** *3,* 610-614.

156. Meyer, D.E.; Wood, K.; Bachas, L.G.; Bhattacharyya, D. Degradation of chlorinated organics by membrane-immobilized nanosized metals. *Environ. Prog.* **2004,** *23,* 232-242.

157. Zodrow, K.; Brunet, L.; Mahendra, S.; Li, D.; Zhang, A.; Li, Q.; Alvarez, P.J.J. Polysulfone ultrafiltration membranes impregnated with silver nanoparticles show improved biofouling resistance and virus removal. *Water Res.* **2009,** *43,* 715-723.

158. Ulbricht, M.; Belfort, G. Surface modification of ultrafiltration membranes by low temperature plasma II. Graft polymerization onto polyacrylonitrile and polysulfone. *J. Membr. Sci.* **1996,** *111,* 193-215.

159. Carroll, T.; Booker, N.A.; Meier-Haack, J. Polyelectrolyte-grafted microfiltration membranes to control fouling by natural organic matter in drinking water. *J. Membr. Sci.* **2002,** *203,* 3-13.

160. Rasul, S.B.; Munir, A.K.M.; Hossain, Z.A.; Khan, A.H.; Alauddin, M.; Hussam, A. Electrochemical measurement and speciation of inorganic arsenic in groundwater of Bangladesh. *Talanta* **2002,** *58,* 33-43.

161. Chen, Z.; Akter, K.F.; Rahman, M.M.; Naidu, R. Speciation of arsenic by ion chromatography inductively coupled plasma mass spectrometry using ammonium eluents. *Journal of Separation Science* **2006,** *29,* 2671-2676.

162. Frechet, J.M.J.; Tomalia, D.A. *Dendrimers and Other Dendrtitic Polymers.* Wiley Series in Polymer Science; Wiley: Chichester, England, **2001**; pp. 648.

163. Diallo, M.S. Water treatment by dendrimer enhanced filtration. *United States Patent* **2008,** *11/182,314,* 1-40.

164. Halford, B. Dendrimers branch out. *Chemical and Engineering News* **2005,** *83,* 30-36.

165. Ottaviani, M.F.; Favuzza, P.; Bigazzi, M.; Turro, N.J.; Jockusch, S.; Tomalia, D.A. A TEM and EPR investigation of the competitive binding of uranyl ions to Starburst dendrimers and liposomes: Potential use of dendrimers as uranyl ion sponges. *Langmuir* **2000,** *16,* 7368-7372.

166. Lard, M.; Kim, S.H.; Lin, S.; Bhattacharya, P.; Ke, P.C.; Lamm, M.H. Fluorescence resonance energy transfer between phenanthrene and PAMAM dendrimers. *Phys. Chem. Chem. Phys.* **2010,** *12,* 9285-9291.

167. Scott, R.W.J.; Wilson, O.M.; Crooks, R.M. Synthesis, characterization, and applications of dendrimer-encapsulated nanoparticles. *J Phys Chem B* **2005,** *109,* 692-704.

168. Balogh, L.; Swanson, D.R.; Tomalia, D.A.; Hagnauer, G.L.; McManus, A.T. Dendrimer-silver complexes and nanocomposites as antimicrobial agents. *Nano Lett.* **2001,** *1,* 18-21.

169. Diallo, M.S.; Christie, S.; Swaminathan, P.; Balogh, L.; Shi, X.; Um, W.; Papelis, C.; Goddard, W.A.; Johnson, J.H. Dendritic chelating agents. 1. Cu(II) binding to ethylene diamine core poly(amidoamine) dendrimers in aqueous solutions. *Langmuir* **2004,** *20,* 2640-2651.

170. Diallo, M.S.; Christie, S.; Swaminathan, P.; Johnson, J.H.; Goddard, W.A. Dendrimer enhanced ultrafiltration. 1. Recovery of Cu(II) from aqueous solutions using PAMAM dendrimers with ethylene diamine core and terminal NH_2 groups. *Environ. Sci. Technol.* **2005,** *39,* 1366-1377.

171. Lee, C.C.; MacKay, J.A.; Frechet, J.M.J.; Szoka, F.C. Designing dendrimers for biological applications. *Nat Biotech* **2005,** *23,* 1517-1526.

172. Mortimer, M.; Kasemets, K.; Heinlaan, M.; Kurvet, I.; Kahru, A. High throughput kinetic Vibrio fischeri bioluminescence inhibition assay for study of toxic effects of nanoparticles. *Toxicology in Vitro* **2008,** *22,* 1412-1417.

173. Tang, M.X.; Redemann, C.T.; Szoka, F.C. In vitro gene delivery by degraded polyamidoamine dendrimers. *Bioconjugate Chem.* **1996,** *7,* 703-714.

174. Rossetti, R.; Nakahara, S.; Brus, L.E. Quantum size effects in the redox potentials, resonance Raman-spectra, and electronic-spectra of Cds crystallites in aqueous-solution. *J. Chem. Phys.* **1983,** *79,* 1086-1088.

175. Eychmuller, A. Structure and photophysics of semiconductor nanocrystals. *J Phys Chem B* **2000,** *104,* 6514-6528.

176. Jamieson, T.; Bakhshi, R.; Petrova, D.; Pocock, R.; Imani, M.; Seifalian, A.M. Biological applications of quantum dots. *Biomaterials* **2007,** *28,* 4717-4732.

177. Lin, S.; Bhattacharya, P.; Rajapakse, N.C.; Brune, D.E.; Ke, P.C. Effects of quantum dots adsorption on algal photosynthesis. *J. Phys. Chem. C* **2009,** *113,* 10962-10966.

178. Bhattacharya, P.; Lin, S.; Turner, J.P.; Ke, P.C. Physical adsorption of charged plastic nanoparticles affects algal photosynthesis. *J. Phys. Chem. C* **2010,** *114,* 16556-16561.

179. Nel, A.; Xia, T.; Mädler, L.; Li, N. Toxic potential of materials at the nanolevel. *Science* **2006,** *311,* 622-627.

180. Ke, P.C. and Qiao, R. Carbon nanomaterials in biological systems. *Journal of Physics: Condensed Matter* **2007,** *19,* 373101-1-25.

181. Maynard, A.D.; Aitken, R.J.; Butz, T.; Colvin, V.; Donaldson, K.; Oberdörster, G.; Philbert, M.A.; Ryan, J.; Seaton, A.; Stone, V.; Tinkle, S.S.; Tran, L.; Walker, N.J.; Warheit, D.B. Safe handling of nanotechnology. *Nature* **2006,** *444,* 267-269.

182. Alivisatos, P. The use of nanocrystals in biological detection. *Nat Biotech* **2004,** *22,* 47-52.

183. Yu, W.W.; Chang, E.; Drezek, R.; Colvin, V.L. Water-soluble quantum dots for biomedical applications. *Biochem. Biophys. Res. Commun.* **2006,** *348,* 781-786.

184. Klostranec, J.M. and Chan, W.C.W. Quantum dots in biological and biomedical research: recent progress and present challenges. *Adv Mater* **2006,** *18,* 1953-1964.

185. Xing, Y.; Chaudry, Q.; Shen, C.; Kong, K.Y.; Zhau, H.E.; Chung, L.W.; Petros, J.A.; O'Regan, R.M.; Yezhelyev, M.V.; Simons, J.W.; Wang, M.D.; Nie, S. Bioconjugated quantum dots for multiplexed and quantitative immunohistochemistry. *Nature Protocols* **2007,** *2,* 1152-1165.

186. Mortensen, L.J.; Oberdörster, G.; Pentland, A.P.; DeLouise, L.A. In vivo skin penetration of quantum dot nanoparticles in the murine model: The effect of UVR. *Nano Lett.* **2008,** *8,* 2779-2787.

187. Smith, B.R.; Cheng, Z.; De, A.; Koh, A.L.; Sinclair, R.; Gambhir, S.S. Real-time intravital imaging of RGD−quantum dot binding to luminal endothelium in mouse tumor neovasculature. *Nano Lett.* **2008,** *8,* 2599-2606.

188. Xie, H.; Li, Y.; Kagawa, H.K.; Trent, J.D.; Mudalige, K.; Cotlet, M.; Swanson, B.I. An intrinsically fluorescent recognition ligand scaffold based on chaperonin protein and semiconductor quantum-dot conjugates. *Small* **2009,** *5,* 1036-1042.

189. Hannah, W. and Thompson, P.B. Nanotechnology, risk and the environment: a review. *J. Environ. Monit.* **2008,** *10,* 291-300.

190. Zhu, H.; Han, J.; Xiao, J.Q.; Jin, Y. Uptake, translocation, and accumulation of manufactured iron oxide nanoparticles by pumpkin plants. *J. Environ. Monit.* **2008,** *10,* 713-717.

191. Etxeberrie, E.; Gonzalez, P.; Baroja-Fernandez, E.; Romero, J.O. Fluid phase endocytic uptake of artificial nano-spheres and fluorescent quantum dots by sycamore cultured cells: evidence for the distribution of solutes to different intracellular compartments. *Plant Signaling Behavior* **2006,** *1,* 196-200.

192. Liu, Q.; Chen, B.; Wang, Q.; Shi, X.; Xiao, Z.; Lin, J.; Fang, x. Carbon nanotubes as molecular transporters for walled plant cells. *Nano Lett.* **2009,** *9,* 1007-1010.

193. Lu, C.M.; Zhang, C.Y.; Wen, J.Q.; Wu, G.R.; Tao, M.X. Research of the effect of nanometer materials on germination and growth enhancement of *Glycine max* and its mechanism. *Soybean Sci* **2002,** *21,* 168-172.

194. Zheng, L.; Hong, F.; Lu, S.; Liu, C. Effect of nano-TiO_2 on strength of naturally aged seeds and growth of spinach. *Biological Trace Element Research* **2005,** *104,* 83-91.

195. Govorov, A.O. and Carmeli, I. Hybrid structures composed of photosynthetic system and metal nanoparticles: plasmon enhancement effect. *Nano Lett.* **2007,** *7,* 620-625.

196. Yang, L. and Watts, D.J. Particle surface characteristics may play an important role in phytotoxicity of alumina nanoparticles. *Toxicol. Lett.* **2005,** *158,* 122-132.

197. Lin, S. and Chen, D. Synthesis of water-soluble blue photoluminescent silicon nanocrystals with oxide surface passivation. *Small* **2009,** *5,* 72-76.

198. Kloepfer, J.A.; Mielke, R.E.; Nadeau, J.L. Uptake of CdSe and CdSe/ZnS quantum dots into bacteria via purine-dependent mechanisms. *Applied and Environmental Microbiology* **2005,** *71,* 2548-2557.

199. Demchick, P. and Koch, A.L. The permeability of the wall fabric of Escherichia coli and Bacillus subtilis. *Journal of Bacteriology* **1996,** *178,* 768-773.

200. Dabbousi, B.O.; RodriguezViejo, J.; Mikulec, F.V.; Heine, J.R.; Mattoussi, H.; Ober, R.; Jensen, K.F.; Bawendi, M.G. (CdSe)ZnS core-shell quantum dots: Synthesis and characterization of a size series of highly luminescent nanocrystallites. *J Phys Chem B* **1997,** *101,* 9463-9475.

201. Stoimenov, P.K.; Klinger, R.L.; Marchin, G.L.; Klabunde, K.J. Metal oxide nanoparticles as bactericidal agents. *Langmuir* **2002,** *18,* 6679-6686.

202. Petruska, M.A.; Bartko, A.P.; Klimov, V.I. An amphiphilic approach to nanocrystal quantum dot−titania nanocomposites. *J. Am. Chem. Soc.* **2004,** *126,* 714-715.

203. Haram, S.K.; Quinn, B.M.; Bard, A.J. Electrochemistry of CdS anoparticles: A correlation between optical and electrochemical band gaps. *J. Am. Chem. Soc.* **2001,** *123,* 8860-8861.

204. Hoyer, P. and Weller, H. Size-dependent redox potentials of quantized zinc oxide measured with an optically transparent thin layer electrode. *Chemical Physics Letters* **1994,** *221,* 379-384.

205. Plastics-Europe. Analysis of plastics production demand and recovery in Europe for 2008. *Association of Plastics Manufacturers* **2008,** 1-20.

206. Gregory, M.R.; Kirk, R.M.; Mabin, M.C.G. Pelagic tar, oil, plastics and other litter in surface waters of the New Zealand sector of the Southern Ocean and on Ross Dependency shores. *NZ Antarct Record* **1984,** *6,* 12-28.

207. Garrity, S.D. and Levings, S.C. Marine debris along the Caribbean coast of Panama. *Mar. Pollut. Bull.* **1993,** *26,* 317-324.

208. Benton, T.G. From castaways to throwaways: marine litter in the Pitcairn Islands. *Biol. J. Linn. Soc.* **1995,** *56,* 415-422.

209. Ye, S. and Andrady, A.L. Fouling of floating plastic debris under Biscayne Bay exposure conditions. *Mar. Pollut. Bull.* **1991,** *22,* 608-613.

210. Silverman, J. <http://science.howstuffworks.com/great-pacific-garbagepatch.htm.> **2007**.

211. Ward, E.J. and Shumway, S.E. Separating the grain from the chaff: particle selection in suspension- and deposit-feeding bivalves. *J. Exp. Mar. Biol. Ecol.* **2004,** *300,* 83-130.

212. Olivier, V.; Rivière, C.; Hindié, M.; Duval, J.-.; Bomila-Koradjim, G.; Nagel, M.-. Uptake of polystyrene beads bearing functional groups by macrophages and fibroblasts. *Colloids and Surfaces B Biointerfaces* **2004,** *33,* 23-31.

213. <http://www.americanchemistry.com/s_plastics/sec_pfpg.asp?CID=1432&DID=5224.> **2012**

214. Goodenough, U.W.; Gebhart, B.; Mecham, R.P.; Heuser, J.E. Crystals of the Chlamydomonas reinhardtii cell wall: polymerization, depolymerization, and purification of glycoprotein monomers. *The Journal of Cell Biology* **1986,** *103,* 405-417.

215. Davis, R.D. and Plaskitt, A. Genetic and structural analysis of cell-wall formation in Chlamydomonas reinhardtii. *Genet. Res. Camb.* **1971,** *17,* 33-43.

216. Zelitch, I. *Photosynthesis, Photorespiration and Plant Productivity.* Academic Press: London, 1971; pp. 275.

217. Adams, M. *Superfoods for Optimum Health: Chlorella and Spirulina.* Consumer Wellness Research Center: pp. 1-39.

218. Smith, E.F. and Lefebvre, P.A. PF16 encodes a protein with armadillo repeats and localizes to a single microtubule of the central apparatus in Chlamydomonas flagella. *The Journal of Cell Biology* **1996,** *132,* 359-370.

219. Roberts, K. and Hills, G.J. The crystalline glycoprotein cell wall of the green alga Chlorogonium elongatum: a structural analysis. *Journal of Cell Science* **1976,** *21,* 59-71.

220. Slejko, F.L. *Adsorption technology. A step-by-step approach to process evaluation and application.* Marcel dekker: New York, 1985;

221. Ribeiro, M.; Lourenço, P.; Monteiro, J.; Ferreira-Dias, S. Kinetics of selective adsorption of impurities from a crude vegetable oil in hexane to activated earths and carbons. *European Food Research and Technology* **2001,** *213,* 132-138.

222. Hund-Rinke, K. and Simon, M. Ecotoxic effect of photocatalytic active nanoparticles (TiO_2) on algae and daphnids. *Environmental Science and Pollution Research* **2006,** *13,* 225-232.

223. Fujiwara, K.; Suematsu, H.; Kiyomiya, E.; Aoki, M.; Sato, M.; Moritoki, N. Size-dependent toxicity of silica nano-particles to Chlorella kessleri. *Journal of Environmental Science and Health, Part A* **2008,** *43,* 1167-1173.

224. Aruoja, V.; Dubourguier, H.C.; Kasemets, K.; Kahru, A. Toxicity of nanoparticles of CuO, ZnO and TiO_2 to microalgae Pseudokirchneriella subcapitata. *Sci. Total Environ.* **2009,** *407,* 1461-1468.

225. Morrison, S.S.; Mullineaux, C.W.; Ashby, M.K. The influence of acetyl phosphate on DspA signalling in the Cyanobacterium *Synechocystis* sp. PCC6803. *BMC Microbiol.* **2005,** *5,* 47-54.

226. Frense, D.; Muller, A.; Beckmann, D. Detection of environmental pollutants using optical biosensor with immobilized algae cells. *Sens. Actuator B-Chem.* **1998,** *51,* 256-260.

227. Lin, S.; Keskar, G.; Wu, Y.; Wang, X.; Mount, A.S.; Klaine, S.J.; Moore, J.M.; Rao, A.M.; Ke, P.C. Detection of phospholipid-carbon nanotube translocation using fluorescence energy transfer. *Appl. Phys. Lett.* **2006,** *89,* 143118-1-3.

228. Weiss, S. Fluorescence spectroscopy of single biomolecules. *Science* **1999,** *283,* 1676-1683.

229. Stryer, L. and Haugland, R.P. Energy transfer: a spectroscopic ruler. *PNAS* **1967,** *58,* 719-726.

230. McCormick, C.L.; Callais, P.A.; Hutchinson, B.H. Solution studies of cellulose in lithium chloride and N,N-dimethylacetamide. *Macromolecules* **1985,** *18,* 2394-2401.

231. Suto, S.; Nishibori, W.; Kudo, K.; Karasawa, M. Lyotropic liquid crystalline solutions of hydroxypropyl cellulose in water: Effect of salts on the turbidity and viscometric behavior. *J Appl Polym Sci* **1989,** *37,* 737-749.

232. Dong, X.M.; Kimura, T.; Revol, J.-.; Gray, D.G. Effects of Ionic Strength on the isotropic-chiral nematic phase transition of suspensions of cellulose crystallites. *Langmuir* **1996,** *12,* 2076-2082.

233. Halliwell, B. and Gutteridge, J.M.C. *Free Radicals in Biology and Medicine.* Oxford University Press: New York, **1999**; Vol. 3, pp. 936.

234. Pinto, E.; Sigaud-kutner, T.C.S.; Leitão, M.A.S.; Okamoto, O.K.; Morse, D.; Colepicolo, P. Heavy-metal induced oxidative stress in algae. *J. Phycol.* **2003,** *39,* 1008-1018.

235. Liu, W.; Au, D.W.T.; Anderson, D.M.; Lam, P.K.S.; Wu, R.S.S. Effects of nutrients, salinity, pH and light:dark cycle on the production of reactive oxygen species in the alga Chattonella marina. *J. Exp. Mar. Biol. Ecol.* **2007,** *346,* 76-86.

236. Allan, A.C. and Fluhr, R. Two distinct sources of elicited reactive oxygen species in tobacco epidermal cells. *The Plant Cell Online* **1997,** *9,* 1559-1572.

237. Yahraus, T.; Chandra, S.; Legendre, L.; Low, P.S. Evidence for a mechanically induced oxidative burst. *Plant Physiology* **1995,** *109,* 1259-1266.

238. Vowells, S.J.; Sekhsaria, S.; Malech, H.L.; Shalit, M.; Fleisher, T.A. Flow cytometric analysis of the granulocyte respiratory burst - a comparison study of fluorescent-probes. *J. Immunol. Methods* **1995,** *178,* 89-97.

239. Helms, B. and Meijer, E.W. Dendrimers at work. *Science* **2006,** *313,* 929-930.

240. Malik, N.; Wiwattanapatapee, R.; Klopsch, R.; Lorenz, K.; Frey, H.; Weener, J.W.; Meijer, E.W.; Paulus, W.; Duncan, R. Dendrimers: Relationship between structure and biocompatibility in vitro, and preliminary studies on the biodistribution of 125I-labelled polyamidoamine dendrimers in vivo. *J. Controlled Release* **2000,** *65,* 133-148.

241. Diallo, M.S.; Arasho, W.; Johnson, J.H.; Goddard III, W.A. Dendritic chelating agents. 2. U(VI) binding to poly(amidoamine) and poly(propyleneimine) dendrimers in aqueous solutions. *Environ. Sci. Technol.* **2008,** *42,* 1572-1579.

242. Diallo, M.S.; Falconer, K.; Johnson, J.H.; Goddard III, W.A. Dendritic anion hosts: Perchlorate uptake by G5-NH_2 poly(propyleneimine) dendrimer in water and model electrolyte solutions. *Environ. Sci. Technol.* **2007,** *41,* 6521-6527.

243. Haensler, J. and Szoka, F.C. Polyamidoamine cascade polymers mediate efficient transfection of cells in culture. *Bioconjugate Chem.* **1993,** *4,* 372-379.

244. Tang, M.X.; Redemann, C.T.; Szoka, F.C. In vitro gene delivery by degraded polyamidoamine dendrimers. *Bioconjugate Chem.* **1996,** *7,* 703-714.

245. Malik, N.; Duncan, R.; Tomalia, D.A.; Esfand, R. Dendritic-antineoplastic drug delivery system. **2006,** US2006700512 4.

246. Maiti, P.K.; Cagin, T.; Wang, G.; Goddard, W.A. Structure of PAMAM dendrimers: Generations 1 through 11. *Macromolecules* **2004,** *37,* 6236-6254.

247. Maiti, P.K.; Cagin, T.; Lin, S.-.; Goddard, W.A. Effect of solvent and pH on the structure of PAMAM dendrimers. *Macromolecules* **2005,** *38,* 979-991.

248. Arkas, M.; Tsiourvas, D.; Paleos, C.M. Functional dendrimeric "Nanosponges" for the removal of polycyclic aromatic hydrocarbons from water. *Chem. Mater.* **2003,** *15,* 2844-2847.

249. Meijer, E.W. and van Genderen, M.H.P. Chemistry: Dendrimers set to self-destruct. *Nature* **2003,** *426,* 128-129.

250. Xu, Y. and Zhao, D. Removal of lead from contaminated soils using poly(amidoamine) dendrimers. *Ind Eng Chem Res* **2006,** *45,* 1758-1765.

251. Diallo, M.S.; Balogh, L.; Shafagati, A.; Johnson, J.H.; Goddard, W.A.; Tomalia, D.A. Poly(amidoamine) dendrimers: A new class of high capacity chelating agents for Cu(II) ions. *Environ. Sci. Technol.* **1999,** *33,* 820-824.

252. Zhou, L.; Russell, D.H.; Zhao, M.; Crooks, R.M. Characterization of poly(amidoamine) dendrimers and their complexes with Cu^{2+} by matrix-assisted laser desorption ionization mass spectrometry. *Macromolecules* **2001,** *34,* 3567-3573.

253. Lard, M.; Kim, S.H.; Lin, S.; Bhattacharya, P.; Ke, P.C.; Lamm, M.H. Fluorescence resonance energy transfer between phenanthrene and PAMAM dendrimers. *Phys. Chem. Chem. Phys.* **2010,** *12,* 9285-9291.

254. <http://en.wikipedia.org/wiki/Solubility_table.> **2012**

255. Karapanagioti, H.K. Removal of phenanthrene from saltwater solutions using activated carbon. *Desalination* **2007,** *210,* 274-280.

256. United States Environmental Protection Agency. Drinking Water Contaminants. *http://water. epa. gov/drink/contaminants/#content* **Jun 06, 2012**

257. United States Environmental Protection Agency. Phenanthrene. <*http://www. epa. gov/osw/hazard/wastemin/minimize/factshts/phenanth. pdf*> **2012**

258. Nitrate and Nitrite Poisoning: Introduction. *The Merck Veterinary Manual* **2011**, *2012,* <http://www.merckvetmanual.com/mvm/index.jsp?cfile=htm/bc/212300.htm.>

259. Taki, M.; Iyoshi, S.; Ojida, A.; Hamachi, I.; Yamamoto, Y. Development of highly sensitive fluorescent probes for detection of intracellular copper(I) in living systems. *J. Am. Chem. Soc.* **2010,** *132,* 5938-5939.

260. Chen, P.; Yang, Y.; Bhattacharya, P.; Wang, P.; Ke, P.C. A tris-dendrimer for hosting diverse chemical species. *J. Phys. Chem. C* **2011,** *115,* 12789-12796.

261. Buffle, J.; Chalmers, R.A.; Masson, M.R.; Midgley, D. *Complexation Reactions in Aquatic Systems. An Analytical Approach.* Ellis Horwood: Chichester, **1988**; pp. 692.

262. Tipping, E. Modelling ion binding by humic acids. *Colloids Surf. Physicochem. Eng. Aspects* **1993,** *73,* 117-131.

263. Santschi, P.H.; Roberts, K.A.; Guo, L. Organic nature of colloidal actinides transported in surface water environments. *Environ. Sci. Technol.* **2002,** *36,* 3711-3719.

264. Hong, S.; Elimelech, M. Chemical and physical aspects of natural organic matter (NOM) fouling of nanofiltration membranes. *J. Membr. Sci.* **1997,** *132,* 159-181.

265. Yiantsios, S.G.; Karabelas, A.J. An experimental study of humid acid and powdered activated carbon deposition on UF membranes and their removal by backwashing. *Desalination* **2001,** *140,* 195-209.

266. Cai, Z.; Benjamin, M.M. NOM fractionation and fouling of low-pressure membranes in microgranular adsorptive filtration. *Environ. Sci. Technol.* **2011,** *45,* 8935-8940.

267. Kanan, A.; Karanfil, T. Formation of disinfection by-products in indoor swimming pool water: The contribution from filling water natural organic matter and swimmer body fluids. *Water Res.* **2011,** *45,* 926-932.

268. Matilainen, A.; Vepsäläinen, M.; Sillanpää, M. Natural organic matter removal by coagulation during drinking water treatment: A review. *Adv. Colloid Interface Sci.* **2010,** *159,* 189-197.

269. Bolto, B.; Gregory, J. Organic polyelectrolytes in water treatment. *Water Res.* **2007,** *41,* 2301-2324.

270. Huang, Q.R.; Dubin, P.L.; Moorefield, C.N.; Newkome, G.R. Counterion binding on charged spheres: Effect of pH and ionic strength on the mobility of carboxyl-terminated dendrimers. *J Phys Chem B* **2000,** *104,* 898-904.

271. Maiti, P.K.; Messina, R. Counterion distribution and z-potential in PAMAM dendrimer. *Macromolecules* **2008,** *41,* 5002-5006.

272. Huimann, S.; Wynveen, A.; Likos, C.N.; Blaak, R. The effects of pH, salt and bond stiffness on charged dendrimers. *Journal of Physics: Condensed Matter* **2010,** *22,* 232101-1-8.

273. Crooks, R.M.; Zhao, M.; Sun, L.; Chechik, V.; Yeung, L.K. Dendrimer-encapsulated metal nanoparticles: Synthesis, characterization, and applications to catalysis. *Acc. Chem. Res.* **2001,** *34,* 181-190.

274. Ottaviani, M.F.; Montalti, F.; Turro, N.J.; Tomalia, D.A. Characterization of Starburst dendrimers by the EPR technique. Copper(II) ions binding full-generation dendrimers. *J Phys Chem B* **1997,** *101,* 158-166.

275. Crooks, R.M.; Zhao, M. Dendrimer-encapsulated Pt nanoparticles: Synthesis, characterization, and applications to catalysis. *Adv Mater* **1999,** *11,* 217-220.

276. Balogh, L. and Tomalia, D.A. Poly(Amidoamine) dendrimer-templated nanocomposites. 1. Synthesis of zerovalent copper nanoclusters. *J. Am. Chem. Soc.* **1998,** *120,* 7355-7356.

277. Zhao, M.; Sun, L.; Crooks, R.M. Preparation of Cu nanoclusters within dendrimer templates. *J. Am. Chem. Soc.* **1998,** *120,* 4877-4878.

278. Tomisic, V. and Simeon, V. Ion association in aqueous solutions of strong electrolytes: a UV-Vis spectrometric and factor-analytical study. *Phys. Chem. Chem. Phys.* **1999,** *1,* 299-302.

279. Butorac, V.,; Simeon, V.; T., V. Effect of temperature on UV spectra of concentrated $NaNO_3$ aqueous solutions. *Croat. Chem. Acta* **2007,** *80,* 533-539.

280. Lin, S.T.; Maiti, P.K.; Goddard, W.A. Dynamics and thermodynamics of water in PAMAM dendrimers at subnanosecond time scales. *J Phys Chem B* **2005,** *109,* 8663-8672.

281. Jones, M.N. and Bryan, N.D. Colloidal properties of humic substances. *Adv. Colloid Interface Sci.* **1998,** *78,* 1-48.

282. Tomaszewski, J.E.; Schwarzenbach, R. P.; Sander, M. Protein encapsulation by humic substances. *Environ. Sci. Technol.* **2011,** *45,* 6003-6010.

283. Sposito, G. *The Chemistry of Soils.* Oxford University Press: New York, **2008**; Vol. 2, pp. 329-72.

284. Leenheer, J.A. Fractionation techniques for aquatic humic substances, In *HumicSubstances in Soil,Sediment and Water,* Aiken, G.R., McKnight, D.M., Wershaw, R.L. and MacCarthy, P., Eds.; JohnWiley and Sons: New York, **1985**; pp. 409-429.

285. Brownrigg, J.T. and Kenny, J.E. Fluorescence intensities and lifetimes of aromatic hydrocarbons in cyclohexane solution: Evidence of contact charge-transfer interactions with oxygen. *J Phys Chem A* **2009,** *113,* 1049-1059.

286. Clark, C.D. and Zika, R.G. Photochemistry in the Surface Ocean, In *Marine Chemistry: The Handbook of Environmental Chemistry,* D ed.; Wangersky, P.J., Ed.; Springer: New York, **2000**; Vol.5 pp. 8.

287. Lakowicz, J.R. Quenchig of fluorescence, In *Principles of Fluorescence Spectroscopy,* 3rd ed.; Lakowicz, J.R., Ed.; Springer: New York, **2006**; pp. 282.

288. Del Vecchio, R. and Blough, N.V. On the origin of the optical properties of humic substances. *Environ. Sci. Technol.* **2004,** *38,* 3885-3891.

289. Narkis, N. and Rebhun, M. The mechanism of flocculation processes in the presence of humic substances. *J. AWWA* **1975,** *67,* 101-108.

290. Edzwald, J.K.; Half, J.D.; Boak, J.W. Polymer coagulation of humic acid waters. *Journal of the Environmental Engineering Division* **1977,** 979-1000.

291. Glaser, H.T. and Edzwald, J.K. Coagulation and direct filtration of humic substances with polyethylenimine. *Environ. Sci. Technol.* **1979,** *13,* 299-305.

292. Andjelkovic, T.; Perovic, J.; Purenovic, M.; Blagojevic, S.; Nikolic, R.; Andjelkovic, D.; Bojic, A. A direct potentiometric titration study of dissociation of humic acid withselectively blocked functional groups. *Ecl. Quim.* **2006,** *31,* 39-46.

293. Tan, W.F.; Koopal, L.K.; Norde, W. Interaction between humic acid and lysozyme, studied by dynamic light scattering and isothermal titration calorimetry. *Environ. Sci. Technol.* **2009,** *43,* 591-596.

294. Mohan, J. Infrared spectroscopy, In *Organic Spectroscopy: Principles and Applications,* 2nd ed.; Mohan, J., Ed.; Alpha Science: U.K., **2004**; pp. 62.

295. Bhattacharya, P.; Chen, P.; Spano, M.N.; Zhu, L.; Ke, P.C. Copper detection utilizing dendrimer and gold nanowire-induced surface plasmon resonance. *J. Appl. Phys.* **2011,** *109,* 014911-1-6.

296. Taki, M.,; Iyoshi, S.; Ojida, A.; Hamachi, I.; Yamamoto, Y. Development of highly sensitive fluorescent probes for detection of intracellular copper(I) in living systems. *J. Am. Chem. Soc.* **2010,** *132,* 5938-5939.

297. Chan, Y.; Chen, J.; Liu, Q.; Wark, S.E.; Son, D.H.; Batteas, J.D. Ultrasensitive copper(II) detection using plasmon-enhanced and photo-brightened luminescence of CdSe quantum dots. *Anal. Chem.* **2010,** *82,* 3671-3678.

298. Wang, M.; Feng, W.; Shi, J.; Zhang, F.; Wang, B.; Zhu, M.; Li, B.; Zhao, Y.; Chai, Z. Development of a mild mercaptoethanol extraction method for determination of mercury species in biological samples by HPLC–ICP-MS. *Talanta* **2007,** *71,* 2034-2039.

299. Liang, G.-.; Liu, H.-.; Zhang, J.-.; Zhu, J.-. Ultrasensitive Cu^{2+} sensing by near-infrared-emitting CdSeTe alloyed quantum dots. *Talanta* **2010,** *80,* 2172-2176.

300. Dong, B.; Cao, L.; Su, G.; Liu, W.; Qu, H.; Jiang, D. Synthesis and characterization of the water-soluble silica-coated ZnS:Mn nanoparticles as fluorescent sensor for Cu^{2+} ions. *J. Colloid Interface Sci.* **2009,** *339,* 78-82.

301. Ding, L.; Cui, X.; Han, Y.; Lü, F.; Fang, Y. Sensing performance enhancement via chelating effect: A novel fluorescent film chemosensor for copper ions. *J. Photochem. Photobiol. A.* **2007,** *186,* 143-150.

302. White, B.R. and Holcombe, J.A. Fluorescent peptide sensor for the selective detection of Cu^{2+}. *Talanta* **2007,** *71,* 2015-2020.

303. Sumner, J.P.; Westerberg, N.M.; Stoddard, A.K.; Hurst, T.K.; Cramer, M.; Thompson, R.B.; Fierke, C.A.; Kopelman, R. DsRed as a highly sensitive, selective, and reversible fluorescence-based biosensor for both Cu+ and Cu2+ ions. *Biosensors and Bioelectronics* **2006,** *21,* 1302-1308.

304. He, X.; Liu, H.; Li, Y.; Wang, S.; Li, Y.; Wang, N.; Xiao, J.; Xu, X.; Zhu, D. Gold nanoparticle-based fluorometric and colorimetric sensing of copper(II) ions. *Adv Mater* **2005,** *17,* 2811-2815.

305. Zheng, Y.; Orbulescu, J.; Ji, X.; Andreopoulos, F.M.; Pham, S.M.; Leblanc, R.M. Development of fluorescent film sensors for the detection of divalent copper. *J. Am. Chem. Soc.* **2003,** *125,* 2680-2686.

306. Prestel, H.; Gahr, A.; Niessner, R. Detection of heavy metals in water by fluorescence spectroscopy: On the way to a suitable sensor system. *Fresenius' Journal of Analytical Chemistry* **2000,** *368,* 182-191.

307. Birch, D.J.S.; Rolinski, O.J.; Hatrick, D. Fluorescence lifetime sensor of copper ions in water. *Rev. Sci. Instrum.* **1996,** *67,* 2732-2737.

308. Ottaviani, M.F.; Bossmann, S.; Turro, N.J.; Tomalia, D.A. Characterization of starburst dendrimers by the EPR technique. 1. Copper complexes in water solution. *J. Am. Chem. Soc.* **1994,** *116,* 661-671.

309. Bardhan, R.; Grady, N.K.; Cole, J.R.; Joshi, A.; Halas, N.J. Fluorescence enhancement by Au nanostructures: Nanoshells and nanorods. *ACS Nano* **2009,** *3,* 744-752.

310. Zhang, Y.; Aslan, K.; Previte, M.J.R.; Geddes, C.D. Metal-enhanced fluorescence from copper substrates. *Appl. Phys. Lett.* **2007,** *90,* 173116-1-3.

311. Aslan, K.; Leonenko, Z.; Lakowicz, J.; Geddes, C. Annealed silver-island films for applications in metal-enhanced fluorescence: Interpretation in terms of radiating plasmons. *Anal. Biochem.* **2005,** *15,* 643-654.

312. Shang, L. and Dong, S. Silver nanocluster-based fluorescent sensors for sensitive detection of Cu(II). *J. Mater. Chem.* **2008,** *18,* 4636-4640.

313. Gutierrez, E.; Miller, T.C.; Gonzalez-Redondo, J.; Holcombe, J.A. Characterization of immobilized poly-l-aspartate as a metal chelator. *Environ. Sci. Technol.* **1999,** *33,* 1664-1670.

314. Chen, W.; Tu, X.; Guo, X. Fluorescent gold nanoparticles-based fluorescence sensor for Cu^{2+} ions. *Chem. Commun.* **2009,** *13,* 1736-1738.

315. Lin, B.F.; Marullo, R.S.; Robb, M.J.; Krogstad, D.V.; Antoni, P.; Hawker, C.J.; Campos, L.M.; Tirrell, M.V. De Novo design of bioactive protein-resembling nanospheres via dendrimer-templated peptide amphiphile assembly. *Nano Lett.* **2011,** *11,* 3946-3950.

316. Lehn, J.-. Toward complex matter: Supramolecular chemistry and self-organization. *PNAS* **2002,** *99,* 4763-4768.

317. Xu, Y. and Zhao, D. Removal of copper from contaminated soil by use of poly(amidoamine) dendrimers. *Environ. Sci. Technol.* **2005,** *39,* 2369-2375.

318. Tomalia, D.A.; Naylor, A.M.; Goddard, W.A. Starburst dendrimers: Molecular-level control of size, shape, surface chemistry, topology, and flexibility from atoms to macroscopic matter. *Angew Chem Int Ed Engl* **1990,** *29,* 138-175.

319. Narayanan, V. and Newkome, G. Supramolecular chemistry within dendritic structures. *Topics in Current Chemistry* **1998,** *197,* 19-77.

320. Tanis, I. and Karatasos, K. Molecular dynamics simulations of polyamidoamine dendrimers and their complexes with linear poly(ethylene oxide) at different pH conditions: static properties and hydrogen bonding. *Phys. Chem. Chem. Phys.* **2009,** *11,* 10017-10028.

321. Voulgarakis, N.K.; Rasmussen, K.O.; Welch, P.M. Dendrimers as synthetic gene vectors: Cell membrane attachment. *J. Chem. Phys.* **2009,** *130,* 155101-1-5.

322. Smith, P.E.S.; Brender, J.R.; DuÌrr, U.H.N.; Xu, J.; Mullen, D.G.; Banaszak H.l, M.M.; Ramamoorthy, A. Solid-state NMR reveals the hydrophobic-core location of poly(amidoamine) dendrimers in biomembranes. *J. Am. Chem. Soc.* **2010,** *132,* 8087-8097.

323. Kelly, C.V.; Liroff, M.G.; Triplett, L.D.; Leroueil, P.R.; Mullen, D.G.; Wallace, J.M.; Meshinchi, S.; Baker, J.R.; Orr, B.G.; Banaszak H., M.M. Stoichiometry and structure of poly(amidoamine) Dendrimer-'Lipid Complexes. *ACS Nano* **2009,** *3,* 1886-1896.

324. Kukowska-Latallo, J.F.; Bielinska, A.U.; Johnson, J.; Spindler, R.; Tomalia, D.A.; Baker, J.R. Efficient transfer of genetic material into mammalian cells using Starburst polyamidoamine dendrimers. *Proc. Natl. Acad. Sci. U. S. A.* **1996,** *93,* 4897-4902.

325. Hong, S.; Rattan, R.; Majoros, I.J.; Mullen, D.G.; Peters, J.L.; Shi, X.; Bielinska, A.U.; Blanco, L.; Orr, B.G.; Baker, J.R.; Holl, M.M.B. The role of ganglioside GM1 in cellular internalization mechanisms of poly(amidoamine) dendrimers. *Bioconjugate Chem.* **2009,** *20,* 1503-1513.

326. Naha, P.C.; Davoren, M.; Casey, A.; Byrne, H.J. An ecotoxicological study of poly(amidoamine) dendrimers-toward quantitative structure activity relationships. *Environ. Sci. Technol.* **2009,** *43,* 6864-6869.

327. Jevprasesphant, R.; Penny, J.; Jalal, R.; Attwood, D.; McKeown, N.B.; D'Emanuele, A. The influence of surface modification on the cytotoxicity of PAMAM dendrimers. *Int. J. Pharm.* **2003,** *252,* 263-266.

328. Bosi, S.; Da Ros, T.; Spalluto, G.; Prato, M. Fullerene derivatives: an attractive tool for biological applications. *Eur. J. Med. Chem.* **2003,** *38,* 913-923.

329. Bakry, R.; Vallant, R.M.; Najam-ul-Haq, M.; Rainer, M.; Szabo, Z.; Huck, C.W.; Bonn, G.K. Medicinal applications of fullerenes. *International Journal of Nanomedicine* **2007,** *2,* 639-649.

330. Tegos, G.P.; Demidova, T.N.; Arcila-Lopez, D.; Lee, H.; Wharton, T.; Gali, H.; Hamblin, M.R. Cationic fullerenes are effective and selective antimicrobial photosensitizers. *Chem. Biol.* **2005,** *12,* 1127-1135.

331. Jin, H.; Chen, W.Q.; Tang, X.W.; Chiang, L.Y.; Yang, C.Y.; Schloss, J.V.; Wu, J.Y. Polyhydroxylated C60, fullerenols, as glutamate receptor antagonists and neuroprotective agents. *J. Neurosci. Res.* **2000,** *62,* 600-607.

332. Dennler, G.; Scharber, M.C.; Brabec, C.J. Polymer-fullerene bulk-heterojunction solar cells. *Adv Mater* **2009,** *21,* 1323-1338.

333. Ashcroft, J.M.; Tsyboulski, D.A.; Hartman, K.B.; Zakharian, T.Y.; Marks, J.W.; Weisman, R.B.; Rosenblum, M.G.; Wilson, L.J. Fullerene (C60) immunoconjugates: interaction of water-soluble C60 derivatives with the murine anti-gp240 melanoma antibody. *Chem. Commun.* **2006,** *28,* 3004-3006.

334. Gelderman, M.P.; Simakova, O.; Clogston, J.D.; Patri, A.K.; Siddiqui, S.F.; Vostal, A.C.; Simak, J. Adverse effects of fullerenes on endothelial cells: Fullerenol $C_{60}(OH)_{24}$ induced tissue factor and ICAM-1 membrane expression and apoptosis in vitro. *Int J Nanomedicine* **2008,** *3,* 59-68.

335. Dugan, L.L.; Lovett, E.G.; Quick, K.L.; Lotharius, J.; Lin, T.T.; O'Malley, K.L. Fullerene-based antioxidants and neurodegenerative disorders. *Parkinsonism Relat. Disord.* **2001,** *7,* 243-246.

336. Ratnikova, T.A.; Bebber, M.J.; Huang, G.; Larcom, L.L.; Ke, P.C. Cytoprotective properties of a fullerene derivative against copper. *Nanotechnology* **2011,** *22,* 405101-1-7.

337. Gharbi, N.; Pressac, M.; Hadchouel, M.; Szwarc, H.; Wilson, S.R.; Moussa, F. [60]Fullerene is a powerful antioxidant in vivo with no acute or subacute toxicity. *Nano Lett.* **2005,** *5,* 2578-2585.

338. Sayes, C.M.; Fortner, J.D.; Guo, W.; Lyon, D.; Boyd, A.M.; Ausman, K.D.; Tao, Y.J.; Sitharaman, B.; Wilson, L.J.; Hughes, J.B.; West, J.L.; Colvin, V.L. The differential cytotoxicity of water-soluble fullerenes. *Nano Lett.* **2004,** *4,* 1881-1887.

339. Qiao, R.; Roberts, A.P.; Mount, A.S.; Klaine, S.J.; Ke, P.C. Translocation of C60 and its derivatives across a lipid bilayer. *Nano Lett.* **2007,** *7,* 614-619.

340. Salonen, E.; Lin, S.; Reid, M.L.; Allegood, M.; Wang, X.; Rao, A.M.; Vattulainen, I.; Ke, P.C. Real-time translocation of fullerene reveals cell contraction. *Nano Lett.* **2008,** *4,* 1986-1992.

341. Wong-Ekkabut, J.; Baoukina, S.; Triampo, W.; Tang, I.; Tieleman, D.P.; Monticelli, L. Computer simulation study of fullerene translocation through lipid membranes. *Nat Nano* **2008,** *3,* 363-368.

342. Meng, X.; Li, B.; Chen, Z.; Yaw, L.; Zhao, D.; Yang, X.; He, M.; Yu, Q. Inhibition of a thermophilic deoxyribonucleic acid polymerase by fullerene derivatives. *Journal of Enzyme Inhibition and Medicinal Chemistry* **2007,** *22,* 293-296.

343. Ratnikova, T.A.; Nedumpully, G.P.; Salonen, E.; Ke, P.C. In vitro polymerization of microtubules with a fullerene derivative. *ACS Nano* **2011,** *5,* 6306-6314.

344. Shang, J.; Ratnikova, T.A.; Anttalainen, S.; Salonen, E.; Ke, P.C.; Knap, H.T. Experimental and simulation studies of a real-time polymerase chain reaction in the presence of a fullerene derivative. *Nanotechnology* **2009,** *20,* 415101-1-9.

345. Chen, R.; Ratnikova, T.A.; Stone, M.B.; Lin, S.; Lard, M.; Huang, G.; Hudson, J.S.; Ke, P.C. Differential uptake of carbon nanoparticles by plant and mammalian cells. *Small* **2010,** *6,* 612-617.

346. Brant, J.A.; Labille, J.; Robichaud, C.O.; Wiesner, M. Fullerol cluster formation in aqueous solutions: Implications for environmental release. *J. Colloid Interface Sci.* **2007,** *314,* 281-288.

347. Hoffmann, M.; Hotze, E.M.; Wiesner, M.R. Reactive oxygen species generation on nanoparticulate material, In *Environmental Nanotechnology: Applications and Impacts of Nanomaterials,* Wiesner, M.R. and Bottero, J.Y., Eds.; The McGraw Hil Companies: **2007**; pp. 185-200.

348. Pinteala, M.; Dascalu, A.; Ungurenasu, C. Binding fullerenol $C_{60}(OH)_{24}$ to dsDNA. *Int J Nanomedicine* **2009,** *4,* 193-199.

349. Lehrer, S.S. Solute perturbation of protein fluorescence - Quenching of tryptophyl fluorescence of model compounds and of lysozyme by iodide ion. *Biochemistry* **1971,** *10,* 3254-3263.

350. Schwab, F.; Bucheli, T.D.; Lukhele, L.P.; Magrez, A.; Nowack, B.; Sigg, L.; Knauer, K. Are carbon nanotube effects on green algae caused by shading and agglomeration? *Environ. Sci. Technol.* **2011,** *45,* 6136-6144.

351. Hoshino, A.; Hanaki, K.; Suzuki, K.; Yamamoto, K. Applications of T-lymphoma labeled with fluorescent quantum dots to cell tracing markers in mouse body. *Biochem. Biophys. Res. Commun.* **2004,** *314,* 46-53.

352. Rico, C.M.; Majumdar, S.; Duarte-Gardea, M.; Peralta-Videa, J.; Gardea-Torresdey, J. Interaction of nanoparticles with edible plants and their possible implications in the food chain. *J. Agric. Food Chem.* **2011,** *59,* 3485-3498.

353. Bhattacharya, P.; Conroy, N.; Rao, A. M.; Powell, B.; Ladner, D. A.; Ke, P. C. PAMAM dendrimer for mitigating humic foulant, *RSC Adv.* **2012** (ASAP DOI: 10.1039/c0xx00000x).

354. Bhattacharya, P.; Kim, S. H.; Chen, P.; Chen, R.; Spuches, A. M.; Brown, J. M.; Lamm, M. H.; Ke, P. C. Dendrimer-fullerenol soft-condensed nanoassembly. *J. Phys. Chem. C* **2012** (ASAP DOI: 10.1021/jp3036692).

355. Geitner, N. K.; Bhattacharya, P.; Steele, M.; Ladner, D. A.; Ke, P. C. Understanding dendritic polymer-hydrocarbon interaction for oil dispersion (submitted).